

Analysis of Satellite-Based Polar Mesospheric Cloud Observations

by

Susanne Benze

M.S., Leibniz Universität Hannover, 2006

A thesis submitted to the
Faculty of the Graduate School of the
University of Colorado in partial fulfillment
of the requirement of the degree of
Doctor of Philosophy
Department of Atmospheric and Oceanic Sciences

2012

This thesis entitled:

Analysis of Satellite-Based Polar Mesospheric Cloud Observations

written by Susanne Benze

has been approved for the Department of Atmospheric and Oceanic Sciences

Cora E. Randall

V. Lynn Harvey

Date_____

The final copy of this thesis has been examined by the signatories, and we find that both the content and the form meet acceptable presentation standards of scholarly work in the above mentioned discipline.

Benze, Susanne (Ph.D., Department of Atmospheric and Oceanic Sciences)

Analysis of Satellite-Based Polar Mesospheric Cloud Observations

Thesis directed by Professor Cora E. Randall

Polar Mesospheric Clouds (PMCs) are thin water-ice clouds that form in the summer polar mesopause region. Since PMCs are sensitive to changes in the upper atmospheric temperature and water vapor abundance, they can be used to understand the dynamics of the upper mesosphere. It has also been suggested that they are important indicators of mesospheric climate change. PMCs have been successfully observed from the ground and with remote sensing instruments, for example the Cloud Imaging and Particle Size (CIPS) experiment on the Aeronomy of Ice in the Mesosphere (AIM) satellite, and the Solar Backscatter UltraViolet (SBUV) instruments. This thesis presents validation of CIPS observations by showing a comparison of PMC occurrence frequency, cloud and background albedo as observed by CIPS and SBUV. It is found that frequency and cloud albedo are in excellent agreement, with a small (10%) low bias in the CIPS v3.20 operational frequencies at more equatorward PMC latitudes on the descending node. The background albedo, however, shows a still unresolved bias that depends on hemisphere. Overall, the results show that CIPS PMC data are valid for scientific analysis. Furthermore, this thesis investigates and quantifies the relative importance of several coupling mechanisms that contribute to variability in the PMC season onset, such as the solar cycle and intra-hemispheric and inter-hemispheric coupling. It is found that the Southern Hemisphere (SH) PMC season onset is controlled primarily by the timing of the SH stratospheric wind reversal from its winter to summer state, with a smaller but still important contribution

from the solar cycle. Inter-hemispheric coupling triggered by winter stratospheric wind variations plays a significant role in controlling the Northern Hemisphere (NH) PMC season onset dates, again with additional control by the solar cycle. These couplings explain most of the observed variability in the PMC onset dates as observed by SBUV over the past three decades. Preliminary results indicate that the Specified Dynamics version of the Whole Atmosphere Community Climate Model (SD-WACCM) will be a useful tool for more detailed studies of the mechanisms that control PMC variability. Future studies extending the presented CIPS validation and PMC variability investigation are suggested.

Acknowledgements

My heartfelt thanks go to Cora Randall, my PhD advisor and CIPS Principal Investigator, who enabled this thesis through her advice, support and patience. She has spent a considerable amount of time, energy, and thought on my professional development, and I am deeply thankful. Cora enabled me to be part of the AIM team, which brought with it the possibility to attend plenty of science team meetings, workshops, and conferences, where I grew more and more comfortable presenting in front of an audience and got to know great people. In addition to providing lots of her time for discussions and help, she was always there for emotional support and celebration of little and big successes. When solving a problem now, I sometimes ask myself: “How would Cora handle this?”.

Of course, this thesis would not have been possible without the AIM mission with Principal Investigator Jim Russell and the AIM team, who all brought to life a great and successful mission. Special thanks to Matt DeLand for providing SBUV data and for helpful discussions. There are too many names to mention them all, so thanks to the whole AIM team for letting me be part of it.

Many more people deserve praise for supporting me in different ways. Thanks to Bodil Karlsson for sharing her ideas and insights with me and letting me take off with one of them. Thanks to the members of the “MAG” group for enjoyable group meetings. Thanks to Sam Stevenson, Laura Holt, and Jeff France for coffee breaks and big laughs. Thanks to the ATOC and LASP administrative staff, especially Laurie Conway, for caring support and hard work throughout the years. Thanks to the dissertation support group led by Glenda Russell, which

provided excellent advice and motivation while writing up the thesis. Special thanks to Abby Watrous and Jason English for helpful tips on dissertation formatting. Thanks to Chuck Bardeen for introducing me to my first modeling experience, and to Doug Kinnison, Rolando Garcia, and Dan Marsh for always providing WACCM data and helpful responses to my modeling questions. Thanks to my PhD advisory committee Cora Randall, Brian Toon, Lynn Harvey, Dan Marsh and Jeff Thayer for helpful discussions and good advice throughout the years, as well as comments on my thesis.

Finally, I want to thank my family for loving me, believing in me and being proud of me. Special thanks go to Matthias Brakebusch, who has been at my side through good and hard times, and who supports me in all my endeavors in uncountable ways, which I am deeply grateful for.

Contents

1	Introduction	1
1.1	Polar Mesospheric Cloud overview	1
1.2	PMC properties	3
1.2.1	Seasonal characteristics	3
1.2.2	PMC microphysics	5
1.3	Sources of PMC variability	9
1.3.1	General circulation	9
1.3.2	Hemispheric differences	16
1.3.3	The solar cycle effect	18
1.3.4	PMCs and climate change	20
1.4	PMC observations	26
1.4.1	Early history of PMC observations: human observations	26
1.4.2	Rocket launches	29
1.4.3	Lidar observations	31
1.4.4	Satellite observation overview	34
1.5	AIM	40
1.5.1	CDE	40
1.5.2	SOFIE	41
1.5.3	CIPS	43
1.6	SBUV	51
2	CIPS validation	54
2.1	Summary	54
2.2	Benze <i>et al.</i> [2009]: Comparison of polar mesospheric cloud measurements from the Cloud Imaging and Particle Size experiment and the solar backscatter ultraviolet instrument in 2007	57

2.2.1	Introduction.....	59
2.2.2	Cloud detection algorithm.....	62
2.2.3	Results and discussion.....	68
2.2.4	Conclusions.....	77
2.3	Benze <i>et al.</i> [2011]: Evaluation of AIM CIPS measurements of Polar Mesospheric Clouds by comparison with SBUV data.....	80
2.3.1	Introduction.....	81
2.3.2	CIPS evaluation.....	87
2.3.3	PX and operational analysis.....	94
2.3.4	Summary.....	100
3	Teleconnections and the PMC Season Onset.....	104
3.1	Summary.....	105
3.2	Benze <i>et al.</i> [2012]: On the onset of polar mesospheric cloud seasons as observed by SBUV109.....	
3.2.1	Introduction.....	110
3.2.2	Data description and analysis.....	114
3.2.3	Results.....	118
3.2.4	Discussion and Conclusions.....	128
4	Preliminary results: The PMC onset as observed by SD-WACCM.....	133
4.1	Introduction.....	133
4.2	SD-WACCM.....	135
4.3	Preliminary results.....	138
4.4	Summary and outlook.....	141
5	Conclusions and future work.....	143
6	Bibliography.....	148

List of Tables

TABLE 1: SOFIE CHANNEL CHARACTERISTICS	43
TABLE 2: DIFFERENCES IN THE DAILY FREQUENCIES (CIPS – SBUV) AVERAGED OVER ALL LATITUDES (60 – 85°) DURING EACH SEASON	91

List of Figures

FIGURE 1.1: ILLUMINATED PMCS SCATTER SUN LIGHT DOWN TO OBSERVER ON THE DARK EARTH. 2	
FIGURE 1.2: TIME-ALTITUDE CROSS-SECTION OF SOFIE OCCURRENCE FREQUENCY DURING THE NH 2007 SEASON	4
FIGURE 1.3: TIME-HEIGHT CROSS SECTION OF SOFIE EFFECTIVE RADIUS DURING NH 2007	7
FIGURE 1.4: OBSERVED MONTHLY AND ZONALLY AVERAGED TEMPERATURE AND ZONAL WIND FOR JAN. AND JUL	10
FIGURE 1.5: CROSS SECTION OF THE BREWER-DOBSON CIRCULATION DURING THE NH WINTER ...	14
FIGURE 1.6: SBUV SEASONALLY AVERAGED PMC ALBEDO AT 252 NM BETWEEN 64° AND 74°N FROM 1979 TO 2005 FOR DIFFERENT SBUV INSTRUMENTS	20
FIGURE 1.7: SBUV PMC SEASONAL AVERAGED ALBEDO AND MULTIPLE LINEAR REGRESSION FITS FOR THREE NH AND SH LATITUDE BANDS	22
FIGURE 1.8: SIMULATED LIMB BRIGHTNESS OF PMC AS SEEN FROM ORBITING SPACECRAFT	24
FIGURE 1.9: SLANT EMISSION RATES OBSERVED BY OGO-6 AIRGLOW PHOTOMETER AT 29.6°N AND 78.6°N.....	36
FIGURE 1.10: TIMELINE OF SATELLITE INSTRUMENTS OBSERVING PMCS	38
FIGURE 1.11: PMC SCATTERING, ABSORPTION, AND EXTINCTION SPECTRA MODELED USING THE AVERAGE PMC SIZE DISTRIBUTION	42
FIGURE 1.12: CIPS SCENE PROJECTION ONTO THE ATMOSPHERE AT AN ALTITUDE OF ~83 KM.....	44
FIGURE 1.13: MIE SCATTERING PHASE FUNCTIONS FOR PARTICLES WITH A RANGE OF TYPICAL PMC PARTICLE SIZES COMPARED WITH RAYLEIGH SCATTERING FROM ATMOSPHERIC GASES.....	45
FIGURE 1.14: SCAS AND SZAS FOR EVERY CIPS OBSERVATION DURING ORBIT 424 ON MAY 24 2007	46
FIGURE 1.15: CIPS LEVEL 2 ORBIT STRIP OF CLOUD ALBEDO	47
FIGURE 1.16: CIPS LEVEL 3A ‘DAILY DAISY’ OF CLOUD ALBEDO.....	48
FIGURE 1.17: SAMPLE PHASE FUNCTION CONTAINING A PMC WITH A DERIVED ALBEDO OF 10×10^{-1} SR-1 (10 "G") AND A MEAN PARTICLE SIZE OF 66 NM.....	50
FIGURE 1.18: NOAA-9 SBUV/2 252 NM ALBEDO VALUES FOR ALL MEASUREMENTS POLEWARD OF 50°N ON JUNE 29 1985, AND 252 NM ALBEDO RESIDUALS (DATA—FIT).....	53
FIGURE 2.1: COMPARISON OF THE ALBEDO AND ALBEDO RESIDUAL DERIVED FROM THE STANDARD SBUV/2 CLOUD DETECTION ALGORITHM AND THE MODIFIED, SINGLE-WAVELENGTH ALGORITHM APPLIED TO NOAA-17 SBUV/2 DATA.....	64
FIGURE 2.2: DAILY OCCURRENCE FREQUENCIES FROM NOAA-17 SBUV/2 DATA CALCULATED USING THE ALL-LAMBDA AND 273-NM ONE-LAMBDA ALGORITHMS.....	67
FIGURE 2.3: VIEWING GEOMETRY FOR THE CIPS CAMERAS, WITH THE SBUV/2 FIELD OF VIEW SUPERIMPOSED	68
FIGURE 2.4: FOURTH-ORDER POLYNOMIAL FITS TO THE BACKGROUND ALBEDO FOR CIPS AND NOAA-17 SBUV/2 AND DIFFERENCE BETWEEN THE FITS FOR OVERLAPPING SZA RANGES ..	69
FIGURE 2.5: AVERAGE DIFFERENCE BETWEEN THE POLYNOMIAL FITS TO THE BACKGROUND FOR CIPS AND SBUV/2 AT 273 NM VS. DAY OF YEAR FOR THE NH IN 2007.....	70
SIMILAR TO THE RIGHT PANELS IN FIGURE 2.1, BUT FOR NOAA-17 SBUV/2 AND CIPS DATA ON 22 JUNE 2007; GRAY PLUS SYMBOLS DENOTE PMCS.....	71
FIGURE 2.7: DAILY PMC CLOUD OCCURRENCE FREQUENCY FROM NOAA-17 SBUV/2 DATA AT 273 NM AND CIPS IN THE NH IN 2007	72
FIGURE 2.8: CIPS AND SBUV/2 PMC OCCURRENCE FREQUENCY VS. DAY OF YEAR FOR THREE DIFFERENT LATITUDE RANGES	73

FIGURE 2.9: SAME AS FIGURE 2.8, BUT FOR DAILY AVERAGE ALBEDO RESIDUALS PERTAINING TO CLOUD DETECTIONS IN THE SPECIFIED LATITUDE BINS	74
FIGURE 2.10: COINCIDENCES OVERLAID ON ALL MEASUREMENTS FROM CIPS AND NOAA-17 SBUV/2 ON 27 JUNE 2007, FOR ALL LATITUDES AND ONLY HIGH LATITUDES	75
FIGURE 2.11: DAILY AVERAGE ALBEDO, DAILY OCCURRENCE FREQUENCY, AND DAILY AVERAGE PMC BRIGHTNESS, FOR THE NH 2007 SEASON FROM CIPS AND NOAA-17 SBUV/2	76
FIGURE 2.12: DAILY OCCURRENCE FREQUENCY FROM 75° TO 85°N PLOTTED VS. LONGITUDE FOR SBUV/2 AT 273 NM AND CIPS IN THE NH IN 2007	79
FIGURE 2.13: CIPS SCENE SHOWING ALL FOUR CAMERAS AND THE 150 x 150 KM SBUV-SIZE FOOTPRINTS ON THE PY CAMERA AND THE PX CAMERA.....	86
FIGURE 2.14: CIPS PY AND SBUV NOAA-17 LOCAL TIME VS. DFS AND LATITUDE FOR THE NH 2007 AND SH 2007 SEASONS, BOTH ASCENDING AND DESCENDING NODES	89
FIGURE 2.15: CIPS PY AND SBUV NOAA-17 OCCURRENCE FREQUENCY VS. DFS AND LATITUDE IN NH 2007 TO SH 2008.....	90
FIGURE 2.16: SCATTER PLOTS OF COINCIDENCE RESULTS OF OCCURRENCE FREQUENCY, CLOUD ALBEDO, AND BACKGROUND ALBEDO FOR NH 2007 TO SH 2008 IN THE NH AND IN THE SH. 92	
FIGURE 2.17: PY AND PX FREQUENCY VS. DFS FOR ALL LATITUDES (65° TO 85°).....	95
FIGURE 2.18: PY, $PX > 14 \times 10^{-6} \text{ SR}^{-1}$, AND $L4 > 14 \times 10^{-6} \text{ SR}^{-1}$ FREQUENCY VS. DFS FOR ALL LATITUDES (65° TO 85°)	96
FIGURE 2.19: NH 2007 PX AND OPERATIONAL FREQUENCIES AND DIFFERENCES, $L4-PX$, VS. DFS FOR LATITUDES OF 80°N TO 85°N AND 70°N TO 75°N	98
FIGURE 2.20: SCATTER PLOTS OF PX AND OPERATIONAL (L4) FREQUENCY IN DIFFERENT LATITUDE BANDS	100
FIGURE 3.1: SH STRATOSPHERIC WIND REVERSAL DATES FROM ERA-40 AND ECMWF	109
FIGURE 3.2: TIME SERIES OF SBUV PMC SEASON ONSET DATE IN THE NH AND SH	120
FIGURE 3.3: TIME SERIES OF AVERAGE SH PMC SEASON ONSET DATES AS OBSERVED BY SBUV AND DATE OF SH STRATOSPHERIC ZONAL MEAN ZONAL WIND REVERSAL	121
FIGURE 3.4: PMC ONSET DATE VS. WIND REVERSAL DATE WITH A LINEAR FIT TO THE DATA.....	122
FIGURE 3.5: TIME SERIES OF SBUV PMC ONSET DATE AND LYMAN-ALPHA IN THE SH AND NH 123	
FIGURE 3.6: DIFFERENCE BETWEEN SH PMC ONSET DATE AND SH WIND REVERSAL DATE VS. LYMAN-ALPHA	124
FIGURE 3.7: SBUV AND REGRESSED TIME SERIES OF SH PMC ONSET DATE USING SH STRATOSPHERIC WIND REVERSAL DATE AND SOLAR LYMAN-ALPHA AS LINEAR COMPONENTS	125
FIGURE 3.8: DIFFERENCE BETWEEN THE NH PMC ONSET DATE AND SOLAR LYMAN-ALPHA VS. ZONAL MEAN ZONAL WIND, AND SBUV AND REGRESSED TIME SERIES OF NH PMC ONSET DATE.....	127
FIGURE 4.1: METO AND SD-WACCM STRATOSPHERIC ZONAL MEAN ZONAL WIND AT 75°S \pm 2.5° IN SH 2008	136
FIGURE 4.2: SOFIE AND SD-WACCM MESOSPHERIC ZONAL MEAN TEMPERATURE AT 65° - 70°S DURING SH 2008	138
FIGURE 4.3: EVOLUTION OF SD-WACCM WIND AND TEMPERATURE IN SH 2008 SUMMER	139
FIGURE 4.4: SD-WACCM PMC ONSET DATES CALCULATED FROM THE MODEL TEMPERATURE, WIND REVERSAL DATES, AND THE PMC ONSET AS OBSERVED BY SBUV	141

1 Introduction

Beautiful Polar Mesospheric Clouds (PMCs) have aroused the curiosity of observers for more than 120 years. PMCs have always fascinated observers with their night-shining, wispy appearance, but recently they have increasingly been used as indicators of changes in the atmosphere below them. In order to investigate why PMCs form and vary, the Aeronomy of Ice in the Mesosphere (AIM) mission was launched in April 2007. This thesis presents the validation of one of AIM's instruments, the Cloud Imaging and Particle Size (CIPS) experiment, and investigates and quantifies different mechanisms that control the onset date of the PMC season in both hemispheres. Chapter 1 provides a summary of PMC properties, sources of PMC variability, and PMC observations, both from the ground and by satellite instruments. Chapter 2 presents the validation of the CIPS experiment; these results were published in Benze *et al.* [2009, 2011]. Studies that used the validated CIPS data to investigate atmospheric teleconnections were extended to quantify different mechanisms that control the onset date of the PMC season; this is presented in Chapter 3 and published in Benze *et al.* [2012]. In Chapter 4 the Specified Dynamics version of the Whole Atmosphere Community Climate Model (SD-WACCM) is investigated for its applicability to more detailed studies of the mechanisms that control PMC variability. Conclusions and future work are presented in Chapter 5.

1.1 Polar Mesospheric Cloud overview

Clouds are not only present in the troposphere, but also in the upper atmosphere. Mesospheric clouds have been called by different names: NoctiLucent (night-shining) Clouds

(NLCs) when observed from the ground, or PMCs when observed from satellite. Scientists agree that NLCs and PMCs are the same phenomenon, so currently their nomenclature is a matter of preference. In this document they will be referred to as PMCs. PMCs are very thin water-ice clouds forming in the summer polar mesopause region. Due to their small vertical extent and small optical depth a ground observer can only observe them against a dark background sky when they are still illuminated by the sun. They disappear against the bright background sky when the sun is 6° or less below the horizon [Gadsden and Schröder, 1989]. Figure 1.1 shows how PMCs scatter sunlight that is observed on a dark Earth.

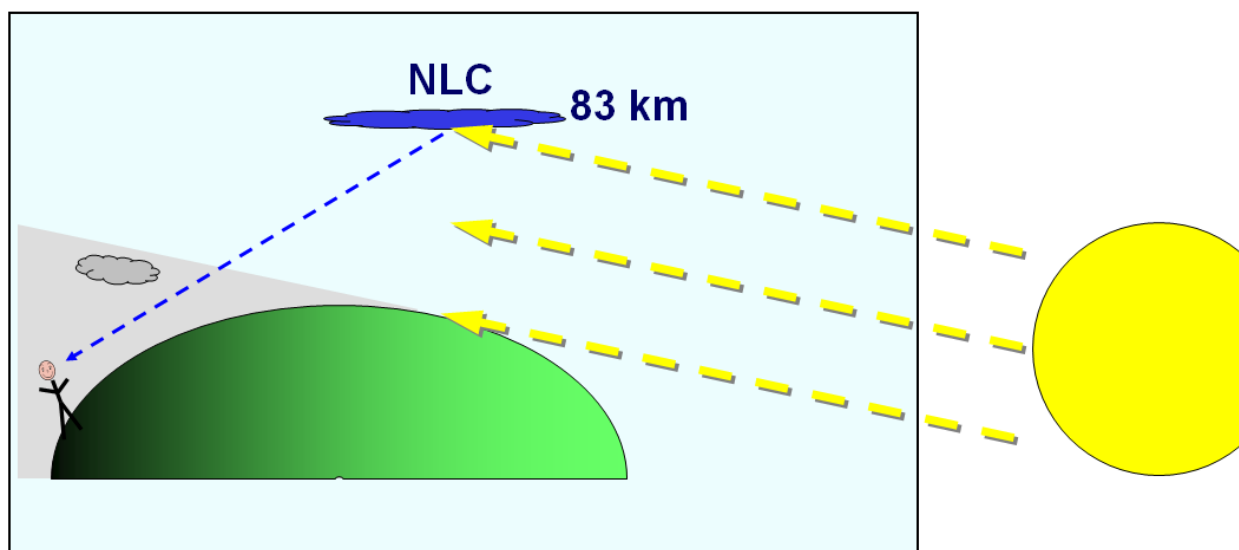


Figure 1.1: Illuminated PMCs scatter sun light down to the observer on the dark Earth.

The existence of PMCs may seem surprising considering the dryness of the upper mesosphere: between 81 km and the mesopause, where most PMCs form, summer polar water vapor concentrations do not exceed 8 ppmv [Stevens *et al.*, 2005a]. For clouds to nucleate and grow, polar summer temperatures in the mesopause region must be very cold, and indeed temperatures of 130 K and lower were observed by Witt *et al.* [1964], Lübken [1999], Höffner and Lübken [2007], and Lübken *et al.* [2008].

PMCs are important as indicators of the upper atmospheric temperature and water vapor. Increasing concentrations of anthropogenic methane (CH₄) and carbon dioxide (CO₂) are expected to result in higher concentrations of water vapor and lower temperatures in the upper atmosphere [Thomas, 1996]. Thus, climate change is suggested to lead to an increase in the occurrence frequency and brightness of PMCs; and this suggestion is supported by reports of increasing PMC frequency and brightness over the last decades [e.g., Shettle *et al.*, 2002; Thomas *et al.*, 2003; DeLand *et al.*, 2007]. Temperature and water vapor are also modulated by the solar cycle and several dynamic processes, for example the strength of the residual circulation, which changes vertical motion and therefore adiabatic cooling as well as upward transport of water vapor in the polar region. In summary, PMC variability, for example long-term trends, solar dependence, hemispheric differences, season-to-season and intra-seasonal variations, can be utilized to learn how the general circulation, the solar cycle, and climate change affect the mesopause region.

1.2 PMC properties

1.2.1 Seasonal characteristics

A typical PMC season begins not earlier than 40 days before and ends not later than 80 days after summer solstice. For convenience, hereinafter "days from solstice" will be abbreviated by DFS. Northern Hemisphere (NH) seasons will be referred to by their hemisphere and year; e.g., "NH 2007". Southern Hemisphere (SH) seasons will be referred to by their hemisphere and year in which they begin; e.g., the SH 2007-2008 season will be referred to as the "SH 2007" season.

A widely measured PMC diagnostic is occurrence frequency or just frequency. Empirically this is defined as the ratio of the number of cloud observations to the total number of observations. Typically, frequency is defined during a certain time range (e.g., daily frequency) and latitude range. Both PMC occurrence frequency and brightness are generally highest near the poles and decline toward the equator. Usually, PMCs are observed poleward of latitudes around 50° , but in rare cases PMCs have also been observed at lower latitudes [e.g., Wickwar *et al.*, 2002]. Measurements from sensitive instruments such as the Solar Occultation for Ice Experiment (SOFIE) show that the PMC season has a rather abrupt start and end, with frequencies during the main season ranging between about 65% and 100%. Figure 1.2 shows SOFIE PMC frequencies for the NH 2007 season.

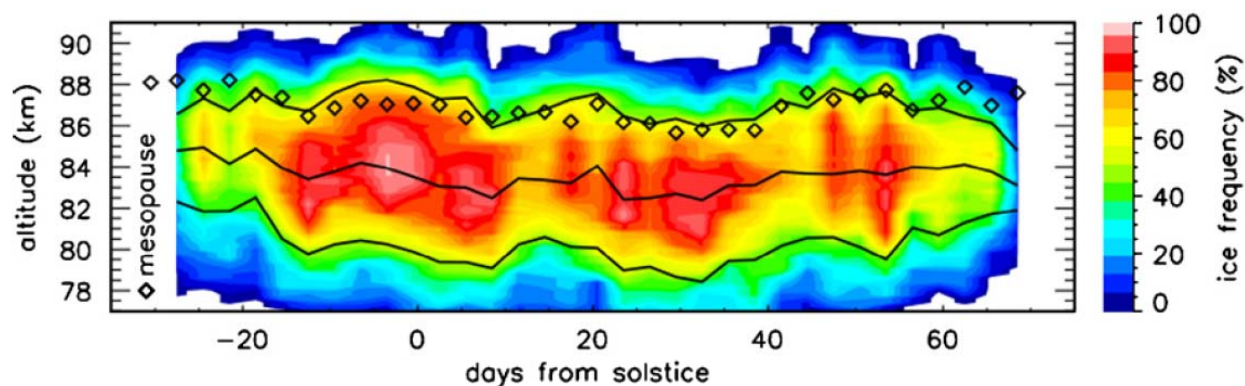


Figure 1.2: Time-altitude cross-section of SOFIE occurrence frequency during the NH 2007 season. Solid lines denote average ice layer top, peak, and bottom altitudes that are defined from PMC extinction, diamonds show the average mesopause altitude. White regions indicate the absence of data. From Hervig *et al.* [2009b], Figure 3a¹.

The typical PMC season starts with a sharp frequency increase over 5 to 10 days. At the beginning and end of the PMC season, peak cloud altitude is usually 2-3 km higher than in the middle of the season [Bailey *et al.*, 2005; Hervig *et al.*, 2009b; Karlsson *et al.*, 2009b]. During

¹ Reprinted from *Journal of Atmospheric and Solar-Terrestrial Physics*, 71, Hervig, M. E., Gordley, L. L., Russell, III, J. M. and Bailey, S. M., SOFIE PMC observations during the northern summer of 2007, 331-339, copyright (2008), with permission from Elsevier.

the season, frequency stays relatively constant with the possibility of steep frequency dips due to warmer temperatures that cause sublimation of ice particles (more details are shown in Section 1.3). The maximum observed frequency is usually at the same altitude as maximum ice extinction. Figure 1.2 also indicates that the mesopause height is generally identical to the cloud top height, even though sometimes PMCs are observed above the mesopause. Russell *et al.* [2010] showed that the mean PMC height is located $3.5 \text{ km} \pm 0.5 \text{ km}$ below the mean mesopause height in both hemispheres throughout the season. The average ice layer thickness increases from about four km in early season to seven km by mid-summer [Hervig *et al.*, 2009b]. The season ends with a sharp decline of frequency similar to the season onset. Polar Mesospheric Summer Echoes (PMSEs) close to or above the mesopause indicate the presence of subvisible ice particles, which extend from the typical PMC altitude of 83 km to over 90 km [Rapp and Lübken, 2004]. It is suggested that PMCs and PMSEs are different manifestations of a continuous ice layer [Hervig *et al.*, 2009b].

1.2.2 PMC microphysics

PMCs are known to be ice clouds, but that was not clear when they were first observed in the late 19th century. PMCs were first thought to directly relate to the Krakatoa volcanic eruption in 1883. It was suggested that particles blown into the upper atmosphere by strong volcanic eruptions caused an increase in PMCs [Gadsden and Schröder, 1989]. While it is likely that Krakatoa did lead to PMC formation, the current understanding of ice nucleation in the upper mesosphere is as follows:

In the summer polar upper mesosphere, water vapor concentrations are usually 5-8 ppmv [e.g., Hervig *et al.*, 2009b; Stevens *et al.*, 2005a]. In combination with the very low temperatures of 120-150 K this causes water to never be in liquid phase, but either gaseous or solid. The transition of water ice into the gas phase is called *sublimation*. PMC nucleation takes place at altitudes with the highest saturation ratios $S = p_{\text{H}_2\text{O}}/p_{\text{SAT}}$. $p_{\text{H}_2\text{O}}$ is the water vapor partial pressure and p_{SAT} is the saturation vapor pressure of water vapor over ice. In units of Pascal, p_{sat} is given by $p_{\text{sat}} = \exp(9.550426 - 5723.265/T + 3.53068 \cdot \ln(T) - 0.00728332 \cdot T)$ [Rapp and Thomas, 2006]. Supersaturation is defined as where $S > 1$. S is highest close to the temperature minimum between 86 and 90 km. The typical S in the polar summer mesopause region is on the order of 100 [Lübken and Müllemann, 2003]. This value is too small to make homogeneous nucleation a probable candidate for PMC nucleation. Homogeneous nucleation is the spontaneous formation of new particles from the ‘pure’ gas phase. However, extreme values of supersaturation of 10^6 to 10^8 in the polar summer mesopause region have also been observed [e.g., Lübken *et al.*, 2009], which is high enough to enable homogeneous nucleation of PMCs. Homogeneous nucleation has been discussed by Zsazsky *et al.* [2009], Lübken *et al.* [2009], and Murray and Jensen [2010]. In accordance with the most commonly accepted understanding, however, preexisting nuclei are needed for ice nucleation in a process that is called heterogeneous nucleation. Existing ice particles grow by the direct deposition of water vapor onto their surfaces, assuming that the atmosphere is sufficiently supersaturated. Growing particles settle down due to gravity, and during this motion the ice particles experience vertical and horizontal mean winds as well as small-scale motions such as turbulence and waves. Growing beyond a certain size the ice particles are observable from ground and from space. When particles fall further they sublime due to increasing temperature. This understanding of PMC nucleation means that for constant

and finite amounts of water vapor present, few nuclei should form few large ice particles, whereas many nuclei should form many small ice particles, assuming all available water vapor is used up in the process of ice particle growth. Scattered radiation varies as r^6 [e.g., Thomas, 1991], and is thus extremely sensitive to the ice particle radius (r). Therefore, many small ice particles should cause PMCs to be less bright than PMCs consisting of fewer but bigger particles (as long as the particle size distribution curve is less steep than an r^{-6} dependence). Figure 1.3 shows the SOFIE effective radius profiles vs. time during the NH 2007 season. Throughout the PMC layer, ice particle size decreases with altitude. Since cloud brightness is correlated with the ice particle size, cloud brightness peaks close to the ice layer bottom. Therefore, cloud altitude generally anti-correlates with cloud brightness [DeLand *et al.*, 2006a].

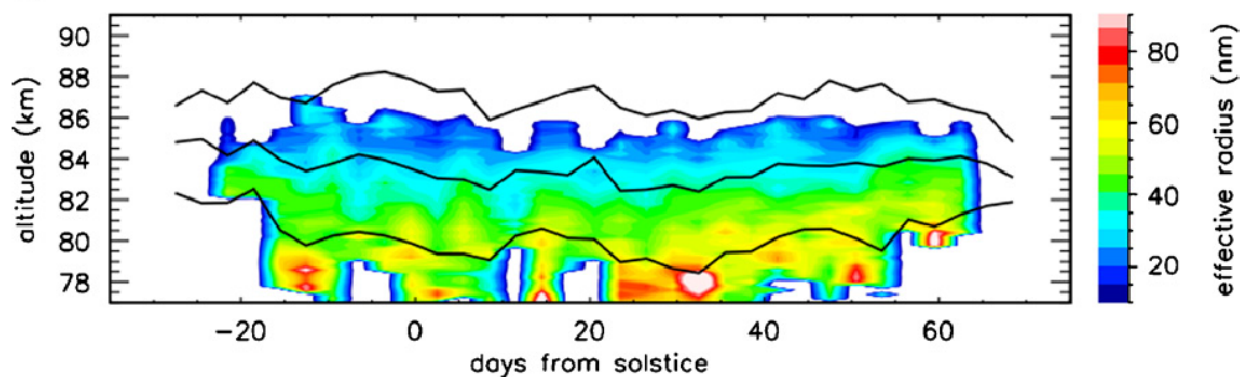


Figure 1.3: Time-height cross section of SOFIE effective radius during the NH 2007 season. The solid lines show average ice layer top, peak, and bottom altitudes. White regions indicate the absence of data. From Hervig *et al.* [2009b], Figure 3d².

However, there is a current challenge to the understanding of PMC nucleation mechanisms. Megner [2011] found through model studies that neither ice mass nor cloud brightness are strongly sensitive to the cloud nuclei concentration. In contrast, the temporal evolution of the temperature and wind field is a much stronger driver of PMC variability than nuclei

² Reprinted from *Journal of Atmospheric and Solar-Terrestrial Physics*, 71, Hervig, M. E., Gordley, L. L., Russell, III, J. M. and Bailey, S. M., SOFIE PMC observations during the northern summer of 2007, 331-339, copyright (2008), with permission from Elsevier.

concentration. Megner [2011] suggests that there is a decoupling of cloud nucleation in regions of high supersaturation close to the mesopause (~87 km, nucleation region) from the growth of ice particles where water vapor is abundant at lower altitudes (~82 km, growth region). This understanding would mean a decoupling of nucleation from the ice growth and therefore visible clouds, both in time and space. Furthermore this suggests that nucleation is controlled by temperature whereas growth is controlled by the availability of water vapor.

As to the PMC nuclei themselves, they are difficult to study using remote sensing techniques [Gelinas *et al.*, 2005], and no clear consensus of their composition has yet emerged. Over the last three decades, several candidates have been brought forth: large proton hydrate ion clusters [Witt, 1969], soot (elemental carbon) particles [Pueschel *et al.*, 2000], sulfuric acid aerosol particles [Mills *et al.*, 2005], sodium bicarbonate [Plane, 2000], sodium hydroxide [Petrie, 2004], and meteoric smoke particles [Rosinski and Snow, 1961; Hunten *et al.*, 1980, Hervig *et al.*, 2009c]. Large proton hydrate ion clusters and soot particles have been excluded as likely nucleation sites for PMCs, whereas meteoric smoke is considered the most likely candidate for PMC nucleation by Rapp and Thomas [2006]. However, it is also possible that there is more than one kind of nucleus playing a role in the formation of PMC particles. In summary, the composition of PMC nuclei is uncertain, with meteoric dust being the most probable candidate. Since the aforementioned nucleus candidates have so far been hard or impossible to observe, the number density or concentration of mesospheric ice nuclei and their spatial and vertical distribution remain uncertain as well.

1.3 Sources of PMC variability

1.3.1 General circulation

PMCs form in the polar summer mesopause region, where from radiative equilibrium one would expect warmer temperatures than in the winter hemisphere. Radiative equilibrium is the equilibrium of solar heating and infrared (IR) cooling during the absence of atmospheric motions. However, the polar summer mesopause region is the coldest region in Earth's atmosphere. Dynamical processes through vertical motions and the resulting adiabatic warming/cooling drive the atmosphere away from radiative equilibrium to observed temperatures. This section describes how the mesopause temperature and therefore PMCs are tightly connected to the general circulation in the middle atmosphere, that region of the atmosphere that extends from the tropopause at 12-20 km to the mesopause at ~90 km.

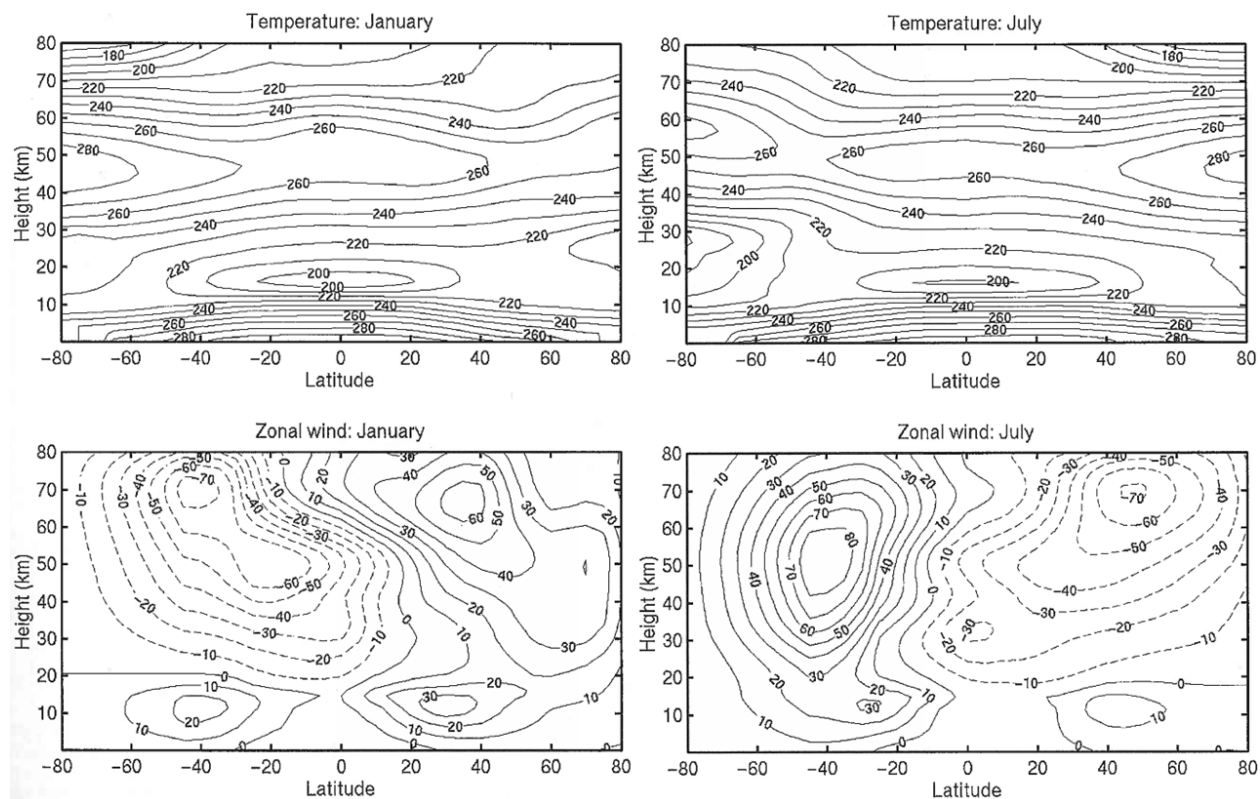


Figure 1.4: Observed monthly and zonally averaged temperature [K, top] and zonal wind [m/s, bottom] for January (left) and July (right). From Holton [2004], Figures 12.2 and 12.3³.

Figure 1.4 shows the middle atmosphere temperature (top) and zonal wind (bottom) in January (left) and July (right). Because of absorption of ultraviolet radiation by ozone, the summer stratosphere temperature increases with height to a maximum at the stratopause near 50 km. Lack of sunlight in the polar winter leads to a cooler polar winter stratosphere. In the mesosphere, temperature decreases with altitude due to the reduced solar heating of ozone and decreasing proximity from the Earth. Figure 1.4 shows that the temperature in the mesosphere, unlike in the stratosphere, decreases from the winter to summer pole. This is in obvious disagreement with what would be expected from radiative equilibrium. The main features of the zonal mean wind in Figure 1.4 include a westward jet in the summer hemisphere peaking at ~70

³ This article was published in Academic Press, International Geophysics Series, Vol. 88, Holton, James R., Dynamic Meteorology, 535 pages, Copyright Elsevier (2004).

km, and an eastward jet in the winter hemisphere with maximum wind speeds occurring near the 60 km level. The eastward jet forms the edge of the polar vortex that exists in the winter polar stratosphere and mesosphere. The wind and temperature distributions shown here are a result of the general circulation in the middle atmosphere, and they also are of particular importance for wave filtering as described below.

The general circulation in the middle atmosphere can be split up into two parts: the lower part in the stratosphere, which is also called the Brewer-Dobson circulation, and the upper part in the mesosphere, which is also called the residual circulation. The residual circulation consists of upwelling over the summer pole and downwelling over the winter pole. This circulation is driven by vertically propagating internal gravity waves (GWs) breaking in the mesosphere. These GWs exist due to flow over topography, frontal processes, convection, and jet streams [Fritts and Alexander, 2003]. As the atmospheric density decreases with altitude, the GW amplitude increases until the waves become convectively unstable. They break and deposit their angular momentum in the same direction as the GW phase speed. In other words, they “drag” the background flow toward their phase speed. Therefore this momentum deposition is also called GW drag [e.g., Garcia and Boville, 1994].

GWs will only vertically propagate through the stratosphere and mesosphere when their phase speed either exceeds the background wind speed or is of opposite direction [e.g., Andrews *et al.*, 1987]. In addition, the breaking altitude depends on the wave amplitude and vertical wavelength: the larger the amplitude and the smaller the vertical wavelength, the lower the wave will break. During summer, the mean stratospheric and mesospheric background flow is westward, so GWs that break in the mesosphere primarily have eastward phase speeds, resulting in a net eastward GW drag in the mesosphere. The induced eastward flow from this drag is

subject to the Coriolis torque, which turns it to the right in the NH and left in the SH. Balance is re-established when the induced flow is directed equatorward. Mass conservation requires that upwelling occurs in the summer hemisphere. Analogous arguments, but for oppositely directed GW drag, can be made for the winter hemisphere to explain downwelling in the polar winter mesosphere. Polar upwelling in the summer hemisphere and downwelling in the winter hemisphere form the vertical components of the residual circulation. Upwelling and downwelling are associated with adiabatic cooling and warming, and hence explain the departure from radiative equilibrium, with colder temperatures in the polar summer mesosphere, and warmer temperatures in the polar winter mesosphere. Only through this dynamical process is it possible that the polar summer mesopause region becomes cold enough for the formation and growth of PMCs.

Driven primarily by latitudinal variations in solar insolation, the winter stratosphere latitudinal gradient in temperature is characterized by high temperatures over the equator and low temperatures over the pole. Due to geostrophic adjustment this results in strong eastward winds at mid-latitudes. Flow over large-scale topographic features, such as the Rocky Mountains, the Himalaya-Tibetan complex, and the Andes, causes vertically propagating planetary waves (PWs) to be generated. The PW dispersion relationship shows that they always have a westward phase speed. Charney and Drazin [1961] developed an important theory about the vertical propagation of PWs, which shows that upward propagation takes place only in an environment of weak to moderate eastward zonal winds, and hence only in the winter hemisphere. In addition, only the waves with the longest wavelengths (wave numbers 1 and 2) are likely to propagate into the stratosphere. There they deposit their westward angular momentum into the eastward background flow, thereby decelerating the background flow, and

sometimes even reversing it. The induced westward angular momentum from breaking PWs is subject to the Coriolis torque, which turns it to the right in the NH (left in the SH). Balance is re-established when the induced flow is directed poleward. Downwelling and adiabatic warming in the polar winter stratosphere follows from mass conservation. This resulting circulation is called the Brewer-Dobson circulation. It consists of upwelling above the tropics, poleward transport, and downwelling over the polar winter, as shown in Figure 1.5. Since it transports mass and chemicals upward in the tropics and downward in the extratropics, it is also called the transport circulation. Since PWs only propagate into the winter stratosphere, this cell is a winter circulation only – it is basically nonexistent in the summer hemisphere. In the absence of waves, i.e., in radiative equilibrium, the polar region would be much colder in the middle of winter than it actually is.

The above mentioned strong eastward winds form the stratospheric polar night jet, which defines the edge of the polar vortex. The jet acts as a barrier to meridional transport, thereby isolating the air inside the polar vortex. Since there is less PW activity in the SH due to higher zonal symmetry, the SH winter polar vortex is closer to radiative equilibrium and therefore colder than the NH winter polar vortex. Fewer stratospheric warmings occur in the SH polar region, whereas in the NH, the Brewer-Dobson circulation is stronger, leading to a warmer and less stable polar vortex.

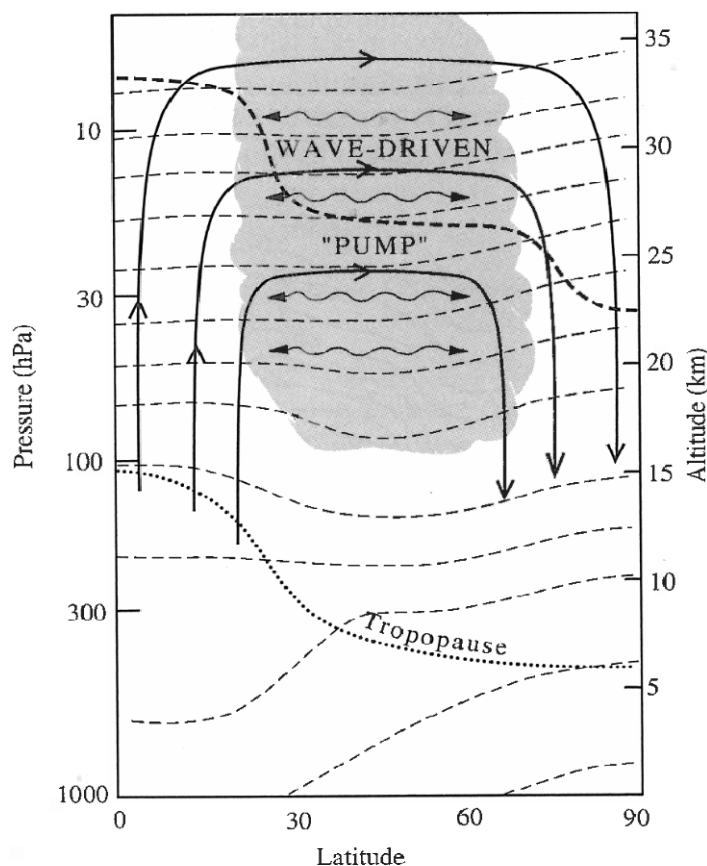


Figure 1.5: Schematic cross section of the Brewer-Dobson circulation during the NH winter. Solid lines depict the wave-driven transport circulation, with the shaded region being the region of PW breaking. Thin dashed lines are potential temperature surfaces. The dotted line is the tropopause. Wavy double-headed arrows depict meridional transport and mixing by eddies. From Holton [2004], Figure 12.8⁴.

The Brewer-Dobson circulation is also important for the PMC region since the polar winter stratosphere can affect the summer polar mesopause region through an inter-hemispheric coupling process [e.g., Becker and Schmitz, 2003; Karlsson *et al.*, 2007]. Briefly, PW-induced changes in the winter stratosphere may change the filtering of GWs in the winter hemisphere, which affects GW breaking in the winter mesosphere. For example, if the winter stratosphere is highly disturbed by PWs, breaking PWs will decelerate or even reverse the normally strong eastward zonal mean zonal wind in the winter stratosphere. This will affect the filtering of GWs

⁴ This article was published in Academic Press, International Geophysics Series, Vol. 88, Holton, James R., Dynamic Meteorology, 535 pages, Copyright Elsevier (2004).

so that the average breaking levels are shifted to lower altitudes and the GW efficiency driving the residual circulation in the mesosphere is decreased [Becker and Schmitz, 2003]. Due to mass conservation, this leads to decreased descent over the winter pole and decreased ascent over the summer pole, with less adiabatic cooling and thus fewer PMCs. This inter-hemispheric coupling process is described in detail by Becker and Schmitz [2003], Becker *et al.* [2004], and Karlsson *et al.* [2007; 2009a]. In summary, increased PW activity in the winter hemisphere leads to fewer and dimmer PMCs in the summer hemisphere.

PMCs are also observed to vary in local time due to temperature oscillations caused by tides [von Zahn *et al.*, 1998; Chu *et al.*, 2003, 2006; Fiedler *et al.*, 2005; Stevens *et al.*, 2010]. Thermally forced tides are excited by O₃ and water vapor solar radiation absorption [e.g., Lindzen, 1967; Lindzen and Blake, 1970]. Tides can play an important role for the thermal and dynamical structure of the mesosphere and lower thermosphere [Lübken *et al.*, 2011]. While they change the temperature and winds, they also interact with small and large scale waves and can significantly modify GW propagation. Tidal amplitudes are largest at equatorial latitudes. Theoretical studies predict rather small amplitudes at summer polar latitudes [e.g., Achatz *et al.*, 2008]; however, measurements show surprisingly large tidal modulations of temperature of up to ± 6 K [Lübken *et al.*, 2011]. Especially ground-based but also satellite observations have shown that PMCs vary diurnally in frequency, brightness and altitude [Stevens *et al.*, 2009]. Light Detection And Ranging (lidar) instruments are especially suited to observe local time variations. Using lidar data at 69°N between 1997 and 2003, Fielder *et al.* [2005] showed that PMCs have both a semidiurnal and a diurnal component, and that they occur preferably in the early morning hours, with a maximum occurrence frequency at local times between 4 AM and 7 AM. Satellites that are in a sun-synchronous orbit are locked in local time, which means that they observe

PMCs at only two different local times at any given latitude (except near the pole, where they progressively sample all local times between their ascending and descending nodes). Stevens *et al.* [2009] used the Spatial Heterodyne IMager for MEsospheric Radicals (SHIMMER), which is not in a sun-synchronous orbit, to show that PMC frequencies between 50°N and 58°N have a semidiurnal behavior with two peaks near 6 AM and 6 PM local time, with PMCs at 6 AM being 10 times more frequent than clouds at 9 AM or 4 PM. Local time variations therefore must be taken into account when combining results from different satellite instruments that observe PMCs at different local times, especially when analyzing long-term trends [e.g., DeLand *et al.*, 2007].

1.3.2 Hemispheric differences

The first indication for hemispheric differences in PMCs was reported by Olivero and Thomas [1986] using Solar Mesosphere Explorer (SME) data between 1981 and 1984. Whereas they reported quite similar occurrence frequencies of NH and SH clouds, the NH clouds were observed to be brighter than their SH counterparts. It was suggested that more scattering particles were present in the NH on average. Observations of PMSEs by Woodman *et al.* [1999] proved to be more difficult in the SH than in the NH, which gave rise to the suggestion that the SH polar summer mesosphere may be warmer by 7.5 K than the NH. Doubts emerged when Lübken *et al.* [1999; 2004] presented falling spheres measurements that suggested that both temperature and wind in the polar summer Antarctic in January and the Arctic in July were similar. However, these results were controversial since other wind measurements, e.g., Vincent [1994] and Dowdy *et al.* [2001] suggested a stronger residual circulation and therefore lower mesopause temperature during NH summer than SH summer. Lidar observations, e.g., Gardner *et al.* [2001]

and Chu *et al.* [2003], showed a hemispheric difference in PMC altitudes, with SH clouds being 2-3 km higher than NH clouds. It was speculated that this might be due to the previously suggested temperature difference, which would cause the altitude of the supersaturation region to be higher in the SH than in the NH. Two possible reasons for this temperature difference were given: 1) a direct radiative effect from the eccentricity of Earth's orbit, which results in a 6% higher solar flux in January in the SH than in July in the NH, and 2) a different GW filtering due to hemispheric asymmetries in summer mean wind of the troposphere and stratosphere. Siskind *et al.* [2003] responded to these suggestions by modeling hemispheric differences in summer temperatures due to the aforementioned effects. Their theoretical studies suggested that poleward of 30° latitude the SH middle atmosphere from 20 to 85 km is warmer than in the NH by 3-8 K. They found that this temperature difference was mostly due to a weaker GW drag in the SH upper mesosphere, leading to a weaker residual circulation over the SH summer pole using the arguments presented in Section 1.3.1. They state that this weaker GW drag in the SH upper mesosphere is due to stronger winds in the SH summer upper troposphere and lower stratosphere region that filters out more GWs in the SH than in the NH. Several studies then confirmed significant differences in PMC occurrence frequency, brightness, and cloud altitude, e.g., Bailey *et al.* [2005], Petelina *et al.* [2006], Wrotny and Russell [2006], and Hervig and Siskind [2006]. Both Wrotny and Russell [2006] and Hervig and Siskind [2006] also presented polar mesospheric temperature and water vapor measurements from the HALOE instruments spanning 14 years: while water vapor was similar between the hemispheres, temperature was 4-7 K lower in the NH polar summer between 75 and 86 km. Bailey *et al.* [2007] stated that NH clouds have a greater equatorward extent, have a larger population of bright clouds and are on average 1.1 km lower in altitude, whereas SH clouds exhibit larger variability in frequency.

In summary, hemispheric differences in PMC occurrence frequency, brightness, and altitude are well established, with more frequent clouds that are brighter and present at lower altitudes in the NH. The cause for this is assumed to be a temperature asymmetry, with the NH polar summer upper mesosphere being 3-7 K colder than its SH counterpart. The larger variability in SH PMC frequency is also expected to influence inter-hemispheric differences in the variability of the PMC onset dates as described in detail in Chapter 3.

1.3.3 The solar cycle effect

A solar cycle effect on PMCs was suggested first by sky observers in the first half of the 20th century [e.g., Vestine, 1934; Fogle and Haurwitz, 1966]. However these observations were not adequate for quantitative investigations of solar cycle effects on PMCs due to statistical non-uniformity of the dataset from year to year and observational factors like the weather. Today it is well known that the solar cycle is anti-correlated with PMC occurrence frequency and brightness [e.g., DeLand *et al.*, 2006a]. The solar Lyman- α emission line at 121.6 nm contains most of the UV energy deposited near the mesopause [Thomas and Olivero, 2001]. From solar minimum to solar maximum, the Lyman- α flux varies by ~50% [Woods *et al.*, 2000]. Increased Lyman- α flux affects PMCs in two ways: through a decrease of water vapor due to larger photolytic destruction rates and an increase of temperature due to stronger diabatic UV heating rates. As suggested by Garcia [1989], water vapor should decrease by 30-40% at 80 km due to enhanced photolysis at solar maximum. Khosravi *et al.* [2002] simulate a 3-6 K temperature increase over the summer pole between 80 and 85 km at solar maximum compared to solar minimum. Both Schmidt *et al.* [2006] and Marsh *et al.* [2007] find that the temperature minimum at the summer polar mesopause increases ~1.5 K at solar maximum compared to solar minimum. However, doubt

was shed on the direct solar Lyman- α control of PMCs when a lag of two to three years between the solar cycle and the PMC changes (with the solar cycle leading) was found by Gadsden [1998] and Thomas and Olivero [2001]. The time constants for both heating and photolysis rates are small compared to the PMC season, so no time lag would have been expected between solar forcing and PMC activity [DeLand *et al.*, 2003]. Several later studies using satellite data, e.g., DeLand *et al.* [2003], Hervig and Siskind [2006], DeLand *et al.* [2007], Kirkwood *et al.* [2008], and Shettle *et al.* [2009], found phase lags between zero and 1.5 years; that is, they were unable to rule out a zero phase lag. Thus whether a phase lag exists is still controversial. However, DeLand *et al.* [2003] suggest that if real, such a lag might be explained by a lag between the solar cycle and the mesospheric winds, particularly the upward wind. Hervig and Siskind [2006] use HALOE data between 1991 and 2004 (solar cycle 23) and find that at 85 km, water vapor varies by $\sim 30\%$ and temperature by ~ 5 K, with more water vapor and lower temperatures during solar maximum conditions. Warmer and drier conditions during solar maximum conditions lead to a decrease in PMC brightness by $\sim 23\%$. They also find that the PMC response to solar activity is the same in both hemispheres. This, however, is contradicted by DeLand *et al.* [2007] using Solar Backscatter UltraViolet (SBUV) data over 27 years: they find that the NH response of PMC brightness to solar activity is bigger (16.9%) than the SH response (9.9%). Figure 1.6 shows the PMC albedo from different SBUV instruments that are normalized to each other. Both the ~ 11 -year anti-correlation of PMC albedo and solar cycle as well as a linear trend (Section 1.3.4) are visible.

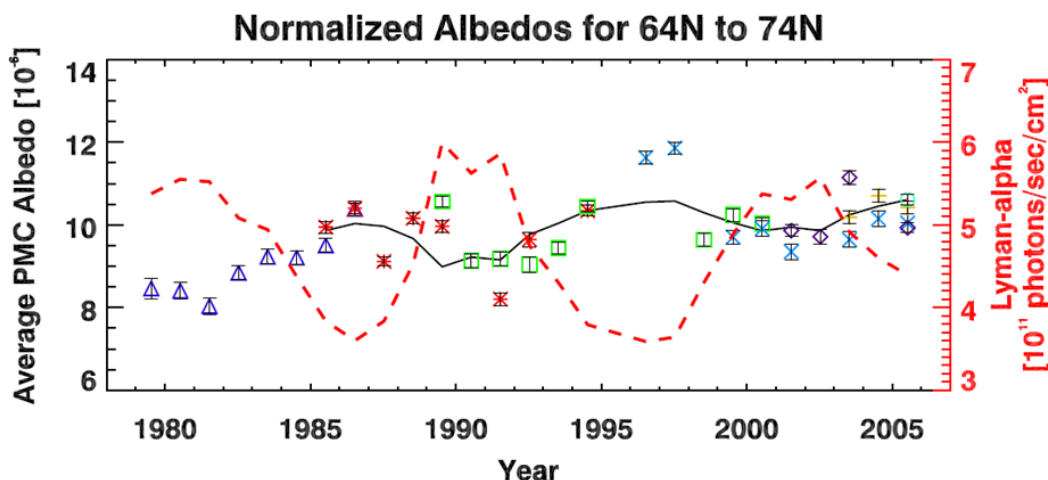


Figure 1.6: SBUV seasonally averaged PMC albedo at 252 nm between 64° and 74°N from 1979 to 2005 for different SBUV instruments (triangle = Nimbus-7, asterisk = NOAA-9, square = NOAA-11, cross = NOAA-14, diamond = NOAA-16, plus = NOAA-17, circle = NOAA-18). Error bars are $\pm 1 \sigma$ standard errors. Inter-instrumental differences (e.g., local time differences) have been normalized. Dashed line: average solar Lyman alpha flux for each season. Solid line: multiple linear regression fit including components for solar cycle and a linear trend between 1985 and 2005. From DeLand *et al.* [2007], Figure 6b⁵.

1.3.4 PMCs and climate change

A first indication of long-term changes in PMCs was presented by Gadsden [1985], who reported an increase in frequency from ground-based observations over 20 years. However, this finding was later found to be in error, e.g., Kirkwood and Stebel [2003]. Thomas *et al.* [1989] proposed that a general increase in tropospheric CH₄ could possibly increase cloud brightness. CH₄ reacts with OH and excited atomic oxygen, O(¹D), to produce water vapor and H in the stratosphere. Water vapor is transported with the general circulation into the mesosphere. Thomas *et al.* [1989] suggested that PMCs were not observed prior to 1885 because they were not bright enough due to a lack of water vapor needed for ice particle growth. It is speculated

⁵ Reproduced by permission of American Geophysical Union. DeLand, M. T., Shettle, E. P., Thomas, G. E. and Olivero, J. J., 2007, Latitude-dependent long-term variations in polar mesospheric clouds from SBUV version 3 PMC data, *Journal of Geophysical Research-Atmospheres*, 112, D10315, 2007. Copyright [2007] American Geophysical Union.

that the Krakatoa eruption in 1883 injected both water and condensation nuclei into the stratosphere. Through transport of water vapor into the mesosphere, cloud growth may have increased, resulting in bigger ice particles that may have caused a sudden boost of PMC brightness.

Thomas [1996a; 1996b] summarized how both mesospheric temperature and water vapor concentrations may potentially change due to global climate change in the troposphere. Many greenhouse gases like CH₄ and N₂O do not have a direct effect on the mesosphere since they are destroyed by photodissociation in the stratosphere. However, CH₄ is converted to water vapor as described above, and CO₂, which is transported to the mesosphere, causes radiative cooling in the mesosphere. IPCC [2007] states that the atmospheric mixing ratio of CO₂ has increased globally by about 100 ppmv (36%) over the last 250 years, while CH₄ has increased by about 1.1 ppmv (140%) compared to pre-industrial conditions. This increase in methane corresponds to an increase in water vapor mixing ratio of about 2.2 ppmv. Increases since about 1740 can be attributed to human activities. Overall increases of CH₄ and CO₂ may have caused a general positive trend in PMC cloud brightness and negative trend in temperature that is currently ongoing.

Ground observations, however, did not confirm statistically significant trends in PMC frequency or brightness [(Dalin *et al.*, 2006, Kirkwood *et al.*, 2008)]. The role of PMCs as an indicator of global climate change has been controversial. For example, the discussion by Thomas [1996] was followed by von Zahn [2003], which was followed by Thomas *et al.* [2003]. Several studies based on satellite data [e.g., Shettle *et al.*, 2002; DeLand *et al.*, 2003; DeLand *et al.*, 2007] provided consistent summaries of an observed trend in PMC brightness and frequency. Using SBUV data, DeLand *et al.* [2007] found that the trend from 1979 to 2005 in PMC albedo

over the polar cap (50° - 82° latitude) was similar in both hemispheres, with values of 6.1%/decade in the NH and 5.4%/decade in the SH (see Figure 1.7). At lower latitudes (50° - 64° latitude) they found smaller trends, which contradicts previous suggestions that PMC brightness should most rapidly change at the most equatorward latitudes since there the clouds are on the brink of existence. It is possible, however, that inconsistencies at equatorward latitudes reflect the inability of SBUV to observe very faint and patchy clouds (see Section 1.6).

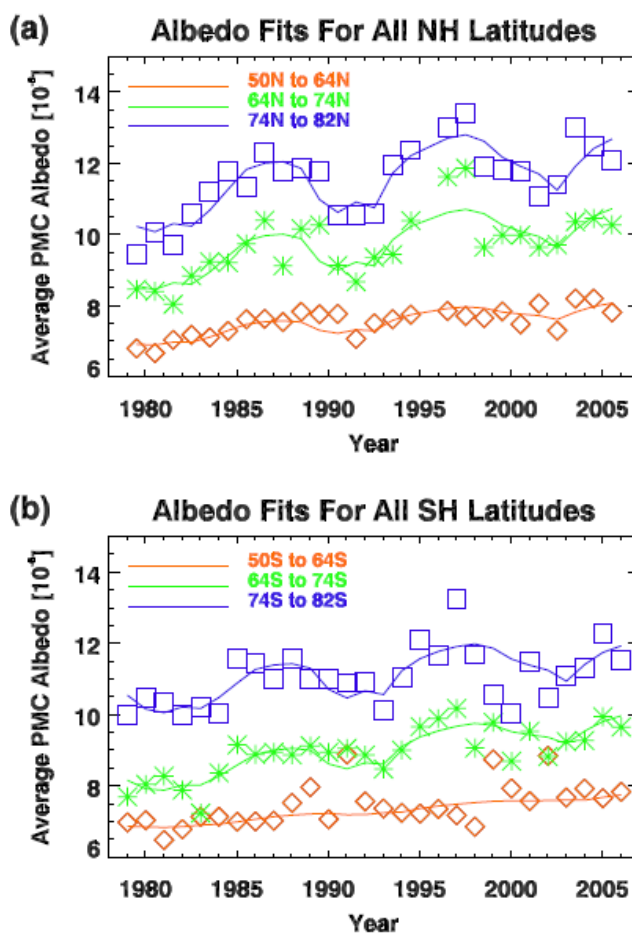


Figure 1.7: SBUV PMC seasonal averaged albedo and multiple linear regression fits for three NH (a) and SH (b) latitude bands. From DeLand *et al.* [2007], Figure 7⁶.

⁶ Reproduced by permission of American Geophysical Union. DeLand, M. T., Shettle, E. P., Thomas, G. E. and Olivero, J. J., Latitude-dependent long-term variations in polar mesospheric clouds from SBUV version 3 PMC data, *Journal of Geophysical Research-Atmospheres*, 112, D10315, 2007. Copyright [2007] American Geophysical Union.

Observed PMC trends have thus far not been conclusively tied to either temperature or water vapor trends in the polar summer mesopause region. Olivero and Thomas [2001] and Beig *et al.* [2003] showed that observed temperature trends in the upper mesosphere are inconclusive. Several studies in the past showed a non-existent or weak trend in temperature [e.g., Lowe, 2000; Lübken *et al.*, 1999 in comparison to Theon *et al.*, 1967; Lübken, 2000], whereas other studies, mostly using rocket soundings, presented large trends [e.g., Golitsyn, 1996; Dunkerton *et al.*, 1998], however with significant uncertainties [Beig *et al.*, 2003]. Updated results by Beig [2011], summarizing the findings of the recent literature, and indicate of weak annual mean negative trends in the mesopause region temperature. Nedoluha *et al.* [2003] used measurements from several satellite instruments to show that there is no statistically significant trend in mesospheric water vapor, even though episodic changes in water vapor may indicate strong trends during some time ranges and no trend during others. This behavior is due to high-frequency variability in water vapor from the Quasi-Biennial Oscillation (QBO), volcanic eruptions, and El Niño/La Niña-Southern Oscillation (ENSO) [Garcia *et al.*, 2007].

Atmospheric models predict a cooling of <1 K/decade in the mesopause region [Beig *et al.*, 2003], or no significant trend at all [Garcia *et al.*, 2007]. A trend of <1 K/decade is close to the lower limit of observed non-zero trend results, and also within the error bars in zero trend results. Model trends of water vapor are only significant if episodic changes are averaged out over a long time range, e.g., from 1950 to 2003 as shown by Garcia *et al.* [2007]. They show an annual water vapor trend in the upper stratosphere and mesosphere of up to 4%/decade in the absence of PMCs.

Thomas [1996] presented the simulated sensitivity of PMC brightness to changes in mesopause temperature and water vapor. Figure 1.8 shows that even a modest change, e.g., a

25% change in water vapor or a 2-3 K change in temperature, may cause a doubling of cloud brightness. Assuming that there is a small trend in mesopause temperature, e.g., 0.5 K/decade, that is not currently detectable from observations, it may well be that this small trend is responsible for the trend in PMC brightness that has been observed in satellite data over the last three decades.

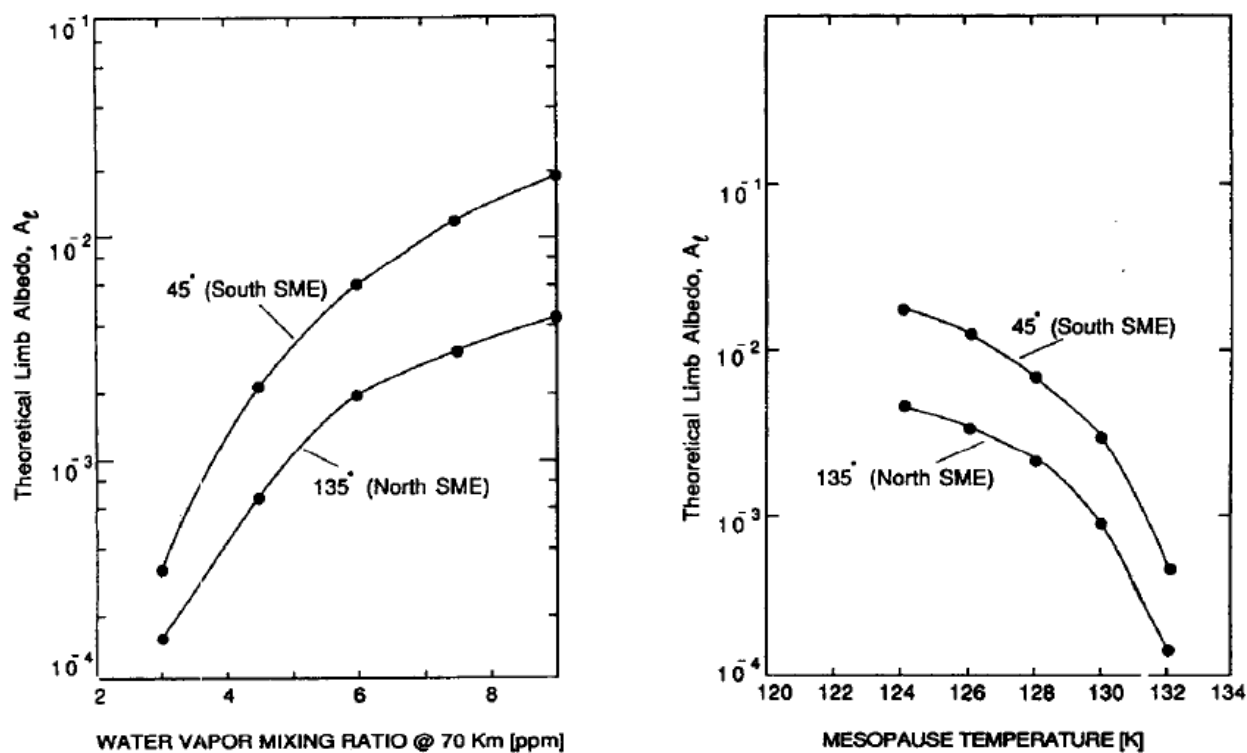


Figure 1.8: Simulated limb brightness of PMC as seen from orbiting spacecraft [Jensen, 1989]. Left panel: two curves show brightness for two different scattering angles appropriate to the SME satellite viewing geometry for a constant temperature of 128 K. Right panel: same, but for a constant water vapor mixing ratio of 6 ppmv at 70 km. From Thomas [1996], Figure 15⁷.

Long-term trends in PMCs can also be affected by dynamical processes. That is, every process that changes the meridional temperature gradient will also affect zonal mean winds through the thermal wind relationship. Changes in zonal mean winds then affect wave filtering

⁷ Reprinted from Journal of Atmospheric and Terrestrial Physics, 58, Thomas, G. E., 1996, Global change in the mesosphere lower thermosphere region: Has it already arrived?, 1629-1656, Copyright (1996), with permission from Elsevier.

and momentum deposition from breaking waves. One example is how changes in the Antarctic ozone hole over the last three decades have affected the mesospheric circulation and therefore PMCs as described by Smith *et al.* [2010]. The loss of ozone each spring since 1980 has led to a decrease in lower stratospheric temperatures, which corresponds to stronger eastward zonal winds in the Antarctic stratosphere that affect the GW filtering. Smith *et al.* [2010] find that these GW filtering changes lead to a weakening of the SH summer upwelling between 65 and 80 km accompanied by an increase in SH temperature. As the ozone hole has continually deepened over the last three decades, it is expected to affect PMCs, specifically the timing of the PMC onset, with a trend towards later PMC onset dates. A discussion of this dynamically induced trend in the SH PMC onset is provided in Section 3.1.

Another factor that may influence trends in PMCs could be the increased number of space shuttle launches. During launch space shuttle exhaust is injected into the atmosphere near 110 km altitude. The water vapor plume can be transported into the polar mesopause region to form PMCs [Stevens *et al.*, 2003]. Stevens *et al.* [2005b] have shown that space shuttle exhaust can be an important global source of both PMC formation and variability. During the 1980s, 2-3 times more shuttles were launched successfully than in the 1970s. Hence it cannot be excluded that PMC trends may be influenced by increased space shuttle launches. Any trends observed in PMCs may therefore be due to a combined effect of global climate change and increased number of shuttle launches.

1.4 PMC observations

1.4.1 Early history of PMC observations: human observations

When the Krakatoa volcano erupted in 1883 and destroyed the Krakatoa Island in Indonesia (6°S), the massive input of volcanic ash into the stratosphere caused uncommon twilight phenomena, e.g., remarkably brilliant sunsets, which caused observers to take careful note of the twilight sky [Gadsden and Schröder, 1989]. The first observation of a PMC followed two years later, by Backhouse in Germany on 8 June 1885 [Backhouse, 1885]. The observations of increased airglow due to Krakatoa volcanic aerosol particles and the first observation of PMCs formed a new science discipline: Aeronomy, the physics of the upper atmosphere [Schröder, 2001]. Other prominent PMCs were observed in late June and July of 1885 by many observers [Schröder, 2001]. Leslie first mentioned PMCs [Leslie, 1885], and shortly after, PMCs were also described by Teraskii in Russia [Teraskii, 1890] and by Jesse in Germany [Jesse, 1885; 1886].

It was Jesse who took the first photographs of PMCs in 1887 and got funded by the Berlin Academy of Science to establish a PMC observatory in Berlin-Steglitz in the same year [Gadsden and Schröder, 1989]. Jesse's main contributions are plentiful: during his systematic photographic monitoring between 1885 and 1899 he gave the first proof of the existence of clouds at 82.08 ± 0.1 km on average. Jesse quantified the direction and velocity of PMC movements: he estimated the speed in the zonal direction to be ~ 109 m/s and the speed in meridional direction to be ~ 53 m/s. Jesse also wrote a manual for PMC observations and encouraged non-European monitoring of PMCs. He considered the origin of PMCs, but due to limited knowledge at the time of temperature, composition, or circulation at 80 km, he could not present a generally valid theory of PMCs. Jesse thought that there must be a connection between the Krakatoa eruption in 1883 and the beginning of PMC observations in 1885, proposing that

PMCs consist of small crystals originating from the material that was distributed into the upper atmosphere after the Krakatoa eruption [see also Förster, 1906]. Wegener [1912] suggested that PMCs were ice clouds nucleating on material from the Krakatoa eruption. However, some big eruptions did not seem to be connected with an increase in PMC activity as expected, e.g., the Mt. Katmai, Alaska, eruption of 1912 [Thomas, 1991]. On this basis, Jardetzky [1926] rejected a volcanic origin completely, suggesting that PMCs were to be seen irrespective of volcanic activity and proposing a simple ice crystal model.

Another theory was proposed by Vestine [1934], who suggested that extraterrestrial particles from great meteor showers and bright comets between 1880 and 1887 could explain the high number of PMC observations at that time. A brilliant PMC display following the atmospheric entry of the famous Tunguska object in Russia on June 30, 1908 pointed toward a cosmic origin of PMCs [Thomas, 1991]. Around the same time, Humphreys [1933] and Martyn and Pulley [1936] advocated ice condensation due to a strong temperature minimum of ~ 180 K at PMC altitude. Since this temperature still seemed too high considering the small amount of stratospheric moisture suggested by Brewer [1949], again dust particles of terrestrial origin creating a “haze top” were brought forward by Ludlam [1957]. However, there were several issues with this suggestion: neither did it explain the seasonal dependence or the existence of PMCs at southern latitudes during summer, nor why PMCs were only observed at high latitude even though meteoric flux is highest towards equatorward latitudes. In addition to these doubts, PMC observations could not be correlated with appearances of major meteor showers.

Since 1930 suggestions have been made of a solar cycle dependence of PMCs, with more clouds being observed during solar minimum [Gadsden and Schröder, 1989, and references therein]. However, this connection stood on shaky ground because the historical PMC database

was inadequate due to statistical non-uniformity from year to year; the number of observers and their competence greatly varied since 1885. In addition, observational factors like the weather were convoluted with real PMC variability. Improvements were made after 1957, when dedicated ground-based networks of both professional and amateur observers were established [e.g., Gadsden, 1998]. As mentioned above, when Gadsden [1998] found a two year time lag between solar activity and PMCs using these ground observations, he shed doubt on a possible physical connection between the two phenomena since such a big time lag is not consistent with the rapid lifetime of photodissociation of water vapor.

Until 1964, the existence of PMCs in the SH was in doubt, since only three observers reported seeing PMCs in the SH [Gadsden and Schröder, 1989]. Observations during the SH summer of 1964/1965 and 1965/1966 finally confirmed the presence of PMC in the SH [Fogle and Haurwitz 1966].

A long data record of PMC observations from human observers on the ground is extremely valuable; however, several factors complicate the usefulness of visual PMC reports for long-term studies [DeLand *et al.*, 2006a]. First, PMC observations are only possible during a few hours around twilight. However, surface weather conditions are often not favorable at PMC observation locations during the summer. Second, since PMCs cannot be observed against a bright polar summer night sky, PMCs can only be seen up to latitudes of $\sim 65^\circ$ [Klostermeyer, 2002]. Third, in spite of the existence of several observational networks in the northern hemisphere, the spatial coverage is still not ideal, with many gaps over land and no coverage over the ocean. In the SH, there are even less PMC observations due to much smaller population density between 50°S and 65°S [Warren *et al.*, 1997]. This hampers the detection of hemispheric differences. Fourth, the quality of PMC observations for detection of long-term change and solar

cycle signal depends critically on the training of PMC observers. Before 1957 there were only scattered reports from untrained observers, making it impossible to find a solar cycle signal in the pre-1964 records [Fogle and Haurwitz, 1966]. Kirkwood *et al.* [2008] report the most current PMC trends and variations as observed by professional and voluntary ground observers in the UK and Denmark between 1964 and 2006, and find reasonable agreement with satellite observations of solar cycle effects on PMCs. Finally, a possible long-term trend in PMC brightness is hard to quantify using ground observations of PMCs. Kirkwood *et al.* [2008] did not confirm a statistically significant long-term trend in moderate or bright PMCs, and their observed significant trend in faint PMCs may be due to changes in observational practices or increasing skill of observers in identifying faint PMCs. In summary, PMC observations from the ground do not offer an ideal database for quantification of long-term trends in PMCs.

A new era of PMC or PMC research started with the International Geophysical Year (1957-58), in which PMCs were a central part of the observations and interest in the upper atmosphere was renewed. However, there was still little known about the constitution of the upper atmosphere at that time, and the composition of PMCs was still unclear. Many new insights came from rocket launches that started in 1962, satellites detecting PMCs from 1969 on, and other observation methods such as lidar.

1.4.2 Rocket launches

A first sampling of PMC particles and in-situ observations of temperature and water vapor became possible through rocket experiments. The first rocket campaigns for characterizing PMC particles started in August 1962 in Sweden. The rockets carried a variety of particle collectors

that were exposed between 75 and 98 km during the ascent of the rocket [Hemenway *et al.*, 1964]. Particles were collected using some kind of coated surface, and evidence was found for water coated particles. However, the size of those particles was difficult to quantify due to melting of the ice sphere and the subsequent flattening, spreading out or shaking across the detector. Comparison of two rocket flights, one through a PMC and one in the absence of a PMC, showed that the particle concentration in the sampled layer was at least 1000 times greater in the presence of clouds than during cloud-free conditions.

Rocket flight experiments continued throughout the years, with different kinds of collectors and detectors. Current detectors have evolved considerably compared to those first rocket launches. During the combined ECOMA (Existence and Charge state Of Meteor smoke particles in the middle Atmosphere) /MASS (Mesospheric Aerosol Sampling Spectrometer) sounding rocket campaign, a newly developed particle detector was used to quantify PMC and PMSE ice particle volume density, mass, radii and number densities [Rapp and Strelnikova, 2009; Strelnikova *et al.*, 2009; Rapp *et al.*, 2009]. The measurements clearly showed meteor smoke particle signatures throughout the whole mesosphere [Strelnikova *et al.*, 2009], with ice volume densities of $2\text{--}8 \times 10^{-14} \text{ cm}^3/\text{cm}^3$, particle radii of 20 – 40 nm, and particle number densities of $400\text{--}1400 \text{ cm}^{-3}$. However, radii and number density estimates are significantly more uncertain than ice volume density estimates since assumptions about the still unknown composition of particles must be made [Rapp *et al.*, 2009].

The first mesospheric temperature derivations were carried out in the 1960s using several techniques: the pitot tube technique [Horvath *et al.*, 1962], the rocketborne acoustic grenade technique [Nordberg *et al.*, 1965; Theon *et al.*, 1967] and the falling spheres technique [Schmidlin *et al.*, 1991; Lübken *et al.*, 1994; Lübken *et al.*, 1999; Lübken and Müllemann,

2003]. Only the falling spheres technique will be described here in detail. A small sphere made of metalized mylar is transported to an altitude of about 110 km by a small rocket. After release the sphere inflates to a diameter of 1 m and passively falls through the atmosphere. Increasing density with decreasing altitude decelerates the fall of the sphere. The sphere is tracked by a high-precision radar. The descent trajectory is used to calculate atmospheric density and horizontal winds. Assuming hydrostatic equilibrium, the density profile is integrated downward into a temperature profile. This method does not determine the temperature at the upper boundary, thus the start temperature needs to be taken from independent measurements or a model [Lübken *et al.*, 1994]. The falling spheres technique showed for the first time that the summer mesopause temperatures at polar latitudes (78°N and 68°S) can reach values of about 130 K [Lübken *et al.*, 1999; Lübken and Müllemann, 2003].

1.4.3 Lidar observations

The first lidar observation of a PMC took place at Andenes, Norway during the night of August 5/6, 1989; the PMC was determined to exist between 82.2 and 83.4 km [Hansen *et al.*, 1989]. Lidars emit laser pulses and detect the backward scattered signal from an object. From the elapsed time between emission and detection of the signal, the distance between the laser and the scattering object is calculated. Depending of the type of laser, lidars can also measure vertical profiles of temperature and other constituents in the middle atmosphere. The narrow-band sodium (Na) laser used by Hansen *et al.* [1989] operates at a wavelength of 589.159 nm, the D₂ resonance line of sodium. Na is present in the atmosphere between 80 and 100 km, with a peak density of several 10^9 atoms m⁻³ [Fricke and von Zahn, 1985]. The sodium D₂ line consists of six hyperfine transitions, which at atmospheric temperatures blend together into two components,

called D_{2a} and D_{2b} [Chamberlain *et al.*, 1958], separated by 2 pm. Due to Doppler broadening, the width of these two components broadens to an extent that depends on temperature. At the low pressures found in the mesopause region, pressure broadening is negligible. Doppler broadening can be detected by a narrow-band, powerful lidar with a sensitive detection system probing at several or at least two wavelengths, the maximum of the D_{2a} line and the intermediate minimum between the D_{2a} and D_{2b} line [Fricke and von Zahn, 1985]. The two or more resulting intensities at different wavelengths can then be converted to an atmospheric temperature. A very similar lidar is the potassium (K) lidar that uses the K resonance line at 769.9 nm. Another example of a widely used lidar type is the Rayleigh-Mie-Raman (RMR) lidar, which is capable of sounding the middle atmosphere in daylight and at three widely separated wavelengths [von Zahn *et al.*, 2000].

For more than 20 years, lidars have been used to observe variability of PMC occurrence and layer parameters on various time scales ranging from minutes to decades, including effects of GWs, tides, and solar cycle on PMCs. Lidar measurements are highly accurate and have high temporal and vertical resolution. They are ideally suited for observing local time effects on PMCs, temporal and vertical structure of temperature, number density, ice particle radius, and particle shape, GW effects on PMCs, as well as solar cycle effects. Lidars suffer from interruptions due to weather conditions and are limited to observations at fixed geographic locations. Therefore lidars are complemented by observations from non-geostationary polar orbiting satellite instruments, which provide daily spatial mapping of the polar regions independent of tropospheric weather.

The first lidar observation of a PMC by Hansen *et al.* [1989] during the night of August 5/6, 1989, at Andenes, Norway (69°N, 16°E) showed PMC altitudes ranging from 83.4 to 82.2

km, with an average altitude of 82.6 ± 0.1 km. Von Cossart *et al.* [1997] and von Zahn *et al.* [1998] confirmed these observations by reporting PMC mean altitudes over Alomar, Norway (69°N , 16°E) of 83.0 km and 82.7 km. SH PMC lidar observations by Chu *et al.* [2001a; b; 2003; 2004] and Gardner *et al.* [2001], both over the South Pole and Rothera (67.5°S , 68°W), provided insights into seasonal and latitudinal variations as well as hemispheric differences in PMC altitudes. Chu *et al.* [2004] revealed that SH PMCs had an ~ 1 km higher mean altitude than NH PMCs at similar latitudes; they also reported weaker and less frequent PMCs in the SH. Chu *et al.* [2006] found a symmetric and nearly Gaussian distribution of PMC altitudes, and a non-Gaussian distribution of PMC brightness, with cloud brightness being anti-correlated with cloud altitude. Lidar observations of local time effects on PMCs were reported by Chu *et al.* [2001a; 2003; 2006] and Fiedler *et al.* [2005; 2011], showing strong semidiurnal and diurnal oscillations in PMC altitudes, brightness, and frequency. Fiedler *et al.* [2011] emphasized that diurnal and semidiurnal amplitudes as well as phases show pronounced year-to-year variations, which has implications for long-term trend analysis by instruments that do not observe the full diurnal cycle like SBUV. Using lidar observations at Alomar, solar cycle effects on PMCs are found to be quite controversial, with an anti-correlation before 1994 and no dependence after 1994 [Fiedler *et al.*, 2009].

PMC particle size and shape have been inferred from lidar observations through multi-wavelength and polarization techniques. The determination of PMC size distribution through observations at three or more wavelengths was first presented by von Cossart *et al.* [1999] and Alpers *et al.* [2000]. Assuming spherical ice particles with a monomodal lognormal size distribution, their combined results are median radii of 20.2 nm to 72 nm, size distribution widths of 1.2 to 1.64 (width unit is unity for a lognormal size distribution), and number densities of 30

to 610 cm^{-3} . Many studies followed, e.g., Baumgarten *et al.* [2007; 2008; 2010], investigating the sensitivity of particle radius, size distribution width, and number density to particle shape (spherical or aspherical) and size distribution (Gaussian or lognormal). Baumgarten *et al.* [2002] observed the polarization state of 532 nm laser light and found unexpectedly large depolarization, from which they inferred that particles are elongated with a length-over-diameter ratio of > 2.5 . Baumgarten *et al.* [2010] observed a quasi-linear relationship between distribution width and mean particle size for particles sizes $< 40 \text{ nm}$, and a size distribution width that is nearly independent of particle size for particles with mean radii $> 40 \text{ nm}$.

Quite a few lidar studies found an anti-correlation of GW activity in the upper stratosphere and PMCs at Sondstrom in Greenland at 67°N [e.g., Gerrard *et al.*, 1998; 2004 and Thayer *et al.*, 2003]. Innis *et al.* [2008], however, observing PMCs in Davis, Antarctica (68°S , 77°E), did not find a relationship between observed stratospheric GW activity and PMC occurrence. Chu *et al.* [2009] consolidated these contradictions by reporting a background temperature dependent response of PMC brightness to stratospheric GWs, comparing observations from the South Pole and Rothera. They hypothesize that in regions of relatively high temperatures, GWs induce temperature perturbations that can destroy growing ice crystals or limit their growth. In contrast, in very cold regions, GW perturbed temperature may never be above the frost point, and thus GW activity has less impact on crystal growth and PMC brightness.

1.4.4 Satellite observation overview

The first detection of PMCs during daytime from the Orbiting Geophysical Observatory (OGO-6) was described by Thomas and Donahue [1972]. About a decade later Thomas [1984]

showed PMC detections using SME. About the same time another instrument was launched into orbit that is still used on different satellites until today: the Solar Backscatter UltraViolet (SBUV) instrument. All of these PMC measurements were serendipitous; the instruments had been designed to measure other quantities. The fact that PMCs were detected by instruments that were not designed to observe them would not change until the launch of the AIM satellite in 2007. Prior to AIM many different satellite instruments had been observing PMCs, sometimes because the presence of PMCs hampered their original retrievals. This section briefly describes the OGO-7 and SME instruments for historic context, lists other satellite instruments that have been used for PMC observation, and describes advantages and disadvantages of satellite observations. The AIM mission and SBUV are described in detail in Sections 1.6 and 1.7, respectively.

OGO-6 was launched in June 1969 into a polar orbit and observed PMCs until December 1970. It used a filter photometer that vertically scanned the horizon, observing green and yellow airglow. Its original objective was to determine the spatial distribution of sodium and atomic oxygen airglow emissions. Thomas and Donahue [1972] describe the OGO-6 instrument and its airglow observations in detail. The left hand-side of Figure 1.9 from Donahue *et al.* [1972] shows the typical slant emission rates for yellow airglow: the background emission due to Rayleigh scattering from gas molecules decreases slowly with increasing altitude, with the yellow airglow layer being detected as an enhancement of the Rayleigh background above 65 km. The right hand-side of Figure 1.9 shows PMCs at a higher latitude as a very bright and narrow emission layer peaking near 83 km. Donahue *et al.* [1972] observed PMCs as thin and intense scattering layers at 75 - 90 km altitude and at polar latitudes, starting 15 days before summer solstice and visible almost always at latitudes around 85°. They also observed a

latitudinal dependence of PMC optical depth, with optical depths increasing by a factor of 50 to 100 between 65° and 80° latitude.

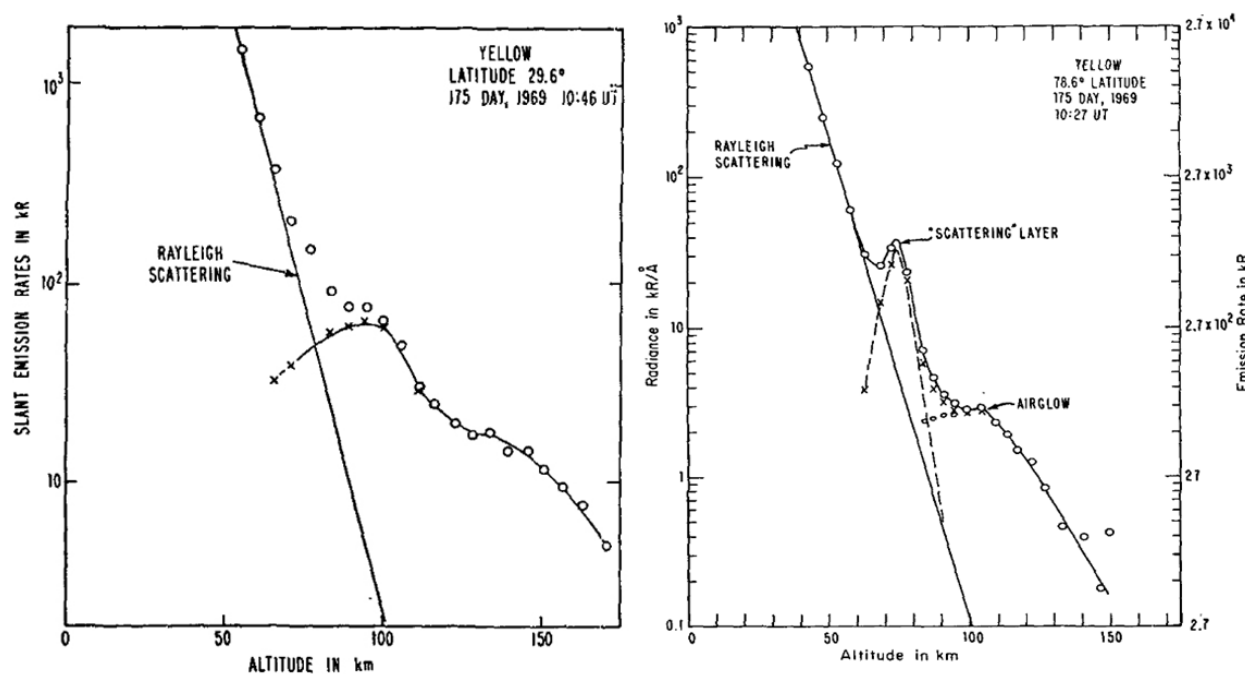


Figure 1.9: Slant emission rates observed by OGO-6 airglow photometer at 589 nm on June 24 1969 at 29.6°N (left) and 78.6°N (right). From Donahue *et al.* [1972], Figures 1 and 2⁸.

About a decade later, SME was launched in October 1981 into a polar sun-synchronous orbit. SME's original goal was the comprehensive study of mesospheric ozone and the processes which form and destroy it, and to do a rigorous test of photochemical ozone theories [Thomas *et al.*, 1980]. SME hosted five instruments that measured mesospheric ozone as well as solar ultraviolet (UV) irradiance, temperature, pressure, water vapor, nitrogen dioxide concentrations and airglow. One of the instruments was the Ultraviolet Spectrometer Experiment (UVS), a limb scanning instrument continuously measuring solar irradiance in the spectral region from 160 to 310 nm (in which molecular oxygen and ozone are dissociated) in addition to Lyman-alpha at

⁸ Donahue, T. M., Blamont, J. E. and Guenther, B., 1972. Noctilucent Clouds in Daytime - Circumpolar Particulate Layers near Summer Mesopause. *Journal of the Atmospheric Sciences*, 29, 10.1175/1520-0469(1972)029<1205:NCIDCP>2.0.CO;2. (c) American Meteorological Society. Reprinted with permission.

121.6 nm (where water vapor is dissociated). These wavelength regions were used to measure molecular oxygen, ozone, and water vapor. Using SME observations, Thomas [1984] showed that a typical PMC season usually begins around 20 days before summer solstice and lasts approximately 90 days. PMCs first appear at highest latitudes and gradually appear at lower latitudes poleward of 55° latitude. He was also the first to show hemispheric differences in the latitudinal range of PMCs: NH PMC usually occurred about 5° more equatorward than their SH counterpart. Due to the short time of observation (5 years between 1981 and 1985), no dependence of PMC occurrence on solar variability or the existence of a long-term trend could be shown.

Between 1978 and the present, instruments in the SBUV series (SBUV and SBUV/2) were flying on different satellites (Nimbus-7, NOAA-9, NOAA-11, and NOAA-14) and are currently flying on NOAA-16, NOAA-17, NOAA-18, NOAA-19. For brevity, the SBUV and SBUV/2 instruments will be referred to as SBUV. The primary purpose of SBUV is to monitor the global distribution of the stratospheric vertical ozone profile and total column ozone [DeLand *et al.*, 2003]. A more detailed description of the SBUV instrument and the PMC detection algorithm is given in Section 1.6.

Many other instruments besides OGO-6, SME, and SBUV have measured PMCs. These include the WIND Imaging Interferometer (WINDII) [Evans *et al.*, 1995], the Polar Ozone and Aerosol Measurement (POAM) II [Debresterian *et al.*, 1997] and III instruments, the Ultraviolet and Visible Imaging and Spectrographic Imaging (UVISI) instrument [Carbary *et al.*, 1999; 2003], the Middle Atmosphere High Resolution Spectrograph Investigation (MAHRSI) [Stevens *et al.*, 2001], the Cryogenic Infrared Spectrometers and Telescopes for the Atmosphere (Christa) [Stevens *et al.*, 2001], the Student Nitric Oxide Explorer (SNOE) [Bailey *et al.*, 2005], the

Halogen Occultation Experiment (HALOE) [Hervig *et al.*, 2001], the Optical Spectrograph and InfraRed Imager System (OSIRIS) [Petelina *et al.*, 2005], the Michelson Interferometer for Passive Atmospheric Sounding (MIPAS) [López-Puertas *et al.*, 2009], the Spatial Heterodyne Imager for Mesospheric Radicals (SHIMMER) [Stevens *et al.*, 2009], the SCanning Imaging Absorption SpectroMeter for Atmospheric CartograpHY (SCIAMACHY) [Robert *et al.*, 2009], the Atmospheric Chemistry Experiment Fourier Transform Spectrometer (ACE-FTS) [Eremenko *et al.*, 2005], and the Ozone Monitoring Instrument (OMI) [DeLand *et al.*, 2010]. Figure 1.10 shows the timeline of instruments that have observed PMCs from space.

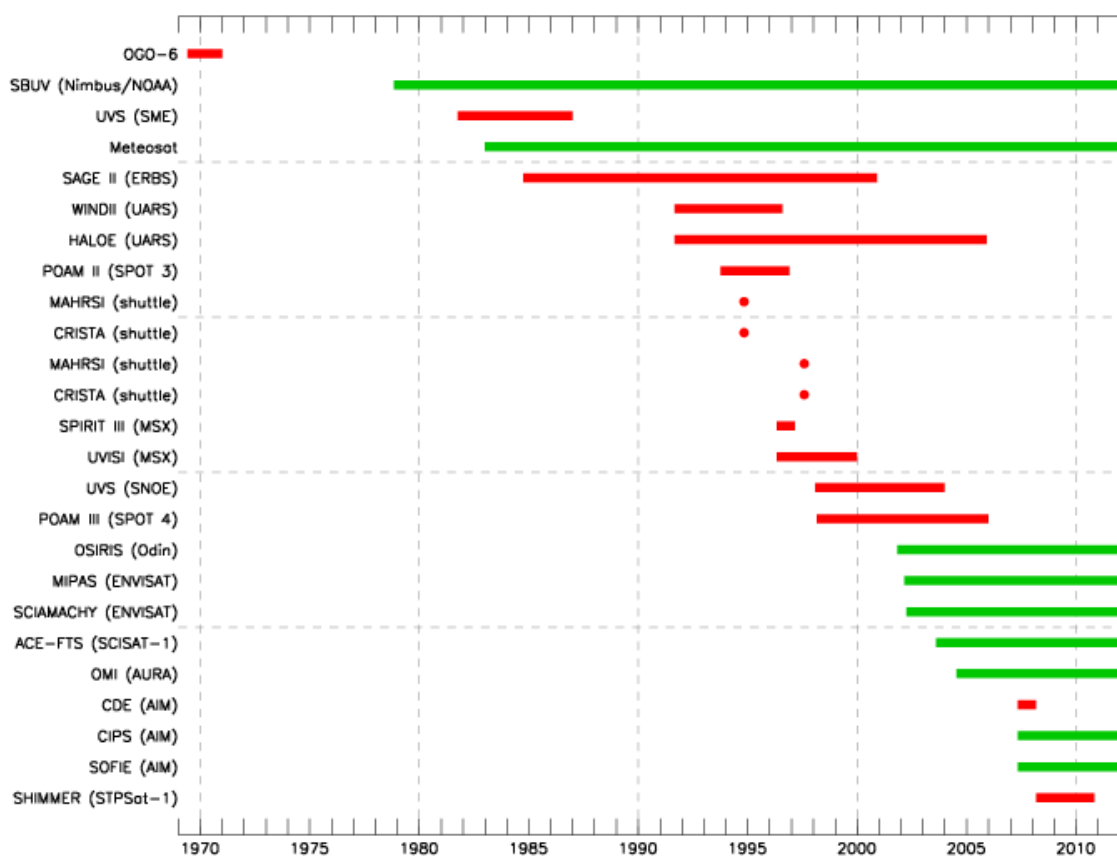


Figure 1.10: Timeline of satellite instruments observing PMCs (satellite platforms in parentheses). Green arrows indicate instruments that are collecting data as of February 2012. Red bars indicate instruments that are no longer active.

Satellite observations of PMCs have several advantages over ground based observations. First, satellite observations are not influenced by tropospheric weather like human observers and lidars. Second, satellites have the advantage of much broader coverage. Non-geostationary, polar orbiting satellites have evenly spaced longitude coverage over the entire planet. Solar occultation instruments in near polar orbits, like POAM or SOFIE, have limited latitude coverage on any given day, but sample an entire circle of latitude in the summer polar region at evenly spaced longitudes $\sim 25^\circ$ apart. Solar occultation instruments in lower inclination orbits might sample the summer polar region on only a few days at a time. Nadir or limb scattering or emission instruments, such as CIPS, SNOE or OSIRIS, sample nearly the entire summer polar region each day. The number of opportunities per day for observing PMCs also depends on the instrument: a solar occultation instrument like SOFIE has only 14-15 chances for observing a cloud, whereas nadir and limb viewing instruments like for example SBUV, CIPS and SNOE have a few hundred to a few thousand potential PMC measurements each day. Where solar occultation struggles with global coverage, it shines with vertical resolution that can be as high as 0.7 km in the case of the POAM II instrument [Debresterian *et al.*, 1997]. One disadvantage of satellite observations lies in their local time coverage: Sun-synchronous satellites observe only two local times at any given latitude. Lidars with their very fine temporal (and vertical) resolution are thus much better suited for local time studies than sun-synchronous satellites.

In April 2007 the AIM satellite was launched with the explicit goal to study PMCs. Both AIM and SBUV are primary instruments/satellites for this thesis; hence they are described in more detail in Sections 1.6 and 1.7, respectively.

1.5 AIM

The AIM mission is the first satellite mission dedicated to the study of PMCs. It was launched on April 25, 2007 into a polar, sun-synchronous orbit at an altitude of ~600 km with equator crossing times of 12:00 AM/PM and is currently still operating. The overall goal is to resolve why PMCs form and why they vary, specifically to quantify the connections between the clouds and the meteorology of the polar mesosphere [Russell *et al.*, 2009]. AIM carries three instruments that provide information about PMCs and their environment: SOFIE, CIPS, and the Cosmic Dust Experiment (CDE).

1.5.1 CDE

CDE is an in-situ cosmic dust detector designed to observe the influx of cosmic matter at the satellite altitude of 600 km due to impact on twelve thin, permanently polarized polyvinylidene fluoride foils (channels). Background noise is measured on two identical sensors on the back side of CDE, which is shielded from particle impact. The time, channel number and impact charge of each particle hit are recorded. When cosmic matter reaches the mesosphere it ablates to become meteoric smoke, which is considered the most likely candidate for PMC nuclei by Rapp and Thomas [2006]. These ablated meteoric dust particles are assumed to have sizes around 0.2 nm, and coagulate to PMC nucleation sites of ~1 nm [Bardeen *et al.*, 2008]. It was expected that temporal variations of meteoric dust particles could be used to assess the role of meteoric dust on PMC formation and variability. CDE experienced noise issues that were addressed successfully with noise filtering algorithms. However, after a safehold event in February 2008, even more noise and failing channels inhibited CDE data analysis completely. Even though the reduced data has low signal to noise ratios, it shows an average dust flux that is

consistent with previous measurements. Despite high error bars there is evidence of temporal variability throughout the year on the order of a factor of two. CDE results confirm previous studies that showed an asymmetric hemispheric behavior, with more dust entering the NH than the SH [Poppe *et al.*, 2011].

1.5.2 SOFIE

SOFIE is a solar occultation differential absorption radiometer covering wavelengths between the UV and near infrared (IR). It provides vertical profiles of temperature, trace gas abundance (O_3 , water vapor, CO_2 , CH_4 , and NO), and PMC extinction [Gordley *et al.*, 2009]. During a solar occultation, solar intensity is monitored as the satellite enters or exits the Earth's shadow; hence SOFIE observes only 14 or 15 vertical profiles of its measured species per day on a circle of latitude in each hemisphere that varies slowly between 65° and 85° . The atmospheric transmission is the ratio of solar intensity measured through the atmosphere to the exoatmospheric solar intensity. Vertical profiles of atmospheric transmission are determined within eight channels or 16 spectral bands between 0.29 and $5.32 \mu m$. Figure 1.11 shows simulated PMC spectra in the SOFIE spectral channels. In each channel two radiometer measurements are taken, one located in a wavelength region of strong absorption and one in a spectrally adjacent region of weaker absorption of the targeted species [Gordley *et al.*, 2009]. Table 1 shows the SOFIE channel characteristics. Sensitivity to ice mass density is obtained from measurements at the ice absorption peak near $3.0 \mu m$, whereas particle sizes are derived from the combination of ice absorption measurements in the IR and scattering measurements at wavelengths shorter than $\sim 1.5 \mu m$ [Gordley *et al.*, 2009]. More details about the SOFIE

measurements and algorithms are presented by Gordley *et al.* [2009], Hervig *et al.* [2009a], and Hervig *et al.* [2009b].

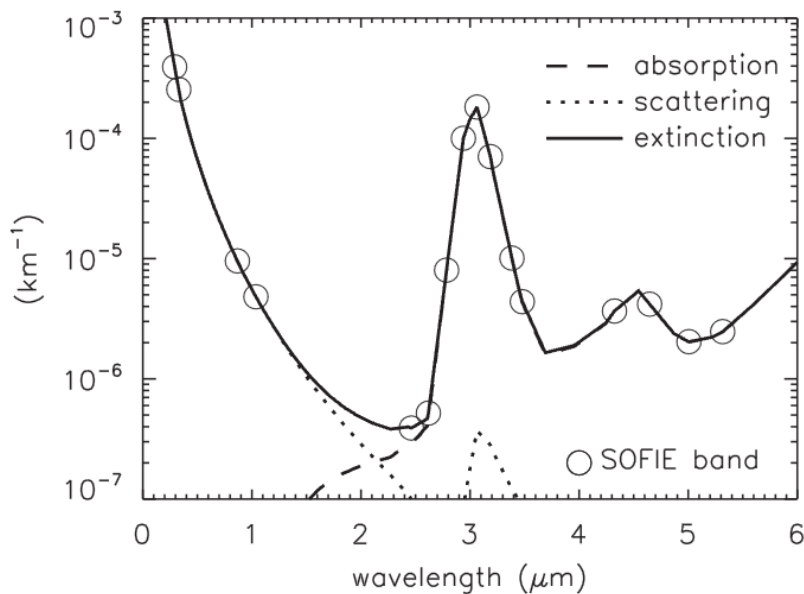


Figure 1.11: PMC scattering, absorption, and extinction spectra modeled using the average PMC size distribution from von Cossart *et al.* [1999]. From Gordley *et al.* [2009], Figure 1⁹.

⁹ Reprinted from *Journal of Atmospheric and Solar-Terrestrial Physics*, 71, Gordley, L. L., Hervig, M. E., Fish, C., Russell, III, J. M., Bailey, S., Cook, J., Hansen, S., Shumway, A., Paxton, G., Deaver, L., Marshall, T., Burton, J., Magill, B., Brown, C., Thompson, E. and Kemp, J., The solar occultation for ice experiment, 300-315, Copyright (2008), with permission from Elsevier.

Table 1: SOFIE channel characteristics. From Gordley *et al.* [2009], Table 1¹⁰.

Channel	Band	Target ^a	Center λ (μm)	$G_{\Delta V}$	Detector ^b
1	1	O ₃ s	0.292	30	SiC, PV
	2	O ₃ w, p	0.330		SiC, PV
2	3	PMC s	0.867	300	Ge, PV
	4	PMC w	1.037		Ge, PV
3	5	H ₂ O w, p	2.462	96	HgCdTe, PC
	6	H ₂ O s	2.618		HgCdTe, PC
4	7	CO ₂ s	2.785	110	HgCdTe, PC
	8	CO ₂ w, p	2.939		HgCdTe, PC
5	9	PMC s	3.064	120	HgCdTe, PC
	10	PMC w	3.186		HgCdTe, PC
6	11	CH ₄ s, p	3.384	202	HgCdTe, PC
	12	CH ₄ w, p	3.479		HgCdTe, PC
7	13	CO ₂ s	4.324	110	HgCdTe, PC
	14	CO ₂ w, p	4.646		HgCdTe, PC
8	15	NO w, p	5.006	300	HgCdTe, PC
	16	NO s	5.316		HgCdTe, PC

^a s indicates strongly absorbing band, w denotes weakly absorbing band, and p denotes PMC measurement as a secondary target.

^b PV denotes photovoltaic, PC denotes photoconductive.

1.5.3 CIPS

The CIPS instrument is a panoramic imager consisting of four CCD cameras operating in a 10 nm passband centered at 265 nm [Russell *et al.*, 2009; McClintock *et al.*, 2009]. It measures UV radiation scattered in the direction of the satellite by clouds and the atmosphere. Using this wavelength takes advantage of the extremely low albedo below 50 km due to absorption of UV primarily by ozone. The CIPS field of view is 120° along track and 80° across track, or about 2000 x 1000 km. The CIPS observation strategy is to acquire successive "scenes" along the orbit path, in which the atmosphere is imaged with all four cameras simultaneously. CIPS scenes are taken every 43 seconds, which means that many locations are viewed at as many as seven

¹⁰ Reprinted from Journal of Atmospheric and Solar-Terrestrial Physics, 71, Gordley, L. L., Hervig, M. E., Fish, C., Russell, III, J. M., Bailey, S., Cook, J., Hansen, S., Shumway, A., Paxton, G., Deaver, L., Marshall, T., Burton, J., Magill, B., Brown, C., Thompson, E. and Kemp, J., The solar occultation for ice experiment, 300-315, Copyright (2008), with permission from Elsevier."

different scattering angles (SCAs) between 15° and 180° . This provides a direct measurement of the cloud scattering phase function, e.g., cloud albedo vs. SCA.

Figure 1.12 illustrates the CIPS scene: the along-track (X) cameras are labeled PX and MX (“plus” and “minus”), while the cross-track (Y) cameras are labeled PY and MY. The PX camera is always directed towards the sun. Fifteen orbits occur each day; and on each orbit, 27 overlapping, successive scenes together sample latitudes between about 40° and 87° . The big CIPS field of view and its near polar orbit thus result in complete coverage each day between latitudes of about 70° and 87° .

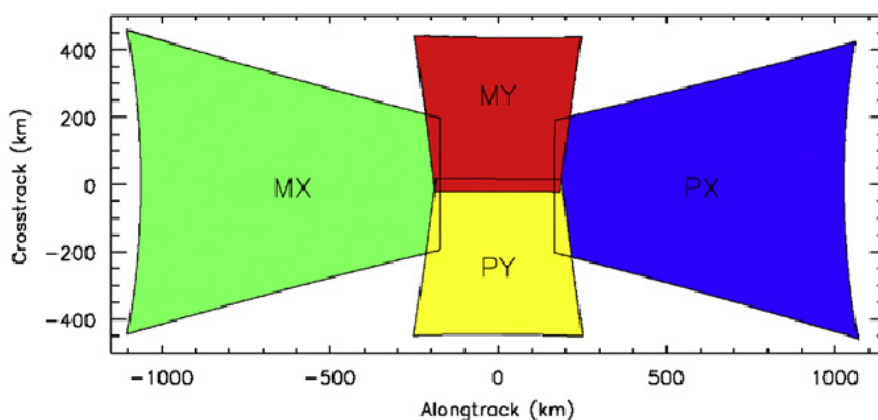


Figure 1.12: CIPS scene projection onto the atmosphere at an altitude of ~ 83 km. From McClintock *et al.* [2009], Figure 2¹¹.

The shape of the cloud scattering phase function is significantly different from the atmospheric background phase function, so clouds can be distinguished from the atmospheric background. The cloud phase function depends on cloud particle size, therefore the particles radius can be derived from the cloud phase function. Figure 1.13 shows that the cloud phase function differs most from the Rayleigh phase function at forward ($< 90^\circ$) SCAs, hence at

¹¹ Reprinted from Journal of Atmospheric and Solar-Terrestrial Physics, 71, McClintock, W. E., Rusch, D. W., Thomas, G. E., Merkel, A. W., Lankton, M. R., Drake, V. A., Bailey, S. M. and Russell, III, J. M., The cloud imaging and particle size experiment on the Aeronomy of Ice in the mesosphere mission: Instrument concept, design, calibration, and on-orbit performance, 340-355, Copyright (2008), with permission from Elsevier.

forward SCAs CIPS is most sensitive to clouds. As one would expect from the fact that the Rayleigh scattering phase function pertains to molecule-size or smaller scatterers, clouds with large mean particle sizes are easier to detect than clouds with small particle sizes.

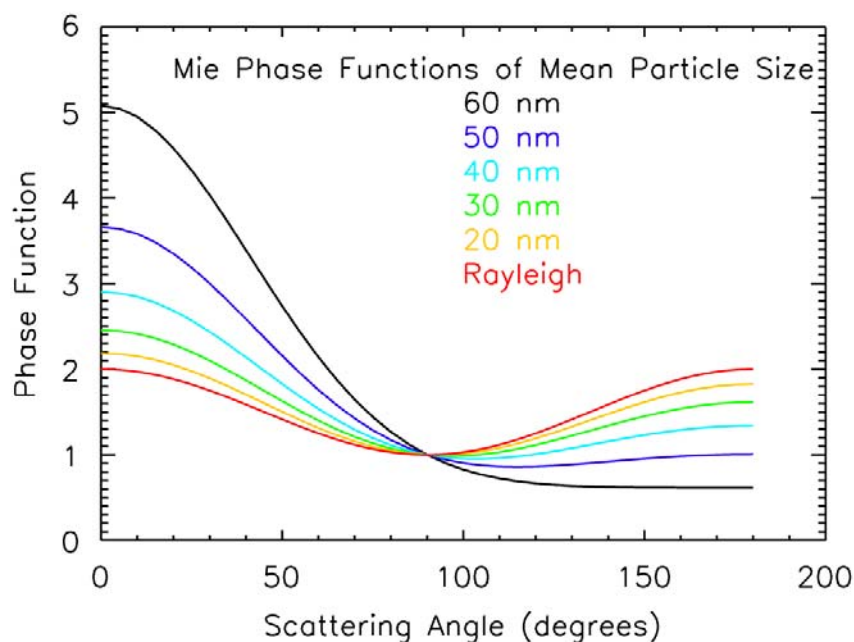


Figure 1.13: Mie scattering phase functions for particles with a range of typical PMC particle sizes show peaked forward scattering compared with Rayleigh scattering from atmospheric gases. From McClintock *et al.* [2009], Figure 1¹².

Figure 1.14 shows the range of SCAs as a function of SZA for one CIPS orbit. For clarity, only every fourth observation is plotted, as a single gray point. For selected locations, e.g., a certain cloud, the scattering profile is shown using asterisks connected by solid lines. Note that at higher SZAs, approximately half of the observations are at forward SCAs where CIPS is most sensitive to cloud detection. AIM was designed so that once every orbit, CIPS and SOFIE make simultaneous and co-located measurements with just a small time delay of six minutes. This region of common observations is called the ‘common volume’ or CV. The CV is located at

¹² Reprinted from Journal of Atmospheric and Solar-Terrestrial Physics, 71, McClintock, W. E., Rusch, D. W., Thomas, G. E., Merkel, A. W., Lankton, M. R., Drake, V. A., Bailey, S. M. and Russell, III, J. M., The cloud imaging and particle size experiment on the Aeronomy of Ice in the mesosphere mission: Instrument concept, design, calibration, and on-orbit performance, 340-355, Copyright (2008), with permission from Elsevier.

SZAs near 90° , or in the so-called "shadow band zone" where SOFIE observes the sunset or sunrise. Here CIPS is most sensitive since it observes at the most forward scattering angles and the Rayleigh background is minimized. The combination of PMC observations from CIPS and SOFIE has several advantages. SOFIE has very high vertical resolution; however, its optical slant path through the cloud is 290 km long [Gordley *et al.*, 2009]. If a cloud is observed away from the tangent point, the retrieved cloud altitude will be biased low. CIPS provides high-resolution horizontal information around the SOFIE slant path, which is helpful interpreting the SOFIE data. Additionally, simultaneous and co-located measurements of the PMC environment, e.g., temperature and water vapor, help with the interpretation of CIPS data.

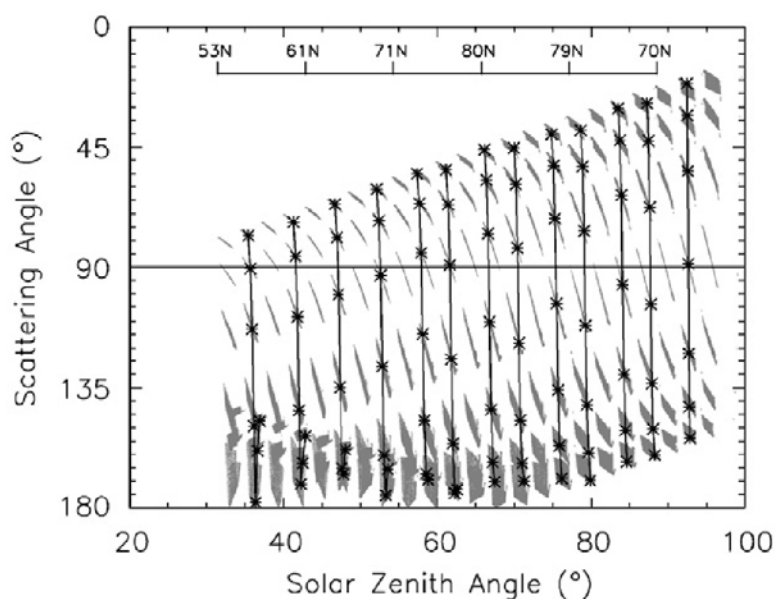


Figure 1.14: SCAs and SZAs for every CIPS observation during orbit 424 on May 24 2007 (gray dots, every fourth observation only). Seven observations for 13 individual locations are shown as asterisks connected by solid lines. From Bailey *et al.* [2009], Figure 1¹³.

¹³ Reprinted from Journal of Atmospheric and Solar-Terrestrial Physics, 71, Bailey, S. M., Thomas, G. E., Rusch, D. W., Merkel, A. W., Jeppesen, C. D., Carstens, J. N., Randall, C. E., McClintock, W. E. and Russell, III, J. M., 2009, Phase functions of polar mesospheric cloud ice as observed by the CIPS instrument on the AIM satellite, 373-380, Copyright (2008), with permission from Elsevier.

CIPS retrievals provide several data products. Level 0 data are single-camera images of the raw, uncalibrated measurements. Images are binned on-chip to 170×340 pixels (cross track by along track) for each camera. Level 1a data are single-camera images of the calibrated and geolocated albedo. In both these levels the resolution of each data pixel depends on its location and varies from $\sim 2.4 \text{ km} \times 2 \text{ km}$ (nadir) to $\sim 4.5 \text{ km} \times 3 \text{ km}$ (front & aft cameras). Level 1b data are orbit-by-orbit, multi-camera map-projected albedo values for which all measurements of a single location have been registered spatially with a resolution of 25 km^2 . At nadir the resolution element has a size of $5 \times 5 \text{ km}$. Away from nadir the resolution elements become elongated, but still always cover exactly 25 km^2 . Levels 0, 1a, and 1b data products do not contain any retrieved cloud parameters and are not publicly available. Level 2 data files contain retrievals of cloud parameters at the level 1b resolution. Four different level 2 files contain data of geolocation (e.g., latitude, longitude, UT time, SZA, etc.), cloud properties (e.g., albedo, particle radius, ice water content (IWC)), cloud phase functions, and retrieved ozone properties. Except for the experimental ozone properties, level 2 is publicly available. Figure 1.15 shows an example of a CIPS level 2 orbit strip of cloud albedo. Level 2 orbit strips are also available showing IWC and ice particle radius.

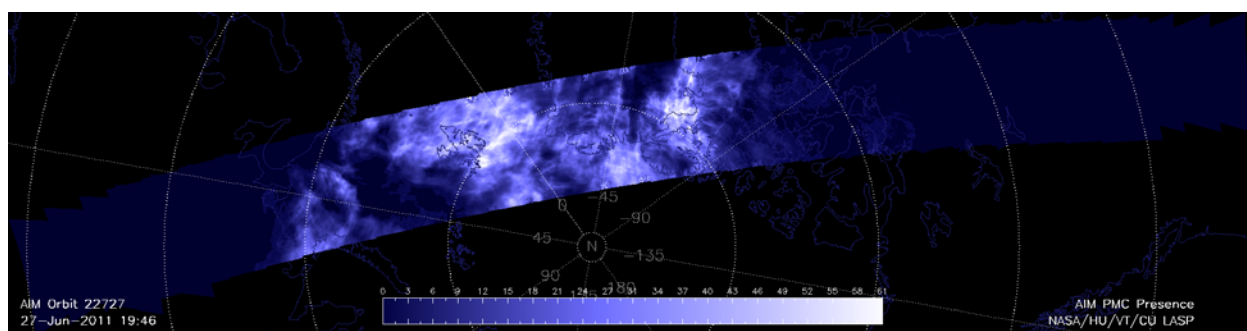


Figure 1.15: CIPS level 2 orbit strip of cloud albedo on June 27 2011, orbit 22727.

Levels 3a, 3b, and 3c contain daily cloud albedo maps, movies of daily cloud albedo maps, and season-long, latitude-binned files of level 2 data on an orbit-by-orbit basis, respectively. Figure 1.16 shows an example of a CIPS daily cloud albedo map for June 21 2011, also called a ‘daily daisy’. More details about data versions and file contents can be found on the AIM CIPS website¹⁴.

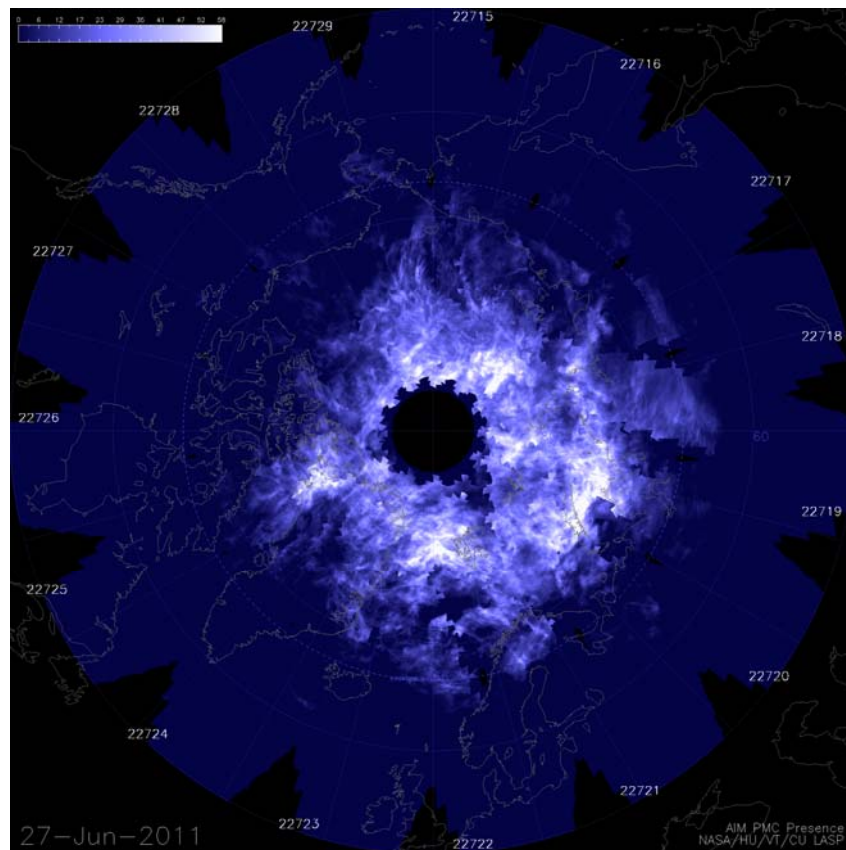


Figure 1.16: CIPS level 3a ‘daily daisy’ of cloud albedo on June 27 2011.

The calibration process that takes place during the conversion from level 0 to level 1a is necessary to correct for the temperature dependent electrical offset and dark current, non-linearity, integration period, radiometric sensitivity, gain correction, and flat field. Additionally,

¹⁴ <http://lasp.colorado.edu/aim/data-overview.html>

the cameras are normalized to each other. This calibration process is described in detail by McClintock *et al.* [2009] and can also be found on the AIM CIPS website¹⁵.

The cloud retrieval algorithm is an iterative process carried out on 0.25° SZA bins. During each of the three iterations, in each SZA bin, data points assumed to be non-cloud measurements (all points in the first iteration) are fit using the C/σ Rayleigh model [McPeters, 1980], which describes the atmospheric albedo due to Rayleigh scattering analytically. It derives the ozone column density above the Rayleigh scattering peak (C), and the ratio of ozone to atmospheric scale heights (σ). The C/σ model and its derivation and limitations as applied to CIPS are described in detail by Bailey *et al.* [2009]. The analytically derived albedo due to Rayleigh scattering for each SZA bin is removed from each measured albedo to get the cloud residual albedo. In each pixel it is then tested whether the residual cloud albedo is above a certain threshold for cloud detection. This threshold is obtained from a look-up table that was generated with pre- and post-season data for each season. For each cloud pixel the particle radius and albedo at a SCA of 90° are retrieved by fitting the measured phase function to a theoretical phase function obtained from T-matrix calculations. The T-matrix approach [Mishchenko *et al.*, 1996; Mishchenko and Travis, 1998] is a more general approach than Mie theory since it does not assume spherical particles, but instead small, randomly oriented, rotationally symmetric particles. For the theoretical phase function, a Gaussian size distribution with radii between 1 and 100 nm, width values that change as a function of radius, and an axial ratio of 2 are assumed. These assumptions are based on results from Rapp and Thomas [2006], Baumgarten *et al.* [2010], and Hervig and Gordley [2010]. The best theoretical phase function fit is obtained through Chi square minimization. For cloud pixels the Rayleigh albedo is recalculated by

¹⁵ http://lasp.colorado.edu/aim/cips/data/repository/docs/cips_calibration.pdf

subtracting the cloud albedo from the observed albedo. The next iteration starts with an updated list of cloud data points so that the calculated Rayleigh background converges towards the true Rayleigh background. Figure 1.17 shows how a sample measured phase function is composed of the sum of Rayleigh phase function and cloud phase function. After the iteration process the IWC is calculated for all cloud pixels using the retrieved particle size, albedo, and the underlying size distribution.

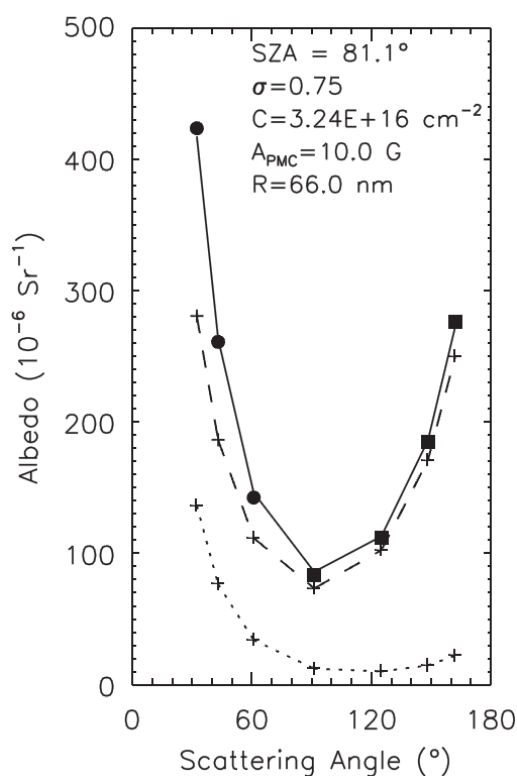


Figure 1.17: Sample phase function containing a PMC with a derived albedo of $10 \times 10^{-6} \text{ sr}^{-1}$ (10 "G") and a mean particle size of 66 nm. Points depict observed albedo: dots denote observations at SCAs less than 90° and squares are observations at SCAs greater than 90° . The dashed line is the retrieved cloud albedo, whereas the dotted line is the retrieved Rayleigh albedo. The black line is the sum of retrieved Rayleigh and cloud albedo. From Bailey *et al.* [2009], Figure 4¹⁶.

¹⁶ Reprinted from Journal of Atmospheric and Solar-Terrestrial Physics, 71, Bailey, S. M., Thomas, G. E., Rusch, D. W., Merkel, A. W., Jeppesen, C. D., Carstens, J. N., Randall, C. E., McClintock, W. E. and Russell, III, J. M., 2009, Phase functions of polar mesospheric cloud ice as observed by the CIPS instrument on the AIM satellite, 373-380, Copyright (2008), with permission from Elsevier.

1.6 SBUV

The SBUV series of instruments was briefly introduced in Section 1.4.4; this section gives a more detailed description of the instrument and an overview of the SBUV PMC detection algorithm. SBUV is a nadir-pointing spectrometer: it observes towards the ground with an $11.3^\circ \times 11.3^\circ$ field of view, which corresponds to a footprint size of $\sim 150 \times 150$ km at PMC altitude. The instrument measures the scattered radiance of the atmosphere, I_λ ($\text{W m}^{-2} \text{sr}^{-1}$), and the incoming solar irradiance, F_λ (W m^{-2}), at twelve wavelengths in the UV. The wavelength dependent albedo is calculated as $A_\lambda = I_\lambda/F_\lambda$; its unit is therefore sr^{-1} . Only the five shortest wavelengths are used for PMC observations: 252.0 nm, 273.6 nm, 283.1, 287.6 nm, and 292.3 nm. In the mid-UV the terrestrial, tropospheric, and stratospheric albedo is extremely low due to absorption of UV primarily by ozone and molecular oxygen [Brasseur and Solomon, 2005]. Only in the mesosphere and above is scattering from the gas molecules observed. For PMC measurements, this scattering is referred to as the Rayleigh background signal since the scattering is described by Rayleigh scattering theory and comes from atmospheric gases, not cloud particles. PMCs are expected to appear as spectrally dependent enhancements of the Rayleigh background, with the largest enhancement at the shortest wavelengths. Because of its nadir viewing geometry, the Rayleigh background observed by SBUV is very bright. Therefore, SBUV is able to identify only the brightest clouds. With SBUV instruments continuously operating since 1978, more than a quarter century of PMC occurrence frequency and brightness measurements are now available for long-term studies. Since the SBUV satellites were launched into different sun-synchronous orbits and therefore measure PMCs at different local times, local time or tidal studies are possible, but difficult since solar cycle and other long-term variations complicate the analyses.

In order to identify the relatively weak PMC signal in the SBUV measurements, the Rayleigh background must first be characterized. This is accomplished in an iterative process. First, a fourth-order polynomial fit to the daily wavelength-dependent albedo is calculated as a function of Solar Zenith Angle (SZA), as shown in Figure 1.18. The residual albedo is calculated by subtracting the fit from the albedo measurement at each corresponding SZA. Several tests are then applied to the residual albedo to positively identify a cloud: the PMC residual albedo must be positive and the PMC residual albedo must be higher at shorter wavelengths than at longer wavelengths. In addition, a noise threshold is applied to filter out potential stratospheric ozone fluctuations of the Rayleigh background during a day. For more details on these PMC detection tests, the reader is referred to DeLand *et al.* [2003; 2007]. During subsequent iterations, all samples that are found to be potential PMC points are excluded for the next iteration when recalculating the Rayleigh background fit. After five iterations, points that are not identified as clouds are identified as background. PMC brightness is set equal to the residual albedo of a cloud point found at 252 nm.

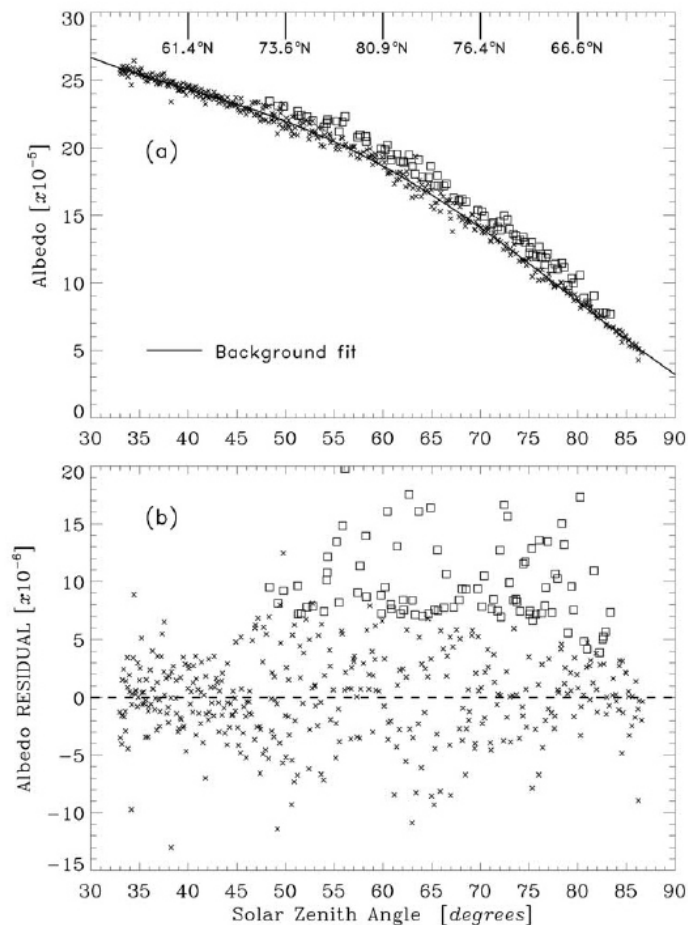


Figure 1.18: (a) NOAA-9 SBUV/2 252 nm albedo values for all measurements poleward of 50°N on June 29 1985. Squares indicate measurements identified as PMCs by the detection algorithm. The solid line is a 4th order polynomial fit to all non-PMC measurements. Heavy tick marks show approximate latitudes corresponding to reference solar zenith angle values. (b) 252 nm albedo residuals (data—fit). PMC detections are indicated by squares. DeLand *et al.* [2003], Figure 2¹⁷.

¹⁷ Reproduced with permission of American Geophysical Union. DeLand, M. T. and Shettle, E. P. and Thomas, G. E. and Olivero, J. J., Solar backscattered ultraviolet (SBUV) observations of polar mesospheric clouds (PMCs) over two solar cycles, *Journal of Geophysical Research-Atmospheres*, 108, 8445, 2003. Copyright [2003] American Geophysical Union.

2 CIPS validation

AIM was launched in April 2007 as the first mission dedicated to investigating PMCs. This chapter summarizes the CIPS validation efforts presented by Benze *et al.* [2009; 2011]. Validation is important and necessary to ensure that CIPS PMC results are valid for scientific analysis. Benze *et al.* [2009] compare CIPS level 1a PMC frequency, cloud albedo and background albedo to SBUV data in the NH 2007 season. Benze *et al.* [2011] extend this study work by updating the analysis from one to four seasons (NH 2007 to SH 2008) and adding a comparison to the CIPS operational algorithm. As shown below, the CIPS data compare favorably to well validated measurements of PMCs from SBUV.

2.1 Summary

Benze *et al.* [2009] and Benze *et al.* [2011] validate CIPS data by comparison to SBUV. CIPS and SBUV are similar in that both are downward-looking instruments measuring scattered sunlight in the UV wavelength region. SBUV is a long-term dataset that has been used to observe PMCs since 1978 [DeLand *et al.*, 2003; 2006b; 2007]. A summary of SBUV validation of ozone and PMCs is presented by Benze *et al.* [2009]. CIPS and SBUV each have their unique advantages: due to its wide-angle setup of four CCD cameras, the CIPS view angle is not restricted to nadir, which facilitates measuring the atmospheric and cloud phase function that is used for PMC detection. In addition, CIPS has a much higher spatial resolution (2 x 2 km in the level 1a data) than SBUV (150 x 150 km at the PMC altitude). SBUV on the other hand captures

the spectral behavior of the atmospheric background and PMCs at five different UV wavelengths, and utilizes the spectral dependence of ice particle scattering for PMC detections.

For validation purposes it is advantageous to match the observations and algorithms of the CIPS and SBUV instruments as closely as possible. Benze *et al.* [2009] and Benze *et al.* [2011] present the so-called ‘SBUV-type’ algorithm, which can be applied to both data sets to infer PMC frequency, cloud albedo (also referred to as cloud brightness) and the albedo of the atmospheric background, or background albedo. In order to resemble the SBUV nadir footprint, CIPS pixels in the PY camera close to nadir are averaged into the ‘PY’ footprint of 150 x 150 km. This SBUV-type algorithm does not take advantage of either the SBUV spectral information or the CIPS SCA dependence and high resolution. Therefore it is expected that this algorithm is not as good for characterizing PMCs as the operational CIPS and SBUV algorithms, respectively, but it serves the purpose of validation.

The validation studies use both zonal average and coincidence analysis to compare frequency, cloud albedo and background albedo. One difference between Benze *et al.* [2009] and Benze *et al.* [2011] is that the earlier study analyzes only the NH 2007 season, whereas the later study extends the validation to four PMC seasons between NH 2007 and SH 2008. The later study also separates observations from the ascending and descending node, finding that the SBUV-type algorithm lacks the ability to properly identify the atmospheric background albedo at the very high SZAs located on the ascending node. It therefore falsely identifies background measurements as clouds, increasing the cloud frequency to improbably high values in the ascending node. This finding leads to an exclusion of ascending node data in the CIPS/SBUV quantitative comparisons reported in Benze *et al.* [2011]. It should be noted however, that this

shortcoming is a result of the SBUV-type algorithm alone and is not necessarily present in the CIPS and SBUV operational algorithms.

The Benze *et al.* [2009, 2011] studies show that cloud frequency and albedo are in excellent agreement between CIPS and SBUV using both zonal average and coincident measurements. The later study however finds a systematic difference in background albedo that is dependent on hemisphere, with the CIPS background albedo being significantly lower than the SBUV background albedo in the NH and vice versa in the SH. This result could not have been gained from the first study investigating only one NH PMC season. The reason for this hemispheric asymmetry in the background albedo differences is speculated to be due to differences in orbit geometry, but remains unclear at the current time.

Averaging CIPS pixels in the nadir portion of the PY camera degrades the CIPS cloud detection sensitivity since the PY camera observes at mostly backscattering angles. At forward scattering angles, i.e. smaller SCAs, the cloud detection sensitivity is expected to increase since at these angles the Mie scattering phase function is most different from the Rayleigh phase function. Therefore, in order to increase cloud detection sensitivity while using the SBUV-type algorithm, CIPS pixels are averaged into a 150 x 150 km footprint at the forward edge of the PX camera, the 'PX' footprint, where observations are made with the smallest SCAs. These results should be similar to the operational CIPS results, which utilize the PMC SCA dependence to calculate the cloud phase function. Benze *et al.* [2011] compare SBUV PMC results from the SBUV-type algorithm to the CIPS nadir results (PY footprint), to the PX footprint results, and also to the operational CIPS results. It is found that the PX footprint and operational frequencies show excellent agreement at latitudes poleward of 75°. At more equatorward latitudes the CIPS operational frequencies are lower than the PX footprint SBUV-type frequencies, with one

possible reason being a decreased cloud sensitivity of the operational algorithm at more equatorward latitudes in the descending node due to poorer constraint of the cloud phase function.

The overall conclusion of Benze *et al.* [2009; 2011] is that CIPS cloud frequency and cloud albedo are valid for scientific analysis, with a still unresolved bias in the background albedo that depends on hemisphere. In addition, the CIPS v3.20 operational frequencies at more equatorward PMC latitudes on the descending node might have a small (~10%) low bias. Subsequent to the publication of Benze *et al.* [2011] the v4.20 operational CIPS retrieval version was introduced. It has a significantly improved background removal algorithm, and thus improved cloud detection statistics.

2.2 Benze *et al.* [2009]: Comparison of polar mesospheric cloud measurements from the Cloud Imaging and Particle Size experiment and the solar backscatter ultraviolet instrument in 2007¹⁸

Susanne Benze^a, Cora E. Randall^a, Matthew T. DeLand^b, Gary E. Thomas^c, David W. Rusch^c, Scott M. Bailey^d, James M. Russell III^c, William McClintock^c, Aimee W. Merkel^c, Chris Jeppesen^c

¹⁸ Reprinted from Journal of Atmospheric and Solar-Terrestrial Physics, 71, Benze, S., C. E. Randall, M. T. DeLand, G. E. Thomas, D. W. Rusch, S. M. Bailey, J. M. Russell, III, W. E. McClintock, A. W. Merkel, and C. D. Jeppesen, Comparison of polar mesospheric cloud measurements from the Cloud Imaging and Particle Size experiment and the solar backscatter ultraviolet instrument in 2007, 365-372, copyright (2008), with permission from Elsevier.

^a Laboratory for Atmospheric and Space Physics & Department of Atmospheric and Oceanic Sciences, University of Colorado at Boulder, 392 UCB, Boulder, CO 80309-0392, USA

^b Science Systems and Applications Inc. (SSAI), Greenbelt, MD, USA

^c Laboratory for Atmospheric and Space Physics, 1234 Innovation Drive, Boulder, CO 80303, USA

^d Bradley Department of Electrical and Computer Engineering, Virginia Polytechnical and State University, Blacksburg, VA 24061, USA

^e Center for Atmospheric Sciences, Hampton University, Hampton, VA, USA

Abstract

We compare measurements from the Aeronomy of Ice in the Mesosphere (AIM) Cloud Imaging and Particle Size (CIPS) experiment to the NOAA-17 solar backscatter ultraviolet (SBUV/2) instrument during the 2007 NH polar mesospheric cloud (PMC) season. Daily average Rayleigh scattering albedos determined from identical footprints from the CIPS nadir camera and SBUV/2 agree to better than ~5% throughout the season. Average PMC brightness values derived from the two instruments agree to within $\pm 10\%$. PMC occurrence frequencies are on average ~5% to nearly a factor of two higher in CIPS, depending on latitude. Agreement is best at high latitudes where clouds are brighter and more frequent. The comparisons indicate that AIM CIPS data are valid for scientific analyses. They also show that CIPS measurements can be linked to the long time series of SBUV/2 data to investigate long-term variability in PMCs.

2.2.1 Introduction

Polar mesospheric clouds (PMCs) are very thin ice clouds forming in the summer mesopause region. They are generally referred to as noctilucent clouds (NLC) when viewed or measured from the ground. It has been suggested that they are related to climate change in the upper atmosphere [Thomas, 1996a; Thomas *et al.*, 1991]. As tracers of upper atmosphere water vapor and temperature, PMCs can be used to understand the dynamics of the upper mesosphere. Thomas *et al.* [1989] first suggested that increases in mesospheric water vapor resulting from increased methane would lead to brighter PMCs. DeLand *et al.* [2003] suggested that this might lead to an earlier (later) first appearance of NLCs during evening (morning) twilight, whereas Thomas [1996b] proposed that it could cause PMCs to shift to lower latitudes, which was supported by Taylor *et al.* [2002]. AIM is the first satellite mission specifically dedicated to measuring PMCs. The mission is designed to elucidate the connections between PMCs and mesospheric water vapor, temperature, and dynamics, with an overall goal of understanding how PMCs form and why they vary [Russell *et al.*, 2009]. AIM was recently extended for another 3 years, making it a 5-year mission. This enables investigation of interannual observations, solar cycle effects, hemispheric differences, and teleconnections among other things.

The Cloud Imaging and Particle Size (CIPS) experiment is a panoramic imager with a field of view of 120° (along track) by 80° (cross-track) or about 2000 x 1000 km; it is described in more detail by Russell *et al.* [2009] and McClintock *et al.* [2009]. CIPS has an unprecedented spatial resolution of ~2 km in the nadir. In order to derive PMC morphology and cloud particle size, CIPS measures scattered sunlight with a 15 nm passband centered at 265 nm. The observed signals include Rayleigh scattering by atmospheric gases as well as scattering by the PMCs

themselves. The Rayleigh scattering signal must therefore be separated from the observed signal to infer PMCs. The method by which this is accomplished is described in Section 2.2.2. Radiation at 265 nm penetrates to an altitude of about 50 km; the atmospheric Rayleigh scattering signal is thus modulated by upper stratospheric and mesospheric ozone absorption in the Hartley–Huggins band as the radiation propagates along the incident and scattered light paths. Chandran *et al.* [2009] use ice signatures to derive information regarding gravity waves; and Merkel *et al.* [2009] analyze the clouds detected by CIPS to derive information on planetary wave activity in the mesosphere. Rusch *et al.* [2009] describe features in the CIPS cloud data that are likely caused by various dynamical phenomena.

The primary goal of this paper is to show that the AIM CIPS data are of high quality, and valid for the types of scientific analyses described above. This is accomplished by comparing CIPS measurements to concurrent measurements from the NOAA-17 solar backscatter ultraviolet (SBUV/2) instrument [e.g., Frederick *et al.*, 1986; Heath *et al.*, 1975]. The SBUV/2 instruments have a long history of PMC measurements, spanning several decades. Therefore, these comparisons also show that the CIPS measurements can be linked to the long time series of SBUV data to investigate long-term variability in PMCs. With its unprecedented high resolution, CIPS data can be used to account for possible biases in the SBUV data set that might result from its lower-resolution sampling, ensuring that long-term trends are interpreted correctly. Because of the coincident information on such atmospheric parameters as mesospheric temperature and water vapor measured by the Solar Occultation For Ice Experiment (SOFIE) [Russell *et al.*, 2009] and the Sounding of the Atmosphere using Broadband Emission Radiometry (SABER) [Russell *et al.*, 1999], we can ultimately address the question of the origin of long-term variability, one of the scientific objectives of AIM. Quantitative comparisons with global models

will be possible, validating the physical mechanism of cloud formation and the origin of long-term variability in PMC properties.

The SBUV/2 instruments are nadir-pointed, and measure backscattered radiation at 12 different wavelengths ranging from 252 to 340 nm. Unlike CIPS, the SBUV/2 instruments are not imagers; rather, the field of view consists of a single footprint of $11.3^\circ \times 11.3^\circ$, or about 150 km x 150 km at the PMC altitude. The SBUV/2 instruments were originally designed to measure ozone, but have been used to measure PMCs [Thomas *et al.*, 1991; DeLand *et al.*, 2003, 2006b, 2007]. For the comparisons shown here, the CIPS data were analyzed in the same manner as the SBUV/2 data, as described in Section 2.2.2. We use level 1a CIPS data, version 3. We restrict the comparisons here to the NOAA-17 SBUV/2 data, since the local times of measurements from this satellite more closely match the CIPS local times than measurements from other SBUV/2 instruments. The SBUV/2 data correspond to version 3. SBUV data have been validated extensively with instruments measuring profile and column ozone as well as PMCs. The integrated ozone columns measured by SBUV and the Stratospheric Aerosol and Gas Experiment between October 1984 and June 1990 agree to within $\pm 2.3\%$ at all latitudes [McPeters *et al.*, 1994]. Thomas *et al.* [1991] showed that SBUV correlates well with contemporaneous Solar Mesosphere Explorer (SME) PMC data: the seasonal and latitudinal variations of PMCs are similar, and correcting for different sensitivities of the instruments, the general magnitude of the SBUV residuals is consistent with that expected from SME data. DeLand *et al.* [2003] extended this comparison to SBUV/2 and found that NOAA-9 SBUV/2, Nimbus-7 SBUV and SME results for the 1985 and 1986 seasons were very similar in magnitude and temporal structure when different sensitivities and scattering angles were accounted for.

Using a more recent PMC detection algorithm, DeLand *et al.* [2007] showed even better agreement between various SBUV/2 instruments in both hemispheres.

2.2.2 Cloud detection algorithm

Both the SBUV/2 and CIPS instruments measure radiance backscattered by the atmosphere and clouds. The albedo (unit of sr^{-1}) is obtained by dividing the radiance by the solar irradiance. This section describes the method by which we separate the contributions to the albedo from “background” Rayleigh scattering and PMC scattering. As described by Bailey *et al.* [2009], one approach to separating Rayleigh scattering from cloud scattering takes advantage of the fact that CIPS is capable of measuring the scattering phase function. That is, CIPS takes multiple exposures of the same region of the atmosphere at different scattering angles. Since scattering by the relatively large particles in clouds is described by a different phase function than Rayleigh scattering, this principle can be utilized to separate the background Rayleigh scattering from the PMCs. This approach is not possible with the SBUV/2 instrument, since it does not measure the same region of space at multiple scattering angles. Thus, the Rayleigh background removal technique used for the CIPS/SBUV comparisons is based on a simplification of the method described by DeLand *et al.* [2003], which is applied to both the CIPS and SBUV/2 data.

In the SBUV/2 data, PMCs appear as spectrally dependent enhancements of the background (Rayleigh scattering) signal. Since the CIPS instrument does not have multi-wavelength data, the standard SBUV/2 cloud detection algorithm, which takes advantage of the spectral dependence, cannot be applied directly to the CIPS data. Therefore, the standard algorithm was modified to a single-wavelength approach, and the modified algorithm was

applied to both the SBUV/2 and CIPS data. Here we describe the standard SBUV/2 algorithm, then compare results from it to the modified algorithm.

In the standard SBUV/2 analysis, the background albedo is defined as a fourth-order polynomial fit to the observed albedo as a function of solar zenith angle (SZA), including all measurements on a given day. The fit is calculated for data acquired at each of five UV wavelengths [DeLand *et al.*, 2003]. As an example, the top left plot of Figure 2.1 shows the SBUV/2 albedo as a function of SZA at 273 nm on 20 July 2007. For a nadir instrument like SBUV/2 the SZA can be converted to the solar scattering angle (SCA): $SCA = 180^\circ - SZA$. Therefore, the background albedo decreases (increases) with increasing SZA (SCA) between 0° and 90° SZA (90° and 180° SCA), as expected for Rayleigh scattering. The difference between the albedo values and the background fit is defined as the albedo residual or, for clouds, the PMC brightness for each wavelength. The residuals for this example are shown in the bottom left plot of Figure 2.1.

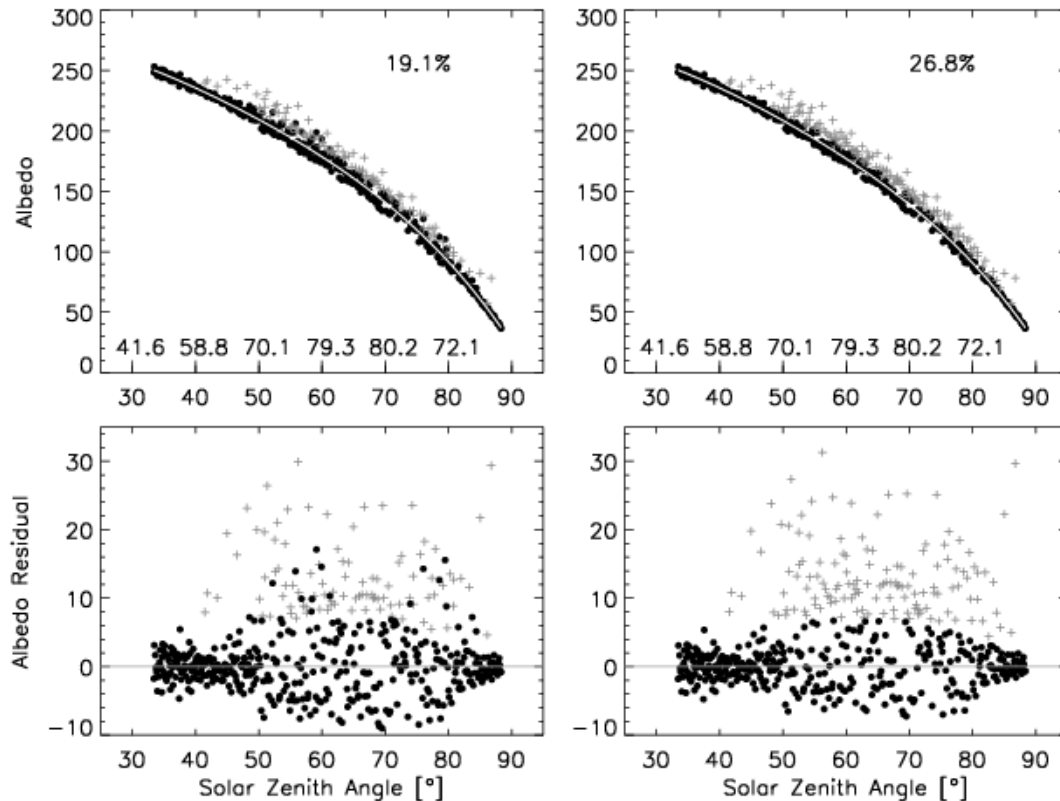


Figure 2.1: Comparison of the albedo (top) and albedo residual (bottom) derived from the standard SBUV/2 cloud detection algorithm (“all- λ ”, left) and the modified, single-wavelength algorithm (“one- λ ”, right) applied to NOAA-17 SBUV/2 data from 20 July 2007. The one- λ algorithm uses the SBUV/2 273-nm channel. Albedo and albedo residual units on all plots are 10^{-6} sr^{-1} . Black, closed circles denote non-cloud points; gray, plus symbols represent cloud detections. Labels just above the horizontal axis in the top panels denote measurement latitudes. The white line in the top panels indicates the fourth-order polynomial fit to the background

In order to identify clouds in the SBUV/2 data, the standard algorithm applies several wavelength-dependent tests to the albedo residuals, as described by DeLand *et al.* [2003] and updated by DeLand *et al.* [2007]. The first test requires that the albedo residuals at the three shortest wavelengths are positive. The second test is based on the fact that for the small particle sizes expected of PMCs, the PMC scattering will be stronger at shorter wavelengths; this imposes the requirement that the slope of a linear regression fit to the five residuals be negative. Other tests require the 252-nm albedo residual to exceed the 273-nm albedo residual and the albedo to exceed a noise threshold. The last test requires the residual to exceed the smaller of

either an absolute ($7 \times 10^{-6} \text{ sr}^{-1}$) or relative (1.05 times the average background) threshold. The last test will be referred to here as the absolute/ relative threshold test. All these tests are run five times iteratively, with successive iterations including only those points that were identified as “background”. That is, points that pass the tests on any iteration are identified as clouds, and not included in successive iterations. After five iterations, any point not already identified as a cloud is identified as background. The left panels of Figure 2.1 show SBUV/2 cloud identifications for 20 July 2007 that were based on this multi-wavelength identification procedure.

For application to CIPS data, which measures at only one wavelength, the algorithm was modified to require only that the residuals for clouds be positive and pass the absolute/relative threshold test. In the following, the original cloud detection algorithm described by DeLand *et al.* [2003; 2007] will be referred to as the "all- λ " algorithm, whereas the modified algorithm will be referred to as the "one- λ " algorithm. To estimate the error introduced by removing the spectral information from the cloud identification algorithm, the one- λ algorithm was applied to SBUV/2 data and the results compared with those obtained using the all- λ algorithm. The SBUV/2 wavelength used was 273 nm, which is the SBUV/2 channel that is closest to the center of the CIPS bandpass at 265 nm. The SBUV spectral response at 273.61 nm is quite narrow and essentially monochromatic [Fleig *et al.*, 1990]. We have performed a detailed examination of the effects of the CIPS bandpass function, convolved with the back-scattered solar radiance spectrum and the smooth spectral dependence of PMC, to find the correction needed to relate the CIPS albedo to the equivalent monochromatic albedo. We find that at 273 nm, the correction factor is fortuitously unity. So for comparison of SBUV/2 at 273 nm and CIPS at 265 nm, no correction was necessary. Further, the 273-nm channel has a signal-to-noise ratio that is ~4–5 times higher than the 252-nm channel.

Figure 2.1 illustrates the comparisons between the all- λ and one- λ algorithms with a single day of data on 20 July 2007. As noted above, the left panels display clouds identified with the all- λ algorithm; the right panels display clouds identified with the one- λ algorithm. The occurrence frequency, which is defined as the ratio of the number of cloud observations to the number of measurements per day, was 19.1% with the all- λ algorithm and 26.8% with the one- λ algorithm. The one- λ cloud detection algorithm results in a higher occurrence frequency because fewer tests are required, making it less stringent. The bottom panels of Figure 2.1 clearly differentiate between the clouds and background, showing that there is no systematic pattern with respect to SZA. Most of the clouds detected by the one- λ algorithm that are not detected by the all- λ algorithm have brightness values that are close to the background (non-cloud) level, but not all. In general, however, the one- λ algorithm gives results that are close to the all- λ algorithm. This is represented statistically in Figure 2.2, which shows the occurrence frequency vs. day of year for the one- λ and all- λ algorithms, for all SBUV/2 data over the entire NH season in 2007. The one- λ algorithm reproduces the temporal variation in cloud frequencies very well throughout the season, but with a high bias. The average frequency over the whole season is 11% for the one- λ case and 8% for the all- λ case. Note that results are similar if only the brightest clouds are included in the analysis. We conclude from this analysis that the one- λ algorithm is suitable for comparing CIPS and SBUV/2 data to evaluate the CIPS data, although frequencies might be overestimated for both instruments.

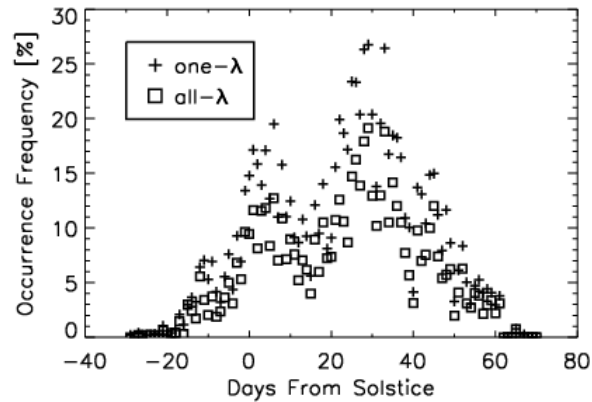


Figure 2.2: Daily occurrence frequencies (number of clouds divided by the total number of measurements on any given day, in %) from NOAA-17 SBUV/2 data calculated using the all- λ (squares) and 273-nm one- λ (plus symbols) algorithms. Measurement latitudes are restricted to 50° – 90° N.

To further ensure that the data sets are analyzed in a consistent manner, the CIPS measurements were binned into a footprint that matches the SBUV/2 footprint of ~ 150 km x 150 km at cloud altitude. Thus a single SBUV/2 measurement corresponds to the average of more than 5000 CIPS pixels. This results in an improvement in signal-to-noise ratio from 5.2 in a single-pixel measurement of the background Earth albedo [Russell *et al.*, 2009] to more than 350 for the binned data. Figure 2.3 illustrates the viewing geometries of CIPS and SBUV/2; all CIPS pixels within the SBUV/2 footprint indicated in white were binned together for the comparisons described below. Results are shown below for the CIPS PY camera (see Figure 2.3), but they are essentially identical for the MY camera.

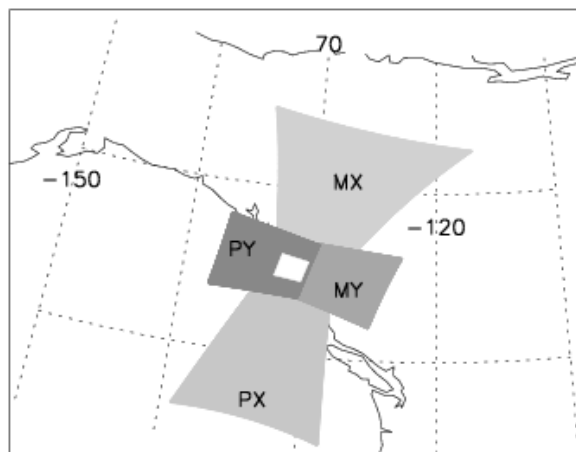


Figure 2.3: Viewing geometry for the CIPS cameras, with the SBUV/2 field of view (white) superimposed.

2.2.3 Results and discussion

An accurate retrieval of the Rayleigh background is fundamental for proper cloud detections. Figure 2.4 compares the background polynomial fits to CIPS and SBUV/2 data for 30 August 2007, a day when no clouds were detected. The top plot shows the albedo vs. SZA, with CIPS in solid gray and SBUV/2 in dashed black. The bottom plot shows the percent difference between the two instruments in the overlapping SZA ranges. For this day the CIPS background is on an average about 2% lower than the SBUV/2 background, representing one of the more favorable comparisons in the data set. Differences are largest at low solar zenith angles, which is likely explained by the fact that the measurement latitudes are significantly different at these SZA values. Figure 2.5 gives an overview of the background differences vs. day of year in 2007. The differences here are calculated as the average of the differences vs. solar zenith angle on each day (e.g., the average of the bottom curves in Figure 2.4, averaged over the entire season). CIPS is systematically lower than SBUV/2, but differences are smaller than 5%, with the exception of one day in July.

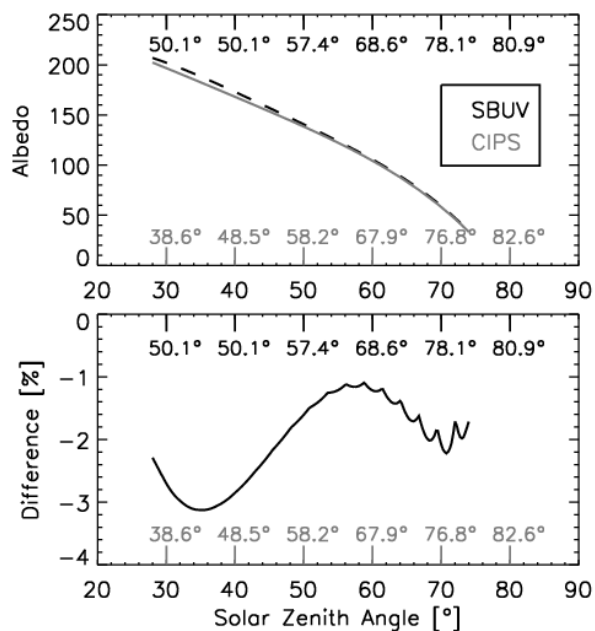


Figure 2.4: Fourth-order polynomial fits to the background albedo (top) for CIPS (gray solid) and NOAA-17 SBUV/2 (black dashed) at 273 nm and the difference between the fits (bottom) for overlapping SZA ranges on 30 August 2007. Albedo units are 10^{-6} sr^{-1} . Labels above (below) the bottom (top) horizontal axes give measurement latitudes for CIPS (SBUV).

There is an interesting time dependence in the background differences. At the beginning and end of the time period, when few or no clouds are present, the agreement is better than in the middle of the season. This could suggest that clouds lead to larger background differences, but this suggestion is contradicted by the behavior of the differences in the middle of the season. That is, temporal variations during the cloud season appear to reflect some of the same variations seen in the cloud frequencies in Figure 2.2. Peaks in frequency occur near 0 and 30 days since solstice; this corresponds approximately to decreases, not increases, in the background differences shown in Figure 2.5. One explanation for this apparent contradiction pertains to the relative brightness of the clouds that are present. Correct calculation of the background requires identification of clouds above the background variability, which is caused primarily by fluctuations in ozone densities [e.g., DeLand *et al.*, 2007] and measurement error. At the beginning and end of the season, clouds are less frequent and on average relatively dim, so even

incorrect identification does not lead to significant errors in the background calculation. In the middle of the season, however, incorrect identification of relatively dim clouds can lead to significant errors in the background because the clouds are so much more numerous. The larger or relatively brighter clouds are more easily distinguished from the background variability, and thus are not expected to lead to significant errors. As shown below (see Figure 2.9), near days 0 and 30 when the cloud frequencies increased, the average cloud brightness also increased. Thus, we speculate that the background calculations should improve near days 0 and 30 since the brighter clouds present at these times are more easily identified, and therefore do not contaminate the background calculation.

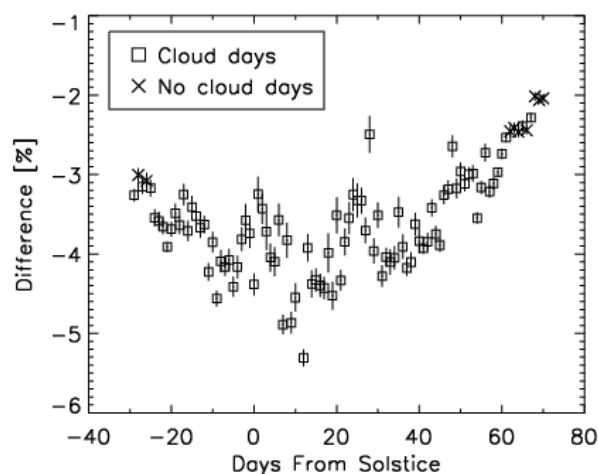


Figure 2.5: Average difference between the polynomial fits to the background for CIPS and SBUV/2 at 273 nm vs. day of year for the NH in 2007. “Error” bars represent $1\text{-}\sigma$ standard deviation of the mean difference on each day.

Figure 2.6 shows cloud detections for 22 June 2007 from both SBUV/2 (left) and CIPS (right). The top (bottom) plots show albedo (albedo residual) vs. SZA, with clouds denoted as gray plus symbols. Both the albedo and albedo residual values compare well with each other, with a minimum near $60\text{--}65^\circ$ SZA and relative maxima near 55° and 70° SZA. The CIPS occurrence frequency of 20.6% is higher than the 17.1% occurrence frequency of SBUV/2; this

is discussed more below. Interestingly, the background (non- cloud) residuals here are very similar in the SBUV/2 and CIPS data. Since the binned CIPS data have such low noise ($<0.5\%$), the variability seen here is very likely real, and caused by ozone fluctuations.

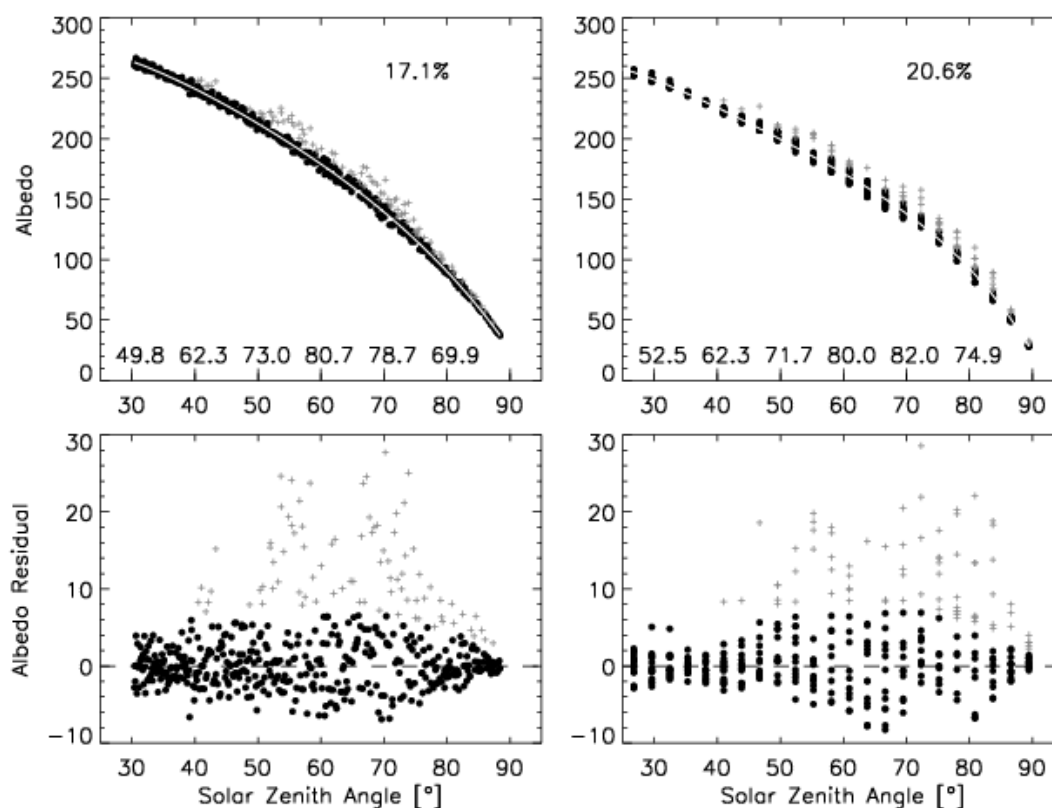


Figure 2.6: Left: Similar to the right panels in Figure 2.1, but for NOAA-17 SBUV/2 data at 273 nm on 22 June 2007; gray plus symbols denote PMCs. Right: Same as left, but for CIPS data on 22 June 2007. Albedo and albedo residual units are 10^{-6} sr^{-1} .

Figure 2.7 shows a qualitative comparison of the latitude dependence of CIPS and SBUV/2 cloud frequencies throughout the season. Both instruments show an asymmetric pattern, with cloud frequencies reaching maximum latitudinal extent near the summer solstice before gradually diminishing in extent over the next 60 days. Both instruments also show a marked decrease in frequency about 10–20 days after solstice that extends across all latitudes. These kinds of patterns have also been noted in other satellite observations of PMCs [e.g., Bailey *et al.*,

2005]. Noteworthy is that, consistent with the single-day result in Figure 2.6, the CIPS frequencies are generally higher than the SBUV/2 frequencies throughout the season and at all latitudes, as quantified next.

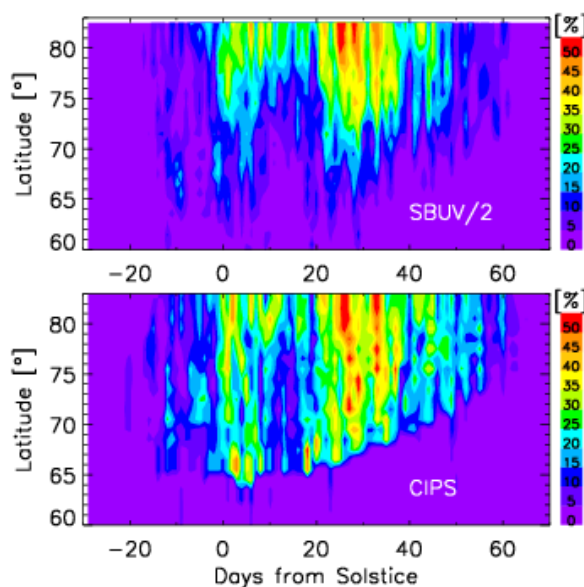


Figure 2.7: Daily PMC cloud occurrence frequency from NOAA-17 SBUV/2 data at 273 nm (top) and CIPS (bottom) in the NH in 2007. Occurrence frequencies (%) are calculated as the number of measurements identified as clouds relative to the total number of measurements in 2° latitude bins.

Figures 2.8 and 2.9 compare the occurrence frequency and PMC brightness for three different latitude ranges ($60\text{--}70^\circ\text{N}$, $70\text{--}80^\circ\text{N}$, and $80\text{--}83^\circ\text{N}$) for CIPS (red) and SBUV/2 (blue). The third latitude range extends only to 83°N because this is the highest latitude either instrument samples. Overall both the frequency and brightness of the two instruments compare very well to each other, but with some latitude dependence. The CIPS frequency is higher than the SBUV/2 frequency, as already noted, but the morphology is similar. Averaged over the season, the frequencies for CIPS (SBUV) are 8% (4%), 19% (15%), and 23% (22%) for the latitude bands from 60° to 70°N , 70° to 80°N , and 80° to 83°N , respectively. That frequencies compare better at higher latitudes might be due in part to the fact that measurement locations for the two

instruments are closer together at the high latitudes. It is probably also related to the fact that cloud brightness increases with increasing latitude, as shown in Figure 2.9. Cloud detections are more robust for the brighter clouds because they are easier to distinguish from the background [DeLand *et al.*, 2007]. The average cloud brightness values for CIPS (SBUV/2) are $6.7 \times 10^{-6} \text{ sr}^{-1}$ ($7.4 \times 10^{-6} \text{ sr}^{-1}$), $10.3 \times 10^{-6} \text{ sr}^{-1}$ ($10.0 \times 10^{-6} \text{ sr}^{-1}$), and $12.2 \times 10^{-6} \text{ sr}^{-1}$ ($11.2 \times 10^{-6} \text{ sr}^{-1}$) for the respective latitude bands. Thus on average the brightness values derived from CIPS and SBUV/2 agree to within 10%. We speculate that the higher CIPS frequencies at the lower latitudes arise because low-intensity clouds are more likely to be detected as noise on the background in the SBUV data, but actual clouds in the CIPS data. This is also consistent with the background comparisons shown in Figure 2.5. If low-intensity clouds are identified incorrectly as background in the SBUV/2 data, they will raise the background level, resulting in a background in CIPS that is lower than in SBUV/2.

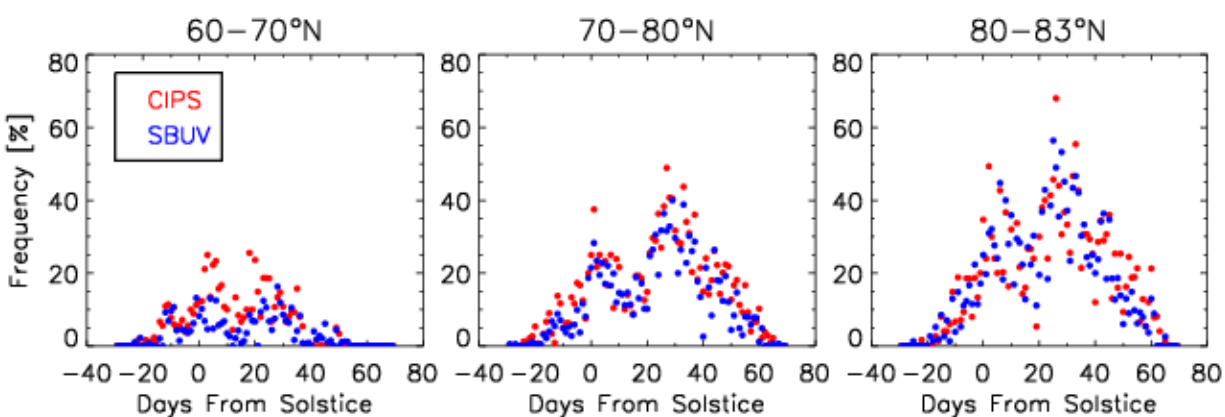


Figure 2.8: CIPS (red) and SBUV/2 (blue) PMC occurrence frequency vs. day of year for three different latitude ranges. Here the occurrence frequencies (in %) are calculated as the number of measurements identified as clouds relative to the total number of measurements in the latitude bins specified at the top of each panel.

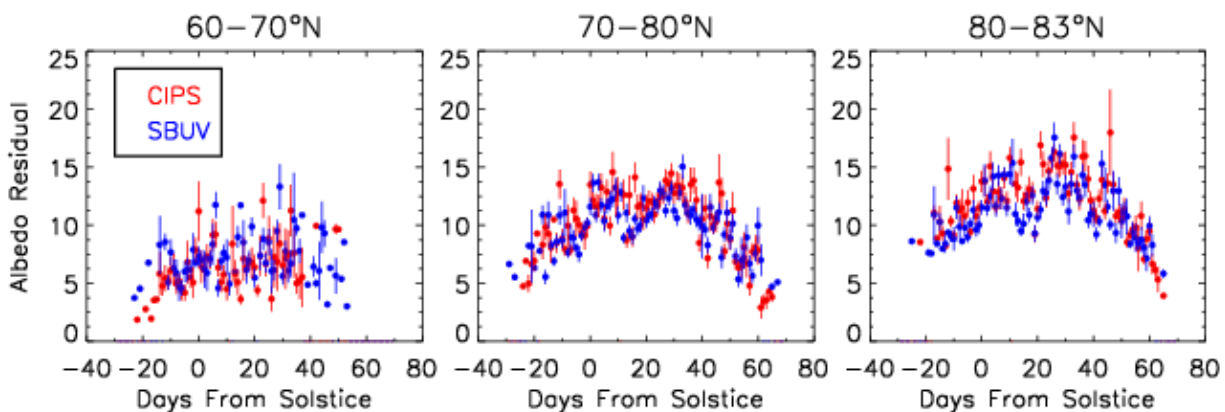


Figure 2.9: Same as Figure 2.8, but for daily average albedo residuals pertaining to cloud detections in the specified latitude bins (observed albedo minus the polynomial fit to the background, so this represents the cloud brightness). The albedo residuals have units of 10^{-6} sr^{-1} . “Error” bars represent $1\text{-}\sigma$ standard deviation of the mean PMC albedo residual on each day.

The results shown above include all of the available measurements from the two instruments, regardless of location and local time. To examine the possibility that these results were biased because of different measurement sampling, comparisons were repeated using only those measurements from both instruments that were within 100 km and 1 h in local time. Although geophysical variations can take place on these scales, this was considered a reasonable trade-off between minimizing differences in the observed atmospheric region and obtaining significant statistics. Figure 2.10 shows the SBUV/2 and CIPS nadir locations on 27 June 2007 (symbols do not correspond to actual footprint size). The framed symbols depict the coincidences. All symbols are color coded for their local time. The top plot shows the measurement locations for the whole latitude range of the measurements for that day ($40\text{--}90^\circ$), whereas the bottom plot is restricted $75\text{--}90^\circ$ in order to better display the coincidences. Over the entire season there were 1372 coincidences between CIPS and SBUV/2, or about 16 coincidences per day (ranging from 9 to 23). Most coincidences were between 78° and 82°N because local time changes rapidly as the satellites cross the polar cap and go from the day side into the night side of the Earth. Note that the number of coincidences is limited by the nadir-

viewing constraint we have placed on the current analysis; many more coincidences will be available for future comparisons using all CIPS viewing angles.

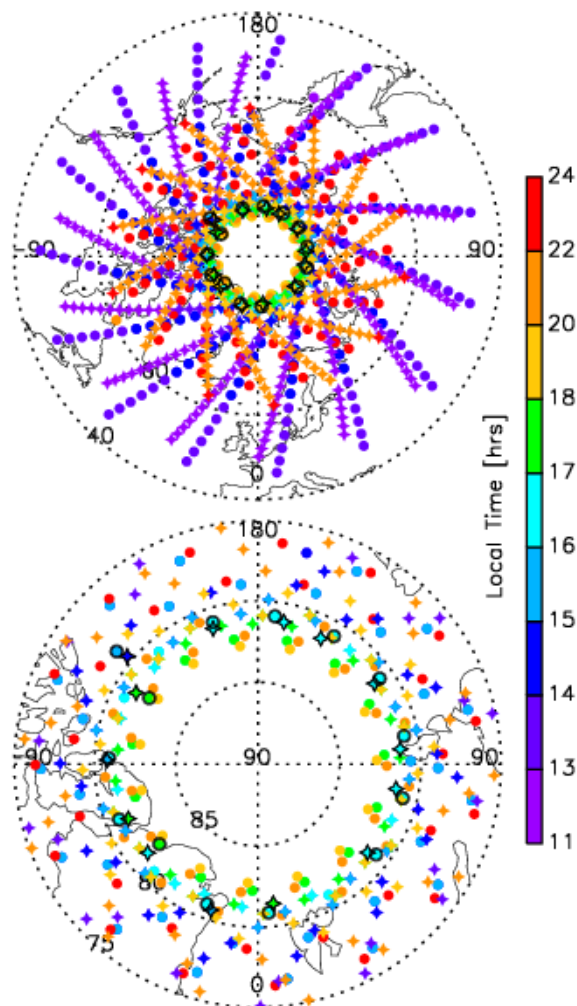


Figure 2.10: Coincidences (framed symbols) overlaid on all measurements from CIPS (circles) and NOAA-17 SBUV/2 (stars) on 27 June 2007, for all latitudes (top) and only high latitudes (bottom). Symbols are color coded by their local time.

Figure 2.11 shows the results of the coincidence comparisons. The full cloud detection analysis was not repeated because the lack of data compromises the background simulation. Rather, for Figure 2.11 the daily average quantities were simply re-calculated using only the coincident data points, but utilizing the background albedo derived with the full data set. To the extent that different measurement sampling affects the background determination, these results

are similar to the non-coincident results shown above; they should, however, be less affected by PMC variability. Figure 2.11 shows the comparisons for daily average albedo (cloud + background), frequency, and daily average albedo residual (albedo minus background) for all coincident measurements. As expected from the comparisons discussed above, all three panels show excellent agreement. The average albedo over the season was $149 \times 10^{-6} \text{ sr}^{-1}$ ($154 \times 10^{-6} \text{ sr}^{-1}$) for CIPS (SBUV/2), a difference of only 3%. The average daily cloud frequency over the season was 24% (27%), and the average cloud brightness over the season was 13% (12%) for CIPS (SBUV/2). These results are similar to the results of the non-coincidence analysis, suggesting that sampling issues are not a significant factor in the comparisons.

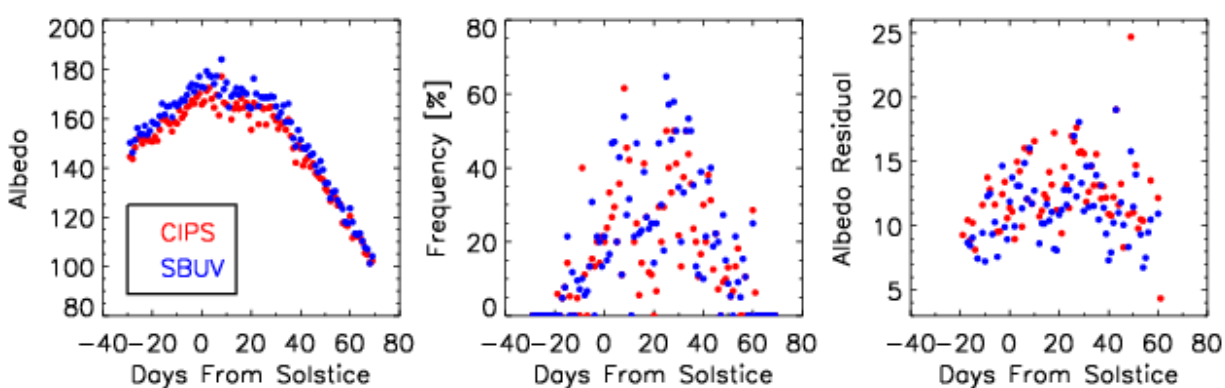


Figure 2.11: Daily average albedo (left, 10^{-6} sr^{-1}), daily occurrence frequency (middle), and daily average PMC brightness (right, 10^{-6} sr^{-1}), for the NH 2007 season from CIPS (red) and NOAA-17 SBUV/2 at 273 nm (blue). Albedos are calculated as the average of the albedos at coincident measurement locations on each day. Albedo residuals are calculated similarly; the background subtracted from the albedo to yield the residual was determined from the full set of measurements, not just coincidences. Occurrence frequencies (%) refer to the number of coincident measurements identified as clouds relative to the total number of coincident measurements on each day.

2.2.4 Conclusions

We have described comparisons between AIM CIPS and SBUV/2 Rayleigh scattering and PMC scattering measurements. A single cloud detection algorithm was applied to data from both instruments, and the high spatial resolution CIPS data were binned to match the SBUV/2 footprint. The CIPS data were thus restricted to the nadir, while SBUV/2 data were restricted to the 273-nm channel. The cloud detection algorithm was based on the standard SBUV/2 cloud detection algorithm, but ignored all spectral information.

The comparisons show that CIPS and SBUV/2 measurements are in excellent agreement. The daily average Rayleigh scattering backgrounds determined from the two instruments agree to better than ~5% throughout the season. Average CIPS PMC brightness values are within 10% of the SBUV values. CIPS daily PMC occurrence frequencies are generally higher than those from SBUV/2, with differences decreasing at high latitudes where the clouds are brighter and more frequent. From 60° to 70°N the average frequencies differed by a factor of two, but this decreased to less than 5% from 80° to 83°N. We tentatively attribute the frequency differences to the fact that binning the CIPS data into the SBUV footprint significantly improves the signal-to-noise, making it more likely that dim clouds are properly identified as such in the CIPS data. We note, however, that the single-wavelength algorithm applied here does not take advantage of the full capabilities of the SBUV/2 data, since it ignores spectral information.

We conclude from the above comparisons that the CIPS nadir data are valid for scientific analysis. It should be noted that only a tiny fraction of the available CIPS data has actually been used. Nadir data within the SBUV/2 footprints from the PY camera represent less than 0.001% of the CIPS data. In the analysis presented above, the high spatial resolution of the CIPS data as well as the scattering angle dependence has been lost. Extended algorithms are necessary to take

advantage of these unique CIPS features, such as described by Bailey *et al.* [2009]. Data produced with this type of extended algorithm was used in the analyses of Chandran *et al.* [2009], Rusch *et al.* [2009] and Merkel *et al.* [2009]. Although the current paper does not provide direct validation of the data used in those papers, the above results do indicate that the cameras are performing as expected. Further, the results in the nadir pixels analyzed here are consistent with the broader results described in those papers. An example is shown here in Figure 2.12. This figure portrays the average NH PMC occurrence frequency as a function of day and longitude during the 2007 season, for latitudes from 75° to 85°N. SBUV/2 results are shown in the top panel; CIPS results (bottom) include only the data binned into the SBUV/2 footprint. Not only do the results agree with each other, as expected from the comparisons shown above, but they also agree with the more comprehensive analysis described by Merkel *et al.* [2009]. That paper uses all of the CIPS data to explore the occurrence of planetary wave activity in the CIPS data, which is seen clearly in both the nadir CIPS and SBUV/2 data here. The comparisons shown here thus serve not only to validate the nadir CIPS data, but also to lend credibility to the off-nadir measurements as well. Finally, that CIPS data binned to match the SBUV/2 spatial resolution compare so well to SBUV/2 data supports the goal of linking the long time series of SBUV/2 data to the CIPS data in order to investigate long-term variability in PMCs.

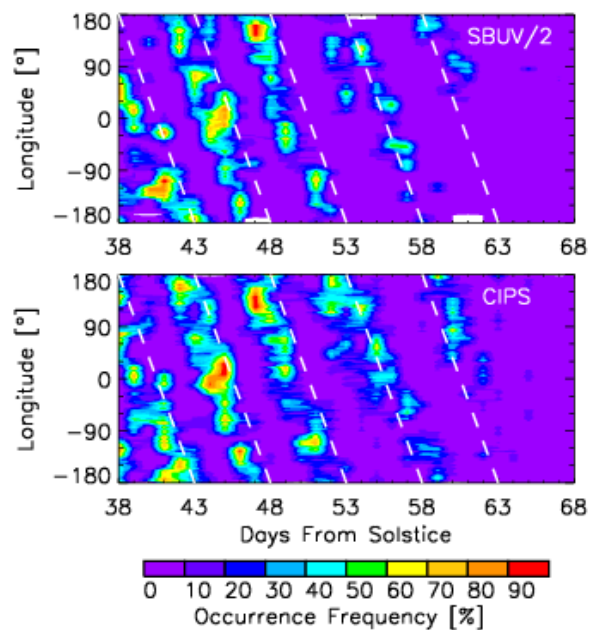


Figure 2.12: Daily occurrence frequency from 75° to 85° N plotted vs. longitude for SBUV/2 at 273 nm (top) and CIPS (bottom) in the NH in 2007. Frequencies represent a running average over 20° in longitude. White, dashed lines are drawn only for guidance; they indicate the tilt that would be expected for a 5-day wave. See Merkel *et al.* [2008] for discussion of wave activity inferred from CIPS data.

Acknowledgments

Funding for CIPS data evaluation, and for the AIM mission, was provided by the NASA Small Explorer program. The SBUV/2 data were obtained from NOAA/NESDIS with support from the NOAA Climate and Global Change Atmospheric Chemistry Element. Some of this work was supported by Grant NNX06AC96G from NASA's Office of Space Science.

2.3 Benze *et al.* [2011]: Evaluation of AIM CIPS measurements of Polar Mesospheric Clouds by comparison with SBUV data¹⁹

Susanne Benze^a, Cora E. Randall^a, Matthew T. DeLand^b, Gary E. Thomas^c, Scott M. Bailey^d, James M. Russell III^e, Aimee W. Merkel^c

^aLaboratory for Atmospheric and Space Physics and Department of Atmospheric and Oceanic Sciences, University of Colorado at Boulder, 392 UCB, Boulder, CO 80309-0392, USA

^bScience Systems and Applications Inc.(SSAI), Greenbelt, MD, USA

^cLaboratory for Atmospheric and Space Physics, 1234 Innovation Drive, Boulder, CO 80303, USA

^dBradley Department of Electrical and Computer Engineering, Virginia Polytechnical and State University, Blacksburg, VA 24061, USA

^eCenter for Atmospheric Sciences, Hampton University, Hampton, VA, USA

Abstract

Polar Mesospheric Cloud (PMC) observations from the Aeronomy of Ice in the Mesosphere (AIM) Cloud Imaging and Particle Size (CIPS) experiment are compared to results from the Solar Backscatter UltraViolet (SBUV/2) instrument for two PMC seasons in each

¹⁹ Reprinted from *Journal of Atmospheric and Solar-Terrestrial Physics*, 73, Benze, S., C. E. Randall, M. T. DeLand, G. E. Thomas, S. M. Bailey, J. M. Russell III, and A. W. Merkel, Evaluation of AIM CIPS measurements of Polar Mesospheric Clouds by comparison with SBUV data, 2065-2072, copyright (2011), with permission from Elsevier.

hemisphere, from 2007–2009. For these comparisons, a CIPS cloud retrieval algorithm based on a technique similar to that used in the operational SBUV PMC retrievals was developed. CIPS nadir data analyzed this way agree with SBUV data to better than 1% (2%) for PMC occurrence frequency (albedo). Non-nadir, forward scattering CIPS data are also analyzed with the SBUV-type algorithm, enabling an indirect verification of the CIPS operational retrievals. CIPS operational PMC frequencies agree with these CIPS–SBUV-type retrievals to within 0.6% at 80–85° latitude, and are lower by 9.8% at 70–75° latitude. Overall, the comparisons show that the v3.20 CIPS operational cloud retrievals are valid for scientific research.

2.3.1 Introduction

Polar Mesospheric Clouds (PMCs) are faint clouds in the summer polar mesopause region. They were first observed from the ground more than a century ago on June 8th, June 23rd, and July 6th 1885 by Backhouse [1885], Jesse [1890], and Leslie [1885], respectively. There is no knowledge of previous observations, which might indicate that PMCs did not exist prior to the end of the 19th century. An increase in PMC frequency and cloud albedo has been observed over the last three decades [DeLand *et al.*, 2007; Shettle *et al.*, 2009]. Several factors could possibly lead to an increase in PMCs: lower temperatures, higher water vapor concentrations, and/or higher concentrations of condensation nuclei. It has been suggested that anthropogenic forcing may lead to more/brighter PMCs since it would cause a cooling of the upper mesosphere by radiative cooling of CO₂ and an increase of water vapor due to increasing methane [Thomas *et al.*, 1989; Thomas 1996a; 1996b; 2003]. It has also been postulated that the increase in space traffic with resulting water vapor injections (e.g., from the main engine of the NASA Shuttle) could have contributed to the upward trend in PMCs [Stevens *et al.*, 2005b]. The available

measurements have neither revealed a statistically significant trend in mesospheric temperature [Lübken, 2000; Semenov *et al.*, 2002] nor water vapor. Von Zahn *et al.* [2004] showed a small water vapor increase of 0.05 ± 0.01 ppmv/year in the polar mesosphere for the period from 1996 to 2000; however, Hartogh *et al.* [2010] showed a decrease in summer water vapor mixing ratios from 1996 to 2006 over the altitude range 50–80 km at the same location as von Zahn *et al.* [2004]. Since measurements of temperature or water vapor in this remote part of the atmosphere are difficult, PMCs might serve as useful indicators for changes in the summer polar mesopause region. However, it is necessary to know the relationship between the clouds, temperature and water vapor. Knowing, for example, whether and to what degree temperature and/or water vapor influence the start, duration, and variability of the PMC season will ultimately help to determine why and due to which factors these clouds have been changing in the past.

The Aeronomy of Ice in the Mesosphere (AIM) mission was launched in 2007 to investigate how and why PMCs form and vary [Russell *et al.*, 2009]. The main goal of this paper is to evaluate PMC data from the AIM Cloud Imaging and Particle Size (CIPS) instrument [McClintock *et al.*, 2009], extending the study of Benze *et al.* [2009] from one season to four. This is accomplished by applying the “SBUV-type” algorithm described in Benze *et al.* [2009] to the CIPS version 3.20 level 1A data for the NH PMC seasons of 2007 and 2008 and the SH PMC seasons of 2007–2008 and 2008–2009. The results are compared with data from a Solar Backscatter Ultraviolet (SBUV/2) instrument [DeLand *et al.*, 2003; 2006b]. For brevity, hereinafter we will refer to the SH 2007–2008 (2008–2009) season as the SH 2007 (2008) season; we will also refer to SBUV/2 as SBUV. Details of the comparisons between CIPS nadir data and SBUV can be found in Section 2.3.2. In Section 2.3.3 we explain the extension of the SBUV-type algorithm from nadir to non-nadir data in order to take advantage of more favorable

scattering angles (SCAs) that can be found at the front edge of the CIPS scene, specifically at the front edge of the “PX” camera. Measurements at smaller scattering angles are more sensitive to PMC scattering, so cloud detections include clouds with lower directional albedo.

CIPS consists of four CCD cameras that image the Earth’s atmosphere with view angles ranging from nadir to 120°. The along-track (X) cameras are labeled PX and MX (“plus” and “minus”), while the cross-track (Y) cameras are labeled PY and MY. CIPS measures the atmospheric radiance scattered to the instrument by the atmosphere and the clouds. In the UV, specifically at the wavelengths that are used for CIPS measurements (265 ± 7 nm), any radiation from below ~ 55 km is absorbed by ozone in the atmosphere. Therefore, the measured signal is modulated by upper stratospheric and mesospheric ozone absorption in the Hartley–Huggins band as the radiation propagates along the incident and scattered light paths. The scattered signal has contributions from both molecular (Rayleigh) and cloud particle scattering that need to be distinguished by any cloud detection algorithm [Bailey *et al.*, 2009]. The CIPS cameras have a resolution of ~ 2 km in the nadir, increasing to ~ 5 km at the forward and backward edge of the CIPS scene. One scene, which is defined as a simultaneous set of images taken by all four cameras, has a field of view of about 2000 km along-track by 1000 km cross-track, when projected to the PMC altitude.

The SBUV instruments are similar to CIPS in that they also are downward-looking instruments measuring in the UV. However, unlike CIPS, the SBUV view angle is restricted to the nadir. On the other hand, whereas CIPS only measures at a single-wavelength, SBUV measures at 12 wavelengths ranging from 252 to 340 nm, from which the five shortest wavelengths between 252.0 and 292.3 nm are used to derive PMC frequency and cloud albedo [DeLand *et al.*, 2003; 2006b]. The fact that PMCs measured by SBUV appear as spectrally

dependent enhancements of the background is utilized by the SBUV cloud detection algorithm. The SBUV instruments are not imagers – their field of view consists of a single footprint with a size of 150 km x 150 km at PMC altitude. The SBUV instruments were originally designed to measure ozone, but have been used to measure PMCs since 1978 [DeLand *et al.*, 2003]. SBUV has been validated successfully by comparing ozone and PMC measurements to instruments like the Solar Mesosphere Explorer (SME) and the Stratospheric Aerosol and Gas Experiment. Additionally, the SBUV instruments have been intercompared with each other with good results [Deland *et al.*, 2003]. A summary of these validations is given in Benze *et al.* [2009].

In this paper, two algorithms for deriving cloud information are applied to CIPS data: the “operational algorithm” [Bailey *et al.*, 2009] and the “SBUV-type algorithm” [Benze *et al.*, 2009]. The operational data analyzed here, which include the cloud presence and albedo, are version 3.20 level 4 (L4) data products. The SBUV-type algorithm is applied to the v3.20 level 1 data products. The operational CIPS algorithm takes advantage of measuring one geographic location at several different SCAs. The measured phase function is used to distinguish between cloud and background, and to infer cloud albedo, particle radii, and IWC. In the SBUV-type algorithm, the background albedo is found by fitting a fourth-order polynomial to the observed albedo as a function of solar zenith angle (SZA), including all measurements on a given day. Measurements on a given day usually comprise latitudes between 30° and 83°, so they always include non-cloud points needed for fitting the Rayleigh background. The albedo residual is defined as the difference between the albedo and background fit. A threshold test is applied to this albedo residual: if the albedo residual exceeds the smaller of either an absolute threshold ($7 \times 10^{-6} \text{ sr}^{-1}$) or a relative threshold (5% above the background fit) then this measurement is defined as a cloud. This procedure is then iterated, omitting all cloud detections: only measurements

defined as background are taken into account for calculating the fourth-order polynomial fit on successive iterations. In this iterative process the background fit slowly converges to the actual Rayleigh background. Iterations are ended when no more measurements fit the cloud detection criteria. In order to compare CIPS–SBUV-type retrievals and SBUV measurements taken at different SCAs, the inferred background and cloud albedos are normalized to $SCA = 90^\circ$. For the background, this normalization assumes a Rayleigh scattering phase function of

$$P_R = \frac{3}{2\pi \cdot (2 + \Delta)} (1 + \Delta + (1 - \Delta)[\cos(SCA)]^2)$$

with $\Delta = 0.035$ being the depolarization factor. For PMCs, the normalization assumes a Mie phase function corresponding to a unimodal Gaussian size distribution with a mode particle radius (r_m) of 55 nm and a distribution width (σ) of 14 nm. The choice of these parameters is discussed in more detail in Section 2.3.3; a size distribution assumption is required here because, unlike the CIPS operational retrieval, size information is not retrieved when the SBUV-type algorithm is applied to the CIPS data.

For comparisons with SBUV, the CIPS level 1 data was analyzed with the SBUV-type algorithm in such a way that it resembles the SBUV footprint. That is, CIPS pixels were averaged into the SBUV-size 150 km x 150 km footprint. For comparisons with the CIPS L4 operational retrieval product, which has a resolution of 15 km x 15 km, the SBUV-type algorithm was applied to the CIPS level 1 data binned into a footprint size of 15 km x 15 km. This was done for two positions on the CIPS scene, as shown in Figure 2.13: on the PY camera as close to nadir as possible (PY analysis), and on the PX camera at the middle of the front edge (PX analysis). The PY analysis is used for comparison to SBUV results, since the SBUV geometry is nadir-viewing. The PX analysis results include clouds with lower directional albedo,

since the PX measurements have the smallest scattering angles and thus are most sensitive to cloud detection; these results are compared to the CIPS operational retrievals, which incorporate data acquired at all scattering angles. Since CIPS measures at just one wavelength, the SBUV algorithm was modified to a single-wavelength approach, and the modified algorithm was applied to data from both instruments. Benze *et al.* [2009] showed that when SBUV data were analyzed with the single-wavelength algorithm, seasonal average cloud frequencies were within 3% of those calculated with the multi-wavelength algorithm. We use a SBUV wavelength of 273 nm; no correction for the wavelength difference is necessary [Benze *et al.*, 2009]. From three possible SBUV instruments operating concurrently with CIPS, NOAA-17 was chosen since its local time was the closest to the CIPS local time (see Figure 2.14); SBUV NOAA-17 data correspond to version 3.

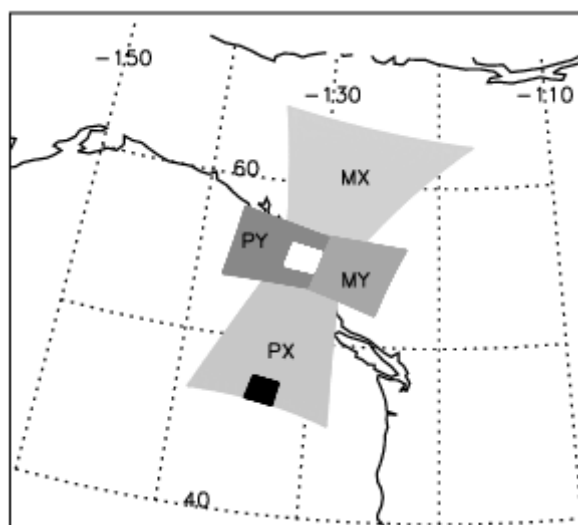


Figure 2.13: CIPS scene showing all four cameras in different shades of gray, and the 150 x 150 km SBUV-size footprints in white on the PY camera and black on the PX camera.

2.3.2 CIPS evaluation

In this section we compare cloud frequency and cloud albedo data from the CIPS nadir (PY) camera and SBUV instrument. CIPS actually has two nadir cameras; results from the nadir “MY” camera are similar, so we only present PY results here. Comparisons are presented both for zonal average measurements and for temporally and spatially coincident measurements. For zonal average comparisons, the only restrictions are that measurements from the two instruments must be taken on the same day and in the same 1° latitude bin. For coincidence comparisons, measurements from the two instruments are required to be within 100 km of each other and 2 h in local time. Zonal average comparisons are performed because they maximize the number of observations included in the statistics (~40 (80) points per day and 5° latitude bin for CIPS (SBUV)). The number of observations is lower in the coincidence analysis (~14 points per day) than in the zonal average analysis, but differences due to geophysical variations are minimized.

As noted above, we have used measurements from the NOAA-17 SBUV instrument because its measurements are closest in local time to CIPS. Figure 2.14 shows the zonal average local times of the CIPS and SBUV instruments for the NH 2007 and SH 2007 seasons; other seasons are similar. These plots have a 1 day and 2.5° latitude grid and use 3 day and 7.5°-latitude-weighted running averages, as do all other time-latitude contour plots in this paper. There are large regions of missing data in the ascending node plots because the satellites are viewing the night side of the orbit at these latitudes/times. On many days toward the end of the SH 2007 season, CIPS ascending node data is excluded because the satellite rolls in order to accommodate “common volume” (CV) measurements at high SZAs; CV measurements allow CIPS and the AIM Solar Occultation For Ice Experiment (SOFIE) to measure the same geographic location within minutes of one another [Russell *et al.*, 2009]. Such rolls cause a

change in view angle, the angle between the satellite line of sight and nadir. Measurements at different view angles have different bidirectional albedos [Bailey *et al.*, 2009], so a single polynomial will not adequately describe the background data if both rolled and non-rolled data are included. Only three or four (rolled) images are excluded per orbit (out of a total of 24–27 images per orbit), all on the ascending node. This explains the sudden change in latitudinal coverage in the SH 2007 ascending node data +5 Days From Solstice (DFS); similar effects occur in the SH 2008 and NH 2008 and 2009 seasons. At the end of the SH 2007 season, the AIM satellite went through a safhold event that shut down the satellite temporarily for safety reasons. At that time, no measurements were taken, which explains the apparent sudden end of the SH 2007 season. For the SBUV-type footprint in the CIPS PY camera, ascending node local times vary from 18 to 23 h (0–6 h) in the NH (SH); descending node local times vary from 12 to 17 h (7–11 h). Ascending node SBUV local times vary from 17 to 21 h (23 previous day to 3 h) in the NH (SH); descending node local times for SBUV vary from 12 to 15 h (4–10 h). At the highest latitudes, when the satellite crosses the pole, local times change rapidly. The largest range over which local time varies in any 2.5° latitude bin at the high latitudes is 2.4 h. Differences in the lowest observed latitudes between ascending and descending node data are determined by the position of the terminator, which is located on the ascending node.

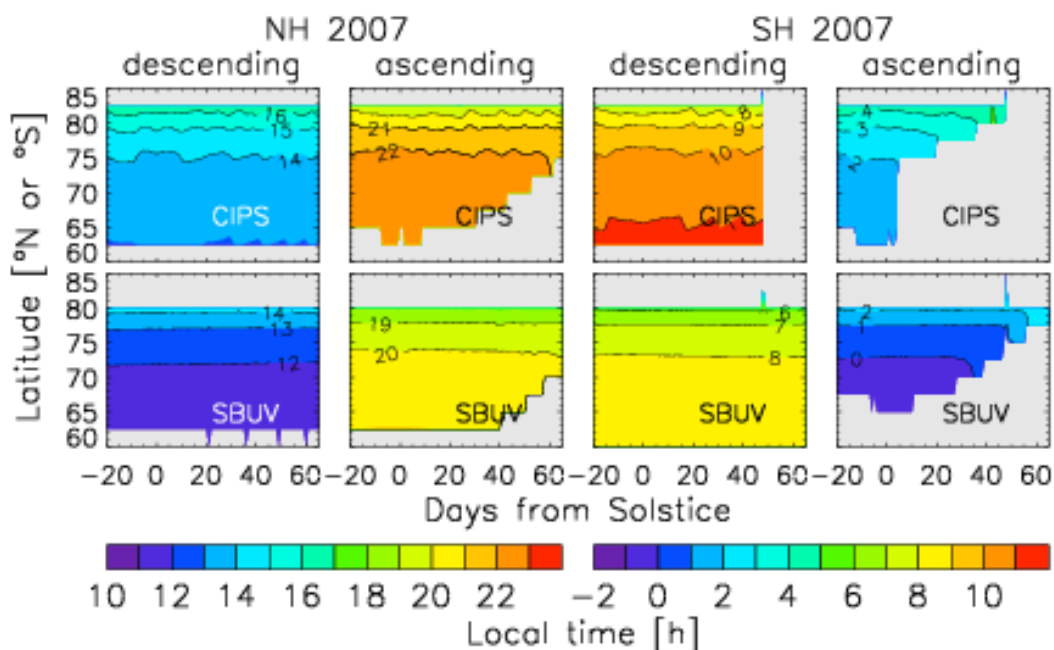


Figure 2.14: CIPS PY and SBUV NOAA-17 local time vs. DFS and latitude for the NH 2007 and SH 2007 seasons, both ascending and descending nodes. Gray areas represent no data.

2.3.2.1 Zonal average analysis

The two top rows of Figure 2.15 show CIPS and SBUV time-latitude contour plots of occurrence frequency for all seasons and for descending node only. Gray areas represent times/latitudes where no measurements were taken. For these plots and all subsequent plots of SBUV data, the SBUV results pertain to the single-wavelength algorithm described above. Qualitatively, there are many similarities between the cloud observations from the two instruments. The time periods over which clouds are detected are similar, frequencies are generally below about 60%, and intra-seasonal variations such as the mid-season PMC frequency decreases in the NH in 2007 and 2008 are captured by both instruments. Both instruments also show lower frequencies in the SH compared to the NH, as expected [Thomas *et al.*, 1991].

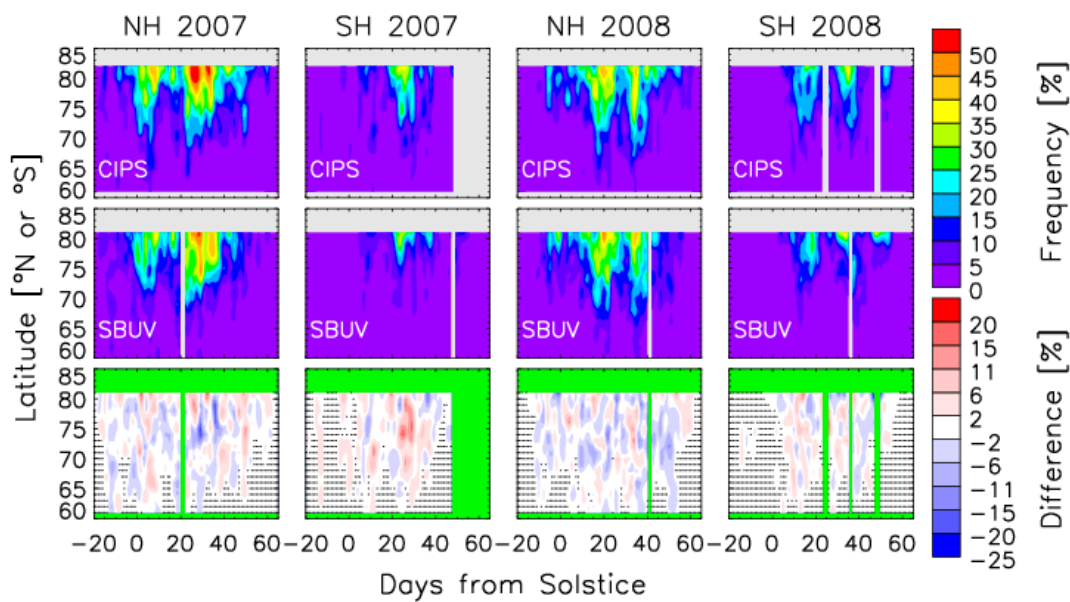


Figure 2.15: CIPS PY (top) and SBUV NOAA-17 (middle) occurrence frequency vs. DFS and latitude. From left to right: NH 2007 to SH 2008, descending node data only. Gray areas represent no data. Bottom panels: Descending node occurrence frequency difference (CIPS-SBUV). Green areas represent no data. Black dots (forming horizontal lines on the 1-degree latitude grid) show the locations of zero CIPS and SBUV frequency.

The bottom panels of Figure 2.15 show the difference (CIPS-SBUV) in occurrence frequency. Green areas represent times/latitudes where no measurements were taken. Black dots (forming horizontal lines on the 1° latitude grid) represent points where both CIPS and SBUV frequency is zero – these points were not included in the calculation of average values of frequency or differences. At most locations and times, the CIPS and SBUV cloud detection frequencies are in good agreement, with no systematic time or latitude dependence. There are a few exceptions, most notably DFS 29 and 36 in the NH 2007 season and DFS 24 and 29 in the SH 2007 season. Close inspection of these days shows robust measurements in both instruments, with no indication of any anomalous data. We thus believe that these differences are most likely due to real geophysical differences in the volume of space sampled by the two instruments. The average differences between the daily frequencies from CIPS and SBUV are listed in Table 2. Also listed is the 1- σ uncertainty in the mean difference (σ/\sqrt{n}), where σ is the standard

deviation of the differences, and n is the number of comparisons. Averaged over all seasons and latitudes, as shown in the last column of Table 2, the CIPS frequency is $0.2 \pm 0.1\%$ higher than the SBUV frequency.

Table 2: Differences in the daily frequencies (CIPS – SBUV) averaged over all latitudes ($60 - 85^\circ$) during each season $\pm 1-\sigma$ uncertainties in the mean differences. The last column gives the average over the four seasons NH07 to SH08.

	NH07	SH07	NH08	SH08	All seasons
CIPS - SBUV	$0.0 \pm 0.2\%$	$1.9 \pm 0.3\%$	$-1.0 \pm 0.2\%$	$1.0 \pm 0.3\%$	$0.2 \pm 0.1\%$

Unlike CIPS occurrence frequency from the descending node, CIPS occurrence frequency from the ascending node tends to increase at the lowest latitudes near the terminator. While it is possible that this is of geophysical origin, we have reason to question the results. The observed albedo varies steeply with SZA at the lower latitudes on the ascending node, where the SZA approaches 90° . In these cases, the fourth-order polynomial fit generally overestimates the curvature in the background, resulting in a low bias near $SZA = 90^\circ$. This low bias results in false PMC detections. Due to these unphysical high frequencies, the ascending node data is excluded for all analyses shown below, with the exception of coincidence analysis results, as explained in Section 2.3.2.2. Improvement of ascending node data is planned for future work. Note that the results shown here are specific to the single- wavelength, SBUV-type algorithm applied to the CIPS or SBUV data; the same artifacts might not necessarily occur in the standard SBUV processing described by Deland *et al.* [2007], which also takes advantage of the multiple wavelengths observed by SBUV. Further, this problem is not relevant to the CIPS operational data products, which utilize a significantly different retrieval algorithm.

2.3.2.2 Coincidence analysis

Because PMCs are known to change substantially during short periods of time, and show marked variations in local time and longitude [Thomas and Olivero, 1989; von Zahn *et al.*, 1998; Chu *et al.*, 2001a; Shettle *et al.*, 2002], comparisons for spatially and temporally coincident measurements are presented in this section. Figure 2.16 shows scatter plots of coincident measurements of CIPS PY and SBUV NOAA-17 daily frequencies (left), cloud albedo (middle), and background albedo (right) from all seasons. Coincidences include only those measurements from CIPS and SBUV that were taken within 100 km and 2 h in local time. Most coincidences are found at latitudes between 78°N and 83°N in the NH and between 79°S and 83°S in the SH. These higher latitudes generally do not coincide with the high SZAs that showed problems in the ascending node data as explained in Section 2.3.2.1. Thus we believe that the single-wavelength, SBUV-type detection algorithm produces reasonable results for coincidence locations on the ascending node, and therefore we include the ascending node data in these coincidence comparisons. The agreement in frequency and cloud albedo is excellent, with both instruments measuring similar day-to-day variability (not shown). The CIPS mean frequency is higher than the SBUV frequency by $0.6 \pm 0.3\%$. The mean cloud albedo calculated from CIPS is $1.5 \pm 0.6\%$ lower than the SBUV cloud albedo.

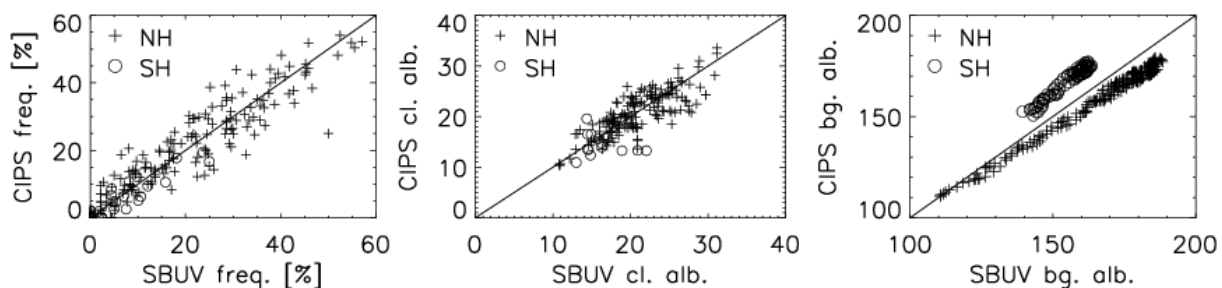


Figure 2.16: Scatter plots of coincidence results for NH 2007 to SH 2008 in the NH (plus symbols) and in the SH (open circles). Left: occurrence frequency; middle: cloud albedo; right:

background albedo. Albedo units are 10^{-6} sr^{-1} . Coincidences are found at latitudes of $80 \pm 3^\circ$ in both descending and ascending node data.

The comparison of the Rayleigh scattering background albedo (right panel in Figure 2.16) shows a systematic bias depending on hemisphere: in the NH the background albedo from CIPS is $4.9 \pm 0.1\%$ lower than from SBUV; in the SH the CIPS background albedo is $7.5 \pm 0.1\%$ higher than from SBUV. Benze *et al.* [2009] examined only the NH 2007 season, and thus only reported the lower CIPS background. As an explanation it was hypothesized that since many CIPS pixels are averaged into the 150 km x 150 km footprint, CIPS should have a much better signal to noise ratio than SBUV. As a consequence, CIPS would be more sensitive to faint clouds, thus leading to a higher SBUV background, which includes some cloud pixels that pull the background up. Taking into account more seasons, this hypothesis no longer holds, since depending on hemisphere, the CIPS background is either lower or higher than SBUV. At the current time, this hemisphere-dependent bias is not completely understood. Differences between the CIPS and SBUV orbit geometry likely play a role: at the latitudes of coincidences, in the NH (SH), the average CIPS SZA is larger (smaller) than the average SBUV SZA. The average NH (SH) SZA of coincident measurements is 66.8° (72.0°). In this SZA region the background albedo starts decreasing steeply with SZA. Thus the larger (smaller) CIPS SZA in the NH (SH) would lead to a smaller (larger) CIPS background albedo, which is consistent with the observed NH/SH bias. Nevertheless, even for those few coincident measurements, which have very similar SZA values, a small hemispheric bias in the background comparisons remains. Understanding the source of this discrepancy is a topic of future research.

2.3.3 PX and operational analysis

The analysis described above utilized only backscatter data from the nadir portion of the PY camera because SBUV measurements only include backscatter data. Back scattering (forward scattering) is defined as $SCA > 90^\circ$ ($SCA < 90^\circ$). However, CIPS also makes measurements of forward scattering, for which an improvement in cloud detection sensitivity is expected. The phase function for PMC particles increases more rapidly with decreasing SCA than the Rayleigh phase function. Thus, at small (forward) SCAs, a cloud signal is easier to distinguish from the background signal than at any other SCA. In this section we thus compare the CIPS PY results to the results of two additional CIPS analyses: (1) an SBUV-type analysis of data from the forward (PX) camera and (2) the operational retrieval results.

For the SBUV-type analysis of PX camera data, we first choose an SBUV-size footprint at the front edge of the camera, which is where the observations with the smallest SCAs are made. The SBUV-type algorithm is the same as for nadir data, with the following modification. The view angle for these pixels is far from nadir, thus elongating the path of the light through the atmosphere, and assuming a horizontal PMC structure, the PMC itself. Measurements at different view angles are standardized by normalizing to a nadir-viewing geometry; this is accomplished by multiplying the observed albedo by the cosine of the view angle. Figure 2.17 compares cloud frequencies determined in this manner from the PX camera to those described above from the PY camera, averaged over all latitudes from 65–85°. The large-scale, day-to-day variations in cloud frequencies are similar in the two cases, providing some support for the relative accuracy of the PX camera data. In terms of absolute accuracy, on average over all latitudes and times PX frequency is 40% higher and PX cloud albedo (not shown) is $17 \times 10^{-6} \text{ sr}^{-1}$

lower than the PY results. This is due to the higher cloud detection sensitivity mentioned earlier, which results in more and fainter clouds being detected by the PX analysis.

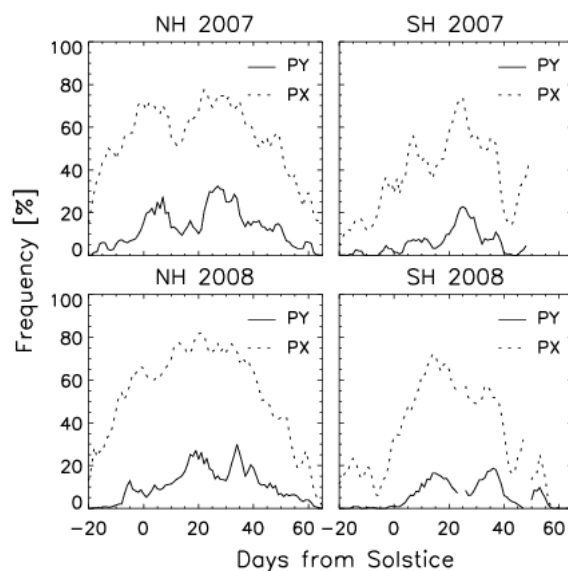


Figure 2.17: PY (solid) and PX (dotted) frequency vs. DFS for all latitudes (65° to 85°). The PY and PX footprint size is 150×150 km. Clockwise from top left: NH 2007, SH 2007, SH 2008, NH 2008. Descending node data only.

More rigorous comparisons of cloud frequencies from the SBUV-type algorithm applied to data in the PX and PY cameras are shown in Figure 2.18. The time series here pertain to daily cloud frequencies in the latitude range from 65° to 85° in each hemisphere. This figure also shows comparisons with the operational algorithm. For these comparisons, the PY and PX footprints were decreased from $150 \text{ km} \times 150 \text{ km}$ to the $15 \text{ km} \times 15 \text{ km}$ footprint size of the operational algorithm. In addition, to quantitatively compare the PY measurements to the PX and operational algorithm, it is necessary to account for the different cloud sensitivities arising from the geometrical configuration of the cameras. To accomplish this, only clouds brighter than $14 \times 10^{-6} \text{ sr}^{-1}$ are included in the PX and operational time series shown in Figure 2.18. This threshold was chosen empirically to optimize the agreement between the operational, PX, and PY results. Given the scattering angle ranges sampled by the PX and PY cameras, a threshold of $14 \times 10^{-6} \text{ sr}^{-1}$

¹ would be broadly consistent with spherical particle radii on the order of 30–40 nm, assuming a constant, unimodal Gaussian size distribution with width 14 nm. Because of the oversimplification implied by this assumption, the choice of threshold should not be interpreted rigorously; nevertheless, it is in reasonable agreement with the median particle radii reported by Hervig *et al.* [2009b]. Figure 2.18 shows that with this threshold the frequency time series can be brought into very good agreement; for instance, the large-scale seasonal variations and the day-to-day variability are similar. Although not shown, the differences do not exhibit any systematic latitude dependence. The largest area of disagreement is at the end of the seasons (days 40–60), when the PY frequencies are larger than the PX or operational frequencies. At this time the scattering angles sampled by the cameras are changing more rapidly than earlier in the season. These differences possibly result, therefore, from the fact that we are applying just a single threshold to the entire season. Overall, we believe that the comparisons here provide confidence that the CIPS operational detections of the brightest clouds are reasonable.

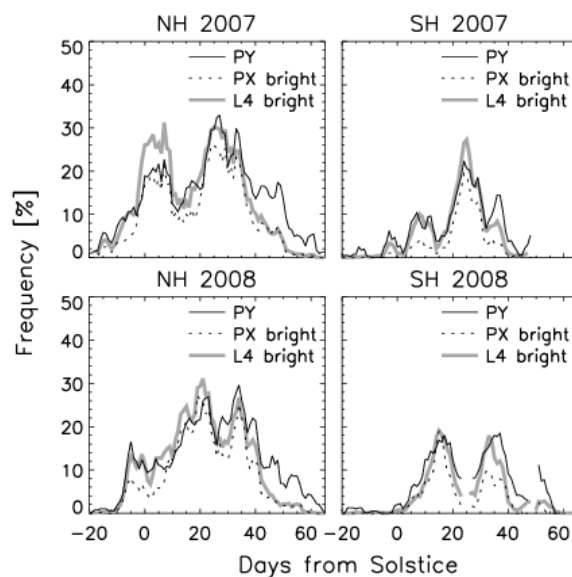


Figure 2.18: PY (solid), $PX > 14 \times 10^{-6} \text{ sr}^{-1}$ (dotted), and $L4 > 14 \times 10^{-6} \text{ sr}^{-1}$ (grey solid) frequency vs. DFS for all latitudes (65° to 85°). The PY and PX footprint size is decreased to the L4

footprint size of 15 x 15 km. Top left: NH 2007, bottom left: NH 2008, top right: SH 2007, bottom right: SH 2008. Descending node data only.

Occurrence frequencies derived from the 150 km x 150 km footprints on PX and PY (Figure 2.17) are about the same as frequencies derived from the 15 km x 15 km footprints (Figure 2.18 for PY; not shown for PX since only the bright clouds are shown in Figure 2.18). Thus, the resolution of these footprints does not play a significant role for occurrence frequency. However, there must be a limit to this rule. In the extreme case of choosing a footprint that is as big as the polar cap, for instance, and assuming that the footprint covers the high latitudes on a day with plenty of clouds present, the occurrence frequency must be 100%. The size of a footprint necessary to have an increasing effect on occurrence frequency is currently unknown. In any case, the SBUV footprints used here are evidently not yet big enough to have a significant influence on frequency.

As noted above, the approach we have adopted for normalizing cloud albedo to 90° SCA assumes a constant r_m for all measurements, disregarding seasonality and latitudinal dependence. This is clearly not realistic, as shown for example by Rusch *et al.* [2008], Robert *et al.* [2009], and Hervig *et al.* [2009b]. Thus this normalization approach only provides a rough estimate of a seasonally averaged PX cloud albedo, which must be considered when interpreting the results. The value of r_m that we use agrees with average results from the CIPS operational algorithm [Bailey *et al.*, 2009]. Increase in r_m or increase in σ (which is assumed) both lead to decrease in cloud albedo after the normalization. For example, if we double r_m from 40 to 80 nm while assuming $\sigma = 14$ nm, the average cloud albedo decreases by 59.1%. Doubling σ from 10 to 20 nm while keeping r_m at 55 nm, the average cloud albedo decreases by 35.4%. The normalization thus leads to large uncertainties in the inferred cloud albedo. Thus, PX occurrence frequencies

that use clouds brighter than a certain threshold should be interpreted with caution. Nevertheless, the fact that Figure 2.18 shows reasonable agreement in the occurrence frequencies between all three methods suggests that the CIPS data from all cameras is robust.

Next we compare the operational retrievals to the SBUV-type PX retrievals for both bright and faint clouds. We again employ a PX footprint size of 15 km x 15 km, to match the operational footprint. In this case, however, both analyses use a cloud albedo threshold of $1 \times 10^{-6} \text{ sr}^{-1}$, rather than $14 \times 10^{-6} \text{ sr}^{-1}$, because the operational and PX analyses both incorporate the more sensitive, forward-scattering observations. Figure 2.19 compares the time series of operational and PX frequencies during the NH 2007 season for the 80 - 85°N and 70 - 75°N latitude bands. The left panel compares the PX and operational results at high latitudes, showing excellent agreement in both the overall frequencies and day-to-day variability. That such remarkable agreement is found between the SBUV-type analysis of PX measurements and the operational results strongly supports the validity of the operational results, since these algorithms are completely independent.

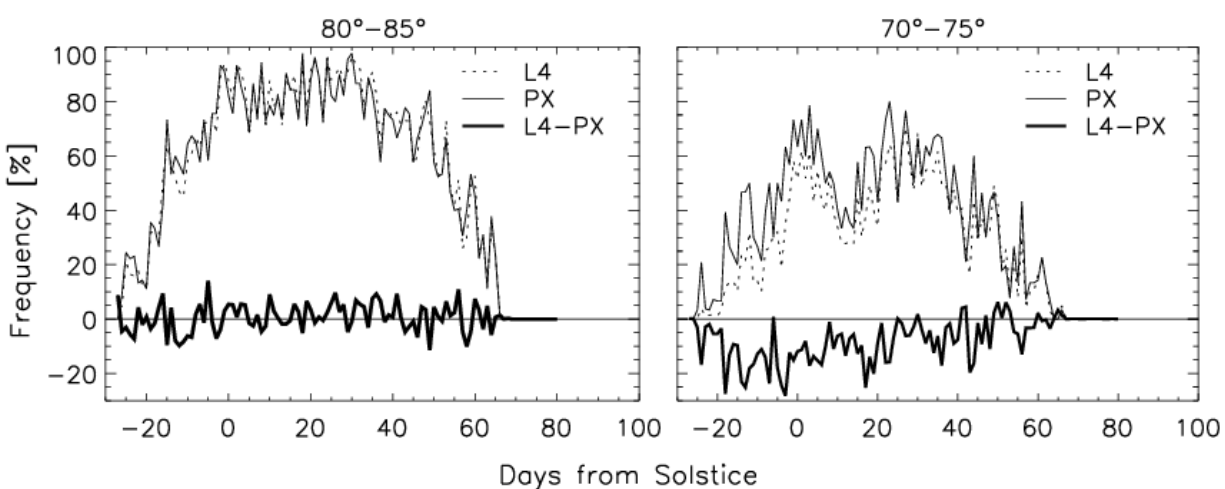


Figure 2.19: NH 2007 PX (thin solid) and operational (L4, dotted) frequencies and differences, L4-PX (thick solid), vs. DFS for latitudes of 80°N to 85°N (left) and 70°N to 75°N (right). PX footprint size is 15x15 km. Descending node data only.

The right panel compares the PX and operational results at lower latitudes, where the operational frequency is somewhat smaller than the PX frequency. This systematic latitudinal behavior is obvious in Figure 2.20, which shows scatter plots of the operational and PX frequencies in different latitude bands. The dashed lines indicate perfect agreement, whereas the solid lines are linear regressions to the data. The difference in frequency, L4-PX, ranges from $0.6 \pm 0.5\%$ at $80\text{--}85^\circ$ latitude to $-9.8 \pm 0.6\%$ at $70\text{--}75^\circ$ latitude. We offer two possible explanations for the increase in discrepancies at low latitudes. (1) At lower latitudes in the descending node data fewer measurements are available for calculation of the phase function, a requirement for the operational algorithm, and those measurements that are available correspond primarily to $\text{SCA} > 90^\circ$. Thus the operational algorithm detection capability declines at low latitudes on the descending node. The SBUV-type analysis does not rely on a phase function approach, so it does not have these restrictions at the lower latitudes. This might contribute to the operational frequency being lower than the PX frequency at lower latitudes. (2) The v3.20 operational algorithm imposes a conservative cloud detection limit that results in zero false detections out-of-season, whereas the SBUV-type algorithm was designed to be consistent with the SBUV algorithm of DeLand *et al.* [2003; 2006b], which yields out-of-season (false) cloud detection frequencies of $<1\%$. Thus the more conservative approach taken by the CIPS operational algorithm might explain the lower frequencies at low latitudes, where the cloud brightness is close to background levels.

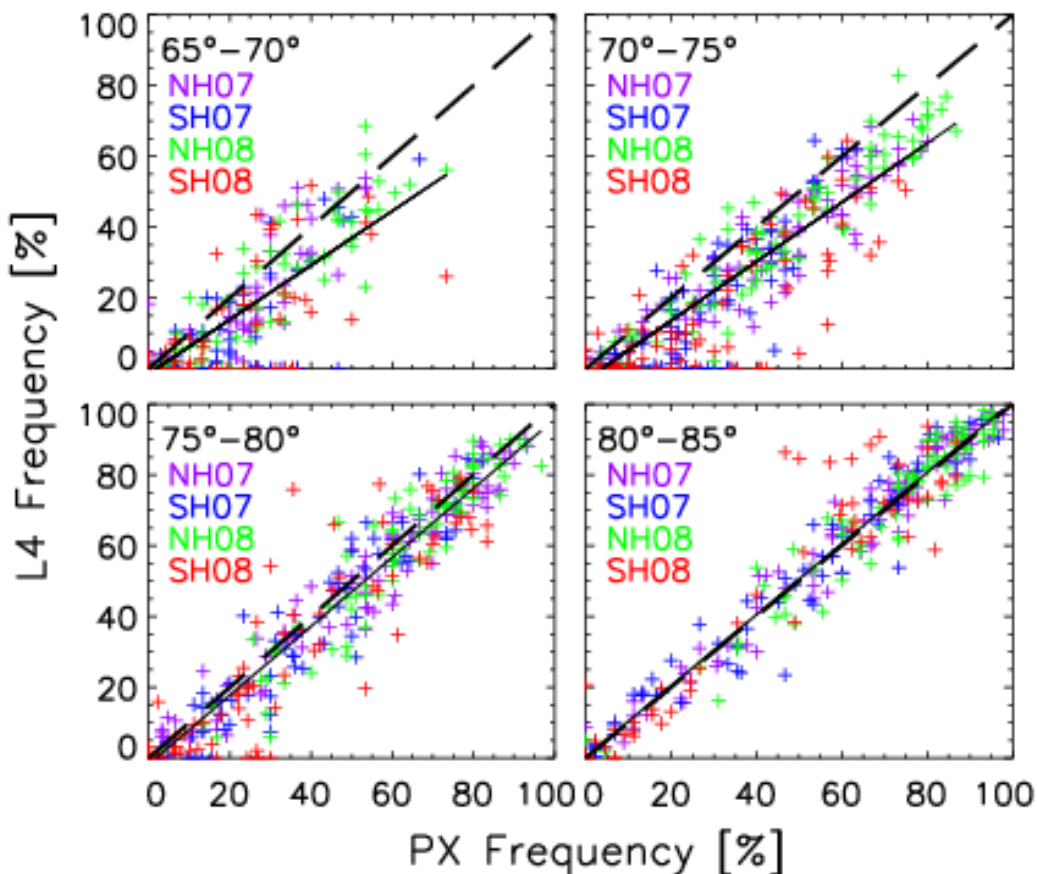


Figure 2.20: Scatter plots of PX and operational (L4) frequency in different latitude bands: top left: 65-70°, top right: 70-75°, bottom left: 75-80°, bottom right: 80-85°. PX footprint size is 15 x 15 km. Points are color-coded to denote the season; descending node data only. Dashed lines are one-to-one correspondence; solid lines are linear regressions to the data.

2.3.4 Summary

Measurements of PMC occurrence frequency, cloud albedo and Rayleigh scattered background albedo from SBUV/2 and AIM CIPS have been compared. The work presented extends the results from Benze *et al.* [2009] by updating the analysis from one to four seasons (NH07 to SH08) and adding a comparison to the CIPS operational algorithm, which is based on calculation of the scattering phase function of cloud particles. The simple SBUV- type algorithm,

which is based on the original SBUV algorithm but ignores spectral information, serves as a link between the results from SBUV and the operational algorithm.

When the SBUV-type algorithm is applied to SBUV and the CIPS PY nadir data, zonal average occurrence frequencies compare very well. CIPS frequency is $0.2 \pm 0.1\%$ higher than SBUV frequency. Coincident measurements, which are defined to occur within 100 km and 2 h in local time, also agree very well. Frequencies calculated from CIPS data are on average higher by $0.6 \pm 0.3\%$ than frequencies calculated from coincident SBUV data. Cloud albedo calculated from CIPS is $1.5 \pm 0.6\%$ lower than coincident measurements of SBUV cloud albedo. However, Rayleigh scattering background albedo shows an unexplained systematic difference that changes with hemisphere. In the NH the background albedo from CIPS is $4.9 \pm 0.1\%$ lower than from SBUV; in the SH the CIPS background albedo is $7.5 \pm 0.1\%$ higher than from SBUV. At the current time we do not understand these background albedo differences, although SZA differences in the coincident measurements can likely explain part of the discrepancy.

The SBUV-type analysis of CIPS data was extended to a footprint on the front of the PX camera, which is located on the CIPS scene where mostly forward scattering is detected. It was shown that day-to-day variations in cloud frequency inferred from the PY and PX cameras were consistent with one another. Therefore, using the PY camera as a transfer standard from SBUV to CIPS PX, these results give confidence in the measured PX albedos. Although intra-seasonal variability in the PY and PX measurements was similar, cloud frequencies inferred from measurements in the PX camera were significantly higher than from measurements in the PY camera. This difference is well understood, and results from the higher sensitivity of the PX camera to cloud detection, because of the forward scattering angles that it samples.

The SBUV-type results were then compared to the CIPS v3.20 operational L4 results, which utilize CIPS measurements of radiation scattered in the forward and backward directions. Since the L4 results have a resolution of 15 km x 15 km, for these comparisons the PX and PY footprints were defined as 15 km x 15 km areas. The occurrence frequencies calculated from the SBUV-type analysis of CIPS data from both the PY and PX cameras generally compare well to frequencies calculated from the operational retrievals if only the brightest clouds are taken into account. This requires applying an empirically derived threshold of $14 \times 10^{-6} \text{ sr}^{-1}$ to the SBUV-type analysis of PX data and to the operational retrieval results. When all clouds are taken into account, frequencies from the PY camera are lower, as expected, than from the PX or operational data. The latter two agree exceptionally well at high latitudes; the operational frequencies are on average lower than the PX frequencies by $0.6 \pm 0.5\%$ at 80–85° latitude. The agreement declines at lower latitudes, to $-9.8 \pm 0.6\%$ at 70–75° latitude. These disagreements might be related to the choice of cloud detection threshold in the two algorithms, or to requirements imposed on the operational algorithm of multiple forward and backward scattering observations at the same location.

Overall, we conclude from the above comparisons that the CIPS PMC occurrence frequencies derived from the operational L4 algorithm are valid for scientific analysis.

The results suggest that some caution is warranted, however, when interpreting CIPS v3.20 cloud measurements on the descending node equatorward of 75° latitude where many of the ground based NLC observations are made. Here, the CIPS operational retrieval algorithm limitations lead to small (<10%) under- estimates of the occurrence frequency. CIPS operational algorithm improvements that address these limitations are currently under development. Due to

limitations of the SBUV-type algorithm described in Section 2.3.2, no validation of CIPS v3.20 operational ascending node frequency is presented in this paper.

Acknowledgments

Funding for CIPS data evaluation, and for the AIM mission, was provided by the NASA Small Explorer program under Contract NAS5-03132. The SBUV/2 data were obtained from NOAA/NESDIS with support from the NOAA Climate and Global Change Atmospheric Chemistry Element. Matt T. DeLand was partially supported by the NASA Geospace Science program through Grant no. NNH09CF72C.

3 Teleconnections and the PMC Season Onset

Karlsson *et al.* [2009b; 2011] used the validated CIPS data to investigate atmospheric teleconnections. These investigations included analysis of both inter- and intra-hemispheric coupling. As described more below, we found that day-to-day variability of the clouds in the SH 2007-2008 season was controlled largely by NH (winter) hemisphere meteorology. It was found that the season onset defined by CIPS data for three seasons was controlled by meteorology in the summer stratosphere below the clouds. Following on from these studies, Benze *et al.* [2012] investigate and quantify different mechanisms that control the onset date of the PMC season in both hemispheres: intra-hemispheric coupling with the same hemisphere (Section 1.3.1), inter-hemispheric coupling with the opposite hemisphere (Section 1.3.1), and variations in the solar cycle (Section 1.3.3). Taken as a whole, this work has accomplished one part of the culminating goal of the AIM mission – to establish the basis for the investigation of long-term change in the mesosphere. That is, AIM data were used to specify relevant mechanisms that control PMC variations; these mechanisms were further investigated and found to control longer term variations observed by previous instruments – but never before explained. This chapter describes these investigations in Section 3.1 and Benze *et al.* [2012] in Section 3.2, who for the first time combined all three effects, intra-, inter-hemispheric coupling, and the solar cycle, in a multiple linear regression analysis and quantified their relative importance in controlling NH and SH PMC onset dates.

3.1 Summary

Previous studies [Karlsson *et al.*, 2011; Gumbel and Karlsson, 2011] have shown that in recent years the SH PMC onset dates have largely been controlled by *intra*-hemispheric coupling; specifically, by the timing of the same-hemisphere stratospheric wind reversal from its winter to summer state. Since seasonally varying stratospheric and mesospheric zonal winds control GW amplitudes and breaking levels through GW filtering, these winds impact mesopause temperatures and therefore PMCs, as described in Section 1.3.1. A late SH wind reversal corresponding to a long-lasting polar vortex leads to later dynamical cooling of the mesopause region, thereby delaying the onset of the SH PMC season. Karlsson *et al.* [2011] and Gumbel and Karlsson [2011] showed this effect using three SH seasons of CIPS and SOFIE data and nine SH seasons of OSIRIS data, respectively. In the NH, however, the stratospheric wind reverses about two months prior to the actual season onset, so it does not influence the onset [Gumbel and Karlsson, 2011].

Previous studies have also described other processes that affect polar summer mesopause temperatures, although the effects of these processes on the season onset have not previously been investigated. As explained in Section 1.3.1, summer polar mesopause temperatures are affected by the winter stratosphere through an *inter*-hemispheric coupling mechanism. Stronger PW activity in the winter hemisphere causes higher temperatures over the summer pole and fewer PMCs [Karlsson *et al.*, 2007; 2009a; 2009b]. For a long time it has also been known that the solar cycle affects PMCs through a decrease of water vapor due to larger photolytic destruction rates and an increase of temperature due to stronger UV heating rates (see Section 1.3.3).

Benze *et al.* [2012] extends these previous findings. We extend the results of Karlsson *et al.* [2011] and Gumbel and Karlsson [2011], showing that their explanation of intra-hemispheric coupling as a controlling factor in the SH PMC onset pertains to historical data from 28 years of SBUV data: year-to-year variability in SH stratospheric winds is highly correlated to the onset of SH PMC seasons. Apart from the available long time series of PMC observations, the SBUV instruments are ideally suited for this kind of study: the PMC onset of each season is calculated as the average of at least two SBUV observations (ascending and descending node) of the PMC onset, and up to eight observations (both nodes from four instruments). Therefore, sampling at different local times and scattering angles, which may influence the timing of the PMC onset, can be excluded as major drivers of the season onset variability observed by SBUV.

In addition to intra-hemispheric coupling effects, the impact on PMC onset dates of variations in winter stratospheric winds (inter-hemispheric coupling) and the solar cycle are also included. Even though previous studies have presented inter-hemispheric coupling effects between winter stratospheric winds and summer mesopause temperatures, PMC radii, and frequency [Karlsson *et al.*, 2007; Karlsson *et al.*, 2009b], the effect on the PMC season onset dates has not been shown previously. Likewise, even though the effect of the solar cycle on PMCs has long been known, any modulation of the PMC season onset with the solar cycle has not previously been presented in the literature. Benze *et al.* [2012] combine all three components (intra-hemispheric coupling, inter-hemispheric coupling, and the solar cycle) in a multiple linear regression analysis of the PMC season onset, resulting in a remarkably high correlation between the observed onset dates and the linear regressed onset dates in the SH. The linear regression coefficients quantify the relative importance of each forcing component and show that the SH PMC season onset is controlled primarily by the timing of the SH stratospheric wind reversal

from its winter to summer state, with a smaller but still important contribution from the solar cycle.

Previous studies are extended further by relating the NH PMC season onset dates to the solar cycle and winter stratospheric winds through inter-hemispheric coupling. Gumbel and Karlsson [2011] stated that the NH PMC onset dates are not related to the same-hemispheric wind, but alternative controlling factors were not suggested. Benze *et al.* [2012] show that inter-hemispheric coupling triggered by winter stratospheric wind variations plays a big role in controlling the NH PMC season onset dates, with additional control by the solar cycle. For the NH, multiple linear regression was carried out with the opposite hemispheric wind speed and solar cycle as linear components. The correlation of observed NH PMC onset dates and linearly regressed onset dates is slightly smaller than in the SH, suggesting unidentified processes that are more important in the NH than SH, for example 2-day or 5-day planetary waves. As mentioned earlier, the effects of tides were not part of this study since the SBUV PMC onset dates were acquired at vastly different local times and averaged into a mean PMC onset date.

Figure 3.1 shows the SH stratospheric wind reversal dates calculated from the European Centre for Medium-Range Weather Forecasts (ECMWF) Re-Analysis (ERA-40) and the United Kingdom Meteorological Office (MetO) Unified Model zonal mean wind. The stratospheric wind reversal date is defined as the day of final decrease of the mean zonal wind at 50 hPa and 65°S below 10 m/s. Despite high variability, the SH wind reversal date shows a positive trend after around 1980, indicated by the red line in Figure 3.1. This trend is suggested to be due to the Antarctic ozone hole, which is characterized by extensive destruction of lower stratospheric ozone by anthropogenic chlorofluorocarbons (CFCs) throughout the polar vortex region during the southern spring [Smith *et al.*, 2010, Lossow *et al.*, 2012]. Reduced ozone concentrations

result in less heating by absorption of solar radiation. A colder polar winter stratosphere enhances the equator-pole temperature gradient, thus increasing the wind speed of the polar night jet surrounding the polar vortex, making it less prone to disruption by planetary wave activity and thereby delaying the final warming. Therefore a deeper Antarctic ozone hole delays the SH PMC onset (Section 1.3.1, Karlsson *et al.*, 2011, Gumbel and Karlsson, 2011). WMO [2007] states that although severe Antarctic ozone holes continue to occur, they have not worsened since the late 1990s, and largely because of dynamical effects, ozone levels have been higher in some years since the turn of the century. It is predicted that Antarctic total ozone will slowly recover to 1980 levels by 2060-2075 due to a successful reduction of ozone destroying substances mainly from CFCs. With summer mesopause temperatures being strongly influenced by the stratospheric wind reversal dates, PMC season onset dates are expected to reflect any long-term trends in stratospheric winds and thus also the recovery of the Antarctic ozone hole. This finding is in contrast to the effects of increasing concentrations of CO₂ and methane that are thought of causing an increase PMC occurrence and brightness as described in Section 1.3.4. These would be expected to cause a trend towards earlier PMC season onset dates. It is important to keep in mind that effects due to increasing mesospheric CO₂ and methane from global climate change in the SH may compete with dynamical changes due to changes in the Antarctic ozone hole.

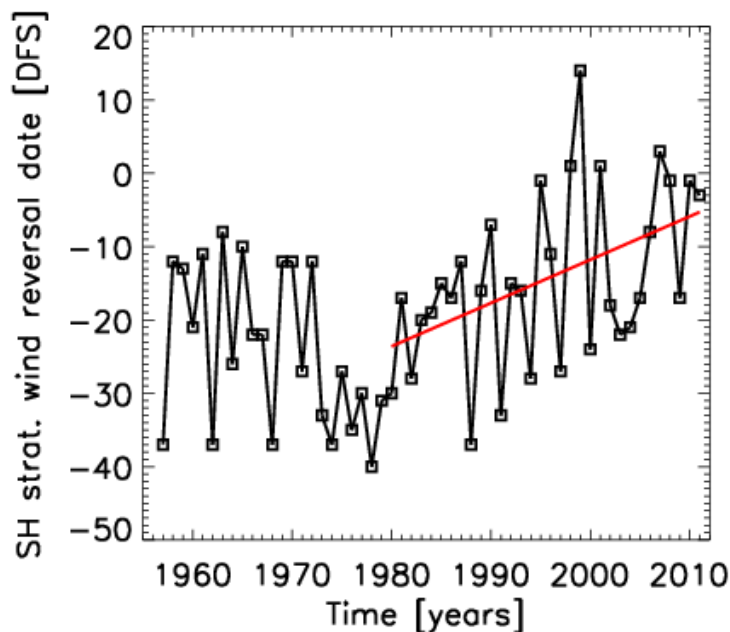


Figure 3.1: SH stratospheric wind reversal dates (definition see text) from ERA-40 and ECMWF. The red line indicates the linear trend after 1980.

3.2 Benze *et al.* [2012]: On the onset of polar mesospheric cloud seasons as observed by SBUV²⁰

Susanne Benze^{1,2}, Cora E. Randall^{1,2}, Bodil Karlsson³, V. Lynn Harvey¹, Matthew T. DeLand⁴, Gary E. Thomas¹, Eric P. Shettle⁴

¹Laboratory for Atmospheric and Space Physics, Univ. CO, Boulder, Colorado, USA

²Department of Atmospheric and Oceanic Sciences, Univ. CO, Boulder, Colorado, USA

³Department of Meteorology, Stockholm University, Stockholm, Sweden

²⁰ Reproduced by permission of American Geophysical Union. Benze, S., C. E. Randall, B. Karlsson, V. L. Harvey, M. T. DeLand, G. E. Thomas, and E. P. Shettle, On the onset of polar mesospheric cloud seasons as observed by SBUV, *Journal of Geophysical Research*, 117, D07104, 2012. Copyright [2012] American Geophysical Union.

⁴Science Systems and Applications, Inc., Lanham, Maryland, USA

Abstract

This paper describes an investigation using data from the Solar Backscatter Ultraviolet (SBUV) satellite instruments to explore and understand variations in the timing of the onset of Polar Mesospheric Cloud (PMC) seasons. Previous work has shown that for several recent SH seasons, the PMC season onset was controlled by the timing of the shift from winter to summer zonal wind flow in the SH stratosphere. We extend the analysis of PMC season onset to 28 years of SBUV observations, including both hemispheres. A multiple linear regression analysis of SBUV data from 1984 - 2011 suggests that the SH PMC season onset is delayed by one day for every day that the zonal wind at 65°S and 50 hPa (~20 km) remains in a winter-like state. In addition, we find that the solar cycle plays a role: The SH season onset is delayed by about ten days at solar maximum compared to solar minimum. In the NH, the PMC season onset is delayed by ~7 days at solar maximum compared to solar minimum; variations in the NH stratospheric wind, however, are not correlated with the NH onset date. On the other hand, inter-hemispheric teleconnections are important in the NH; a one-day shift in the NH season onset corresponds to a shift of ~1.4 m/s in the SH stratospheric wind at 60.0°S and 20 hPa (~26 km). Neither the NH nor the SH season onset date is correlated with the Quasi-Biennial Oscillation, North Atlantic Oscillation, Arctic Oscillation, or El Niño Southern Oscillation.

3.2.1 Introduction

Polar Mesospheric Clouds (PMCs), Earth's highest clouds, form in the summer polar mesopause region, which is the coldest place in the atmosphere. They are observable from ground and space, and provide an indication of the thermal and dynamical conditions of the upper mesosphere. PMCs are highly dependent on mesospheric temperatures, which are modulated by the meridional circulation, planetary waves (PWs), gravity waves (GWs), tides, and the solar cycle.

The upper branch of the Brewer-Dobson circulation consists of upwelling in the summer polar mesosphere and downwelling in the winter polar mesosphere. This circulation is driven by breaking GWs. GWs are vertically propagating waves that are caused by flow over topography, frontal processes, convection, and jet streams [Fritts and Alexander, 2003]. With increasing altitude GW amplitudes grow exponentially due to decreasing atmospheric density. Eventually the wave becomes convectively unstable, breaks, and deposits angular momentum in the same direction as the GW phase speed. This momentum deposition is also called GW drag.

The seasonally varying stratospheric zonal wind controls GW amplitudes and breaking levels through GW filtering. GWs can only propagate vertically when their phase speed either exceeds the zonal wind speed or is of the opposite direction. During summer, the mean stratospheric and mesospheric zonal wind is directed westward, so GWs with westward phase speeds are filtered. Thus in the summer hemisphere breaking GWs cause a net eastward drag in the upper mesosphere, decelerating the mean zonal flow [Holton and Alexander, 2000]. This transfer of angular momentum can only be balanced by the Coriolis torque [Shepherd, 2007]. The Coriolis force acts on the induced eastward flow, with balance re-established once the flow is directed equatorward. Mass conservation and the principle of downward control then require that upwelling occur in the summer polar mesosphere [Shepherd, 2000]. The resulting adiabatic

cooling in the summer mesosphere causes deviations from radiative equilibrium temperatures by more than 60K [Holton and Alexander, 2000; Lübken *et al.*, 2009]. Only this GW induced dynamical pump allows PMCs to form in the summer polar mesopause region. In summary, GWs and stratospheric/mesospheric zonal winds, because of their filtering influence, impact mesopause temperatures and therefore PMCs.

Even though the mechanism driving this dynamical pump is the same in the NH and SH, a hemispheric asymmetry in the summer polar mesospheric temperature of up to 7.5 K was observed by Hervig and Siskind [2006], Wrotny and Russell [2006], and Morris *et al.* [2009]. The hemispheric temperature asymmetry is the main reason for less frequent, dimmer, and less extensive PMCs in the SH [Olivero and Thomas, 1986; Bailey *et al.*, 2005; Petelina *et al.*, 2005; Bailey *et al.*, 2007; Shettle *et al.*, 2010] as well as Polar Mesospheric Summer Echoes [Balsley *et al.*, 1993; 1995; Woodman *et al.*, 1999]. Siskind *et al.* [2003] explained a hemispheric temperature asymmetry of 3-8K as being caused by hemispheric differences in GW wind filtering and radiative effects. Such hemispheric differences might influence the timing of the PMC season onset. Gumbel and Karlsson [2011] found that the timing of PMC onset is more variable in the SH than in the NH. Based on a model study and observations of PMCs from the Aeronomy of Ice in the Mesosphere (AIM) mission, Karlsson *et al.* [2011] suggested that the SH PMC onset date is largely controlled by changes in the timing of the winter-to-summer stratospheric wind reversal. They argue that a more ‘winter-like’ (‘summer-like’) stratospheric mean flow would lead to a warmer (colder) polar mesosphere, using the arguments presented above. Therefore, a late wind reversal, which would correspond to a long-lasting SH polar vortex, would lead to later dynamical cooling of the mesopause region above, thereby delaying the onset of the SH PMC season. On the other hand, increased PW activity in the SH would

cause an earlier breakdown of the polar vortex and lead to an earlier onset of the SH PMC season. Using the Canadian Middle Atmosphere Model, they demonstrated this mechanism in a statistically significant way. Gumbel and Karlsson [2011] confirmed this mechanism using nine years of Odin satellite data.

Several studies [e.g., Becker and Schmitz, 2003; Karlsson *et al.*, 2007] have shown that the polar summer mesopause region is also affected by the winter stratosphere through an inter-hemispheric coupling mechanism. This mechanism is triggered by PW induced changes in the zonal wind that alter GW filtering. In cases where the winter stratosphere is highly disturbed by PWs, the usually strong eastward zonal wind inside the polar vortex is disturbed and weakened, sometimes even reversed. GW filtering through the zonal wind will therefore result in weaker westward GW drag in the winter mesosphere. The combined PW and GW effects induce changes in the circulation that cause a quadrupole structure in the winter hemisphere temperature anomaly field, as described by Karlsson *et al.* [2009a] and Becker *et al.* [2004]. That is, the high-latitude stratosphere and low-latitude mesosphere warm while the high-latitude mesosphere and low-latitude stratosphere cool. The low-latitude, mesospheric warming changes the meridional temperature gradient to the summer polar mesosphere, leading to changes in zonal winds, GW filtering, meridional circulation, and upwelling that result in a warmer summer polar mesosphere. Thus, stronger PW activity in the winter hemisphere results in higher temperatures over the summer pole and fewer PMCs. Analogous arguments can be made that weaker winter hemisphere PW activity leads to a higher probability of summer hemisphere PMCs. Karlsson *et al.* [2007; 2009a; 2009b] presented the effect of inter-hemispheric coupling on mesopause temperatures, PMC effective radii, and PMC occurrence frequency during the PMC season, but not on the PMC onset.

We also expect that the timing of the PMC season onset may be affected by the solar cycle. The solar cycle has long been known for its effect on PMCs through photodissociation of water vapor by Lyman- α radiation [Garcia 1989, Thomas *et al.*, 1991]. Additionally, mesospheric temperature is modulated by the changing solar UV heating rate between solar minimum and maximum conditions. These two effects lead to an \sim 11-year modulation of PMC occurrence frequency, with lower frequencies during solar maximum and higher frequencies during solar minimum conditions [Thomas *et al.*, 1991]. Thus we would expect that on average, during solar maximum conditions the PMC season may start later than during solar minimum conditions. Even though the effect of the solar cycle on season-average PMC frequency is well known, any effect of the solar cycle on the PMC season onset date has not yet been documented.

In this paper we investigate variability from 1984 to 2011 in the PMC season onset date in both hemispheres using observations from the Solar Backscatter UltraViolet (SBUV) series of instruments [DeLand *et al.*, 2003; 2006b; 2007]. We extend the studies of Karlsson *et al.* [2011] and Gumbel and Karlsson [2011] to investigate whether their explanation for the SH PMC season onset pertains to historical data. We also look for other mechanisms that might be contributing to variability in the PMC onset data, such as the solar cycle and inter-hemispheric coupling. Section 3.2.2 contains descriptions of data and analysis methods. Results are shown in Section 3.2.3 and conclusions are drawn in Section 3.2.4.

3.2.2 Data description and analysis

For the current work we correlate variations in PMC data for years 1984 to 2011 from the SBUV series of instruments with variations in meteorological data and the solar cycle. We

analyze the SBUV observations to calculate PMC occurrence frequency, from which the date of the PMC season onset is inferred. We use the meteorological analyses described below to calculate the timing of the reversal of the stratospheric zonal mean zonal wind from winter to summer conditions.

3.2.2.1 SBUV

The SBUV instruments have been launched since 1978, flying on the Nimbus-7, NOAA-9, NOAA-11, NOAA-14, NOAA-16, NOAA-18, and NOAA-19 satellites [DeLand *et al.*, 2003]. Satellites after Nimbus-7 carried the improved SBUV/2 instrument, but for simplicity in this paper all of the instruments will be referred to as SBUV. The SBUV instruments were originally designed to observe global stratospheric ozone but have also been used to measure PMCs [Thomas *et al.*, 1991; DeLand *et al.*, 2003, 2006b, 2007]. The SBUV instruments are nadir-pointed with a horizontal resolution of 150 x 150 km at PMC altitude and measure backscattered radiation at 12 wavelengths in the UV. PMCs are detected following the original technique developed by Thomas *et al.* [1991], which was refined by DeLand *et al.* [2007]. This technique is based on PMCs appearing as a spectrally enhanced signal above the backscattered signal in the UV (252.0 – 292.3 nm), with the maximum enhancement at the shortest wavelengths [DeLand *et al.*, 2003]. In the following, SH seasons will be referred to using the year of their onset, e.g., the SH00 season refers to the SH season that started towards the end of 2000 and extended through the first part of 2001.

3.2.2.2 Meteorological analyses

The European Centre for Medium Range Forecast (ECMWF) Re-Analysis (ERA-40) data are available from 1957-2002 [Uppala *et al.*, 2005]. Model output is provided four times daily at 0 UTC, 6 UTC, 12 UTC, and 18 UTC and has a horizontal resolution of 2.5° longitude by 2.5° latitude. The data are available on 23 pressure levels that extend from 1000 hPa up to 1 hPa. In this study, we use daily averaged zonal mean zonal wind data at 12 UTC, in both hemispheres.

Global assimilation analyses from the United Kingdom Meteorological Office (MetO) Unified Model are available from 1991 to the present [Swinbank and O'Neill, 1994]. The model uses three dimensional variational data assimilation [Lorenc *et al.*, 2000] and has a semi-Lagrangian dynamical core [Davies *et al.*, 2005]. Model output is provided once per day at 12 UTC on a 2.5° latitude by 3.75° longitude grid. The data are on 25 pressure levels between 1000 hPa and 0.1 hPa. Zonal mean zonal winds in both hemispheres are used to extend the zonal wind data record to the present.

ERA-40 and MetO overlapping wind data between 1991 and 2002 compare favorably to within half a percent. For the current work wind data from the two re-analyses were combined using ERA-40 between 1979 and 2001 and MetO between 2002 and 2011.

3.2.2.3 Definition of PMC season onset and stratospheric wind reversal

The PMC season onset is calculated using daily SBUV PMC occurrence frequency between 75° and 82° latitude with a 5-day running average applied separately for ascending and descending nodes. Season onset is defined as the date on which the frequency remains above 1.5% for at least seven consecutive days for the first time. This criterion is sufficiently conservative to filter out false cloud detections, which can cause frequencies of $\sim 0.5\%$ [DeLand

et al., 2007], and to reject sporadic frequency increases before the actual onset of the season. However, this criterion makes PMC season onsets calculated at lower latitudes, e.g., between 70°S and 75°S, more and more unreliable for two reasons: in some years the 1.5% cutoff frequency is a significant fraction of the maximum seasonal frequency and therefore pushes the season onset back unreasonably far; in some other years false pre-season detections at these lower latitudes result in a too early season onset. Since SBUV does not observe PMCs poleward of 82° latitude, the latitude interval of 75° to 82° was chosen. Information from Table 3 in DeLand *et al.* [2007] was used to exclude SBUV data in seasons that exhibited artifacts during the season onset time period. Since analysis of data from each SBUV instrument yields two season onset dates – one for the ascending node and one for the descending node – and some seasons are observed by several instruments (up to four), the reported season onset is the mean season onset. Potential PMC onset variability due to possible instrumental/observational effects and space shuttle launches will be discussed in Section 3.2.4.

It should be noted that PMC season onset as determined by SBUV is delayed by up to ~20 days compared to the date inferred from more sensitive instruments, such as the Cloud Imaging and Particle Size (CIPS) instrument and Solar Occultation For Ice Experiment on AIM; see, e.g., Benze *et al.* [2011] for a comparison of SBUV and CIPS detection capabilities. This can be attributed to the fact that SBUV observes only the brightest clouds, and therefore misses the dim and sparse clouds at the beginning of the season. SBUV and CIPS PMC onset correlate with a coefficient of 0.75 (0.91) in the SH (NH) (not shown), which indicates a good correlation of PMC onset dates between less and more sensitive instruments. However, since this analysis emphasizes the relative change of PMC season onset date from year to year, a consistent determination of PMC season onset date is more important for understanding the observed

variability than absolute accuracy. Moreover, SBUV offers the unique advantage of more than a quarter century of satellite-based cloud detections.

The daily mean stratospheric zonal mean zonal wind was calculated from the meteorological analysis data at 50 hPa (~20 km) and 65° latitude, and a 5-day running average was applied. The timing of the wind "reversal" from winter to summer conditions was defined as the day of the final decrease of the mean zonal wind below 10 m/s. This is the definition of the polar vortex breakup date that was first proposed by Waugh *et al.* [1999] and used by Langematz and Kunze [2006; 2008]; it avoids false detections of early vortex breakdown dates when major warmings occur in the middle of the winter.

3.2.2.4 Solar cycle data

Daily values of Lyman- α [Woods *et al.*, 2000; <http://lasp.colorado.edu/lisird/lya/>] are averaged from 30 to 10 days prior to solstice in the summer hemisphere to provide an indication of the state of the solar cycle at the beginning of the PMC season. Tests were run to evaluate the sensitivity of the results to the period chosen for the Lyman- α average. Conclusions were the same for all choices of averaging time period, which included -40 to -30, -30 to -20, -20 to -10, -10 to 0, 0 to 10, -40 to 10, -30 to 0, -20 to -10, and -30 to -10 days from solstice (DFS).

3.2.3 Results

Figure 3.2 shows the timing of the NH and SH PMC season onset vs. years. The dotted lines indicate years prior to 1984. Seasons between 1979 and 1983 were excluded from the analysis due to very low overall PMC frequencies in these years, the reason for which is unclear.

In these years large uncertainties in the definition of the season onset are caused by the season onset threshold of 1.5% being a significant fraction of the maximum frequency. The PMC seasons 1979 to 1983 coincide with solar maximum conditions that cause higher mesospheric temperatures and lower water vapor concentrations and therefore fewer and dimmer clouds. However, the 1981 solar maximum was comparable to the following solar maximum, during which overall frequencies were twice as high. Solar maximum conditions in addition to the long-term increase in the frequency of PMCs noted by DeLand *et al.* [2003] and Shettle *et al.* [2009], could contribute to lowest frequencies being associated with the earliest dates. Despite the exclusions, 28 continuous years spanning more than two solar cycles are covered in both hemispheres. While the NH and SH PMC seasons on average start at the same time (NH: DFS 15 ± 6 , SH: DFS -12 ± 12), variability in the SH onset date is twice as high as in the NH. Gumbel and Karlsson [2011] found average PMC season onset dates in units of DFS of -26 ± 3 and -24 ± 9 in the NH and SH, respectively, using PMC data from the Optical Spectrograph and InfraRed Imaging System (OSIRIS) instrument between 2002 and 2011. The earlier OSIRIS onset date is because OSIRIS is much more sensitive than SBUV, since it measures limb scattered sunlight. The overall higher SBUV variability in the PMC onset date may be due to the longer period of PMC onset observations available from SBUV. Nevertheless, measurements from both OSIRIS and SBUV show that variability in the SH season onset is significantly higher than in the NH.

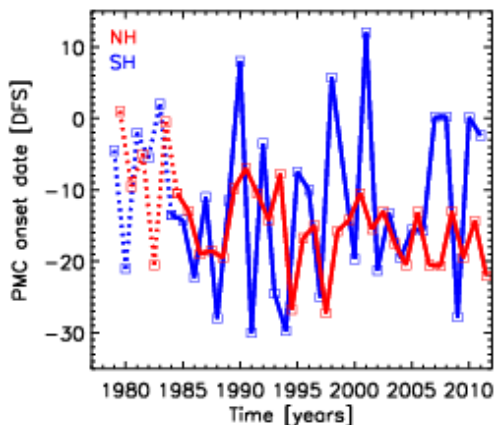


Figure 3.2: Time series of SBUV PMC season onset date in the NH (red) and SH (blue). Dotted lines indicate PMC onsets before 1984.

Figure 3.3 relates the timing of the SH PMC season onset to the timing of the SH lower stratospheric wind reversal from winter to summer conditions. Error bars on the PMC onset time series indicate the range of PMC onset dates from multiple SBUV instruments. Again, the dotted lines prior to 1984 indicate the problematic years described above. Year-to-year variations in the dates of the SH PMC season onset and wind reversal over the last 28 years are highly correlated, with a correlation coefficient $r = 0.85$. Including the PMC onset dates observed prior to 1984 decreases the correlation coefficient to 0.68. For reasons discussed above, the following results will not include the years prior to 1984. It could be argued that a small or absent ozone hole plays a role in these early years: the loss of ozone as observed from the late 1970's onward leads to a reduction in heating via absorption of solar radiation [Thompson and Solomon, 2002; Randel *et al.*, 2009]. A colder stratospheric polar vortex may be prolonged into austral summer, which in turn may lead to a later reversal from winter to summer conditions in the Antarctic polar upper atmosphere [Smith *et al.*, 2010, Lossow *et al.*, 2012]. Therefore it could be argued that the absence of the ozone hole in these early years could lead to earlier wind reversal dates in the SH stratosphere prior to 1984, and therefore cause a de-coupling of stratospheric wind and

PMC onset. That is, if the wind reversal occurred long before summertime conditions were setting up in the mesosphere, one might not expect it to influence PMCs. However, Figure 3.3 shows that the SH stratospheric wind reversal dates were not unusually early between 1979 and 1983. Therefore we exclude this possibility.

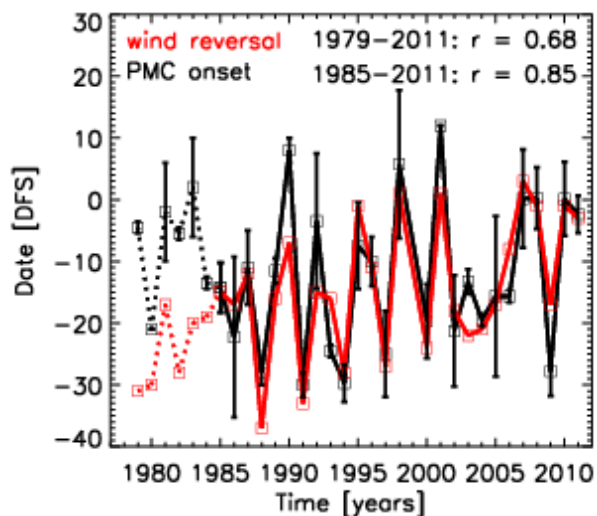


Figure 3.3: Time series of average SH PMC season onset dates as observed by SBUV (black) and date of SH stratospheric zonal mean zonal wind (ERA40 and MetO combined) reversal from winter to summer conditions at 50 hPa and 65°S latitude (red). Dotted lines indicate PMC onsets before 1984. Error bars show the range of values from multiple SBUV instruments.

For a more quantitative comparison, Figure 3.4 shows a linear fit of the PMC season onset to the stratospheric wind reversal. The linear fit to the data (red line) is in very good agreement with the black line, which denotes perfect agreement. The slope of the fit is 0.95 ± 0.12 , suggesting that the stratospheric wind reversal is indeed linearly related to the PMC season onset. That the fit is displaced above the one-to-one line indicates that the PMC onset date as observed by SBUV is delayed by about 1-2 days relative to the timing of the stratospheric wind reversal as defined here. This delay would likely be shorter or reversed for more sensitive instruments, and of course depends on the exact definition of the wind reversal.

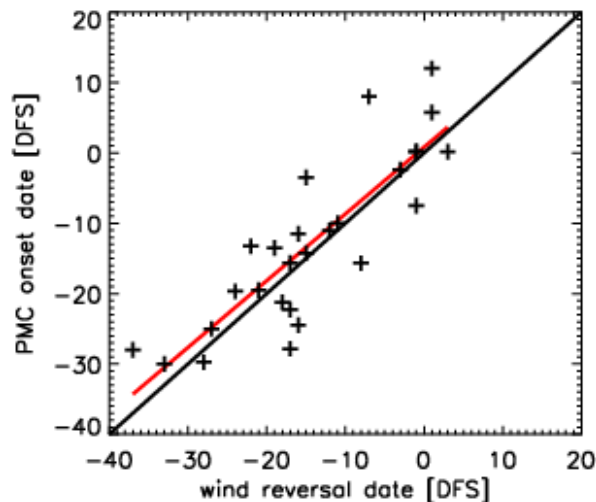


Figure 3.4: PMC onset date vs. wind reversal date (plus symbols) with a linear fit to the data (red) and one-to-one line for reference (black). Data before 1984 is excluded.

In the NH, the stratospheric wind reversal takes place about two months prior to the SBUV PMC season onset (not shown), so the wind reversal is not expected to control the date of the PMC season onset. This is supported by Gumbel and Karlsson [2011] who found no connection between the NH PMC onset and the timing of the NH wind reversal using the more sensitive Odin/OSIRIS instrument. We investigated whether the strength of the NH stratospheric zonal mean zonal wind at the time of the NH PMC season onset has any influence, but did not find any correlation (not shown).

Since PMCs are strongly influenced by solar activity [Thomas *et al.*, 1991, DeLand *et al.*, 2003], we also correlate Lyman- α with the PMC season onset date. Figure 3.5 shows SH (a) and NH (b) PMC season onset date expressed as DFS, and the median Lyman- α between DFS -30 and -10. In the NH there is a moderate correlation between solar signal and PMC season onset date, both with zero lag ($r = 0.60$) and a lag of one year ($r = 0.50$). Lags of more than one year decrease the NH correlation. A lag of one year is considered since several studies have found that PMC frequency correlates best with the solar cycle when a lag of 0.5 to 1.5 year is

considered [Kirkwood *et al.*, 2008; Thomas and Olivero, 2001; DeLand *et al.*, 2003]. In the SH, small correlation coefficients of 0.12 (0.14) at lag = 0 years (1 year) indicate very little correlation between the PMC season onset date and solar signal.

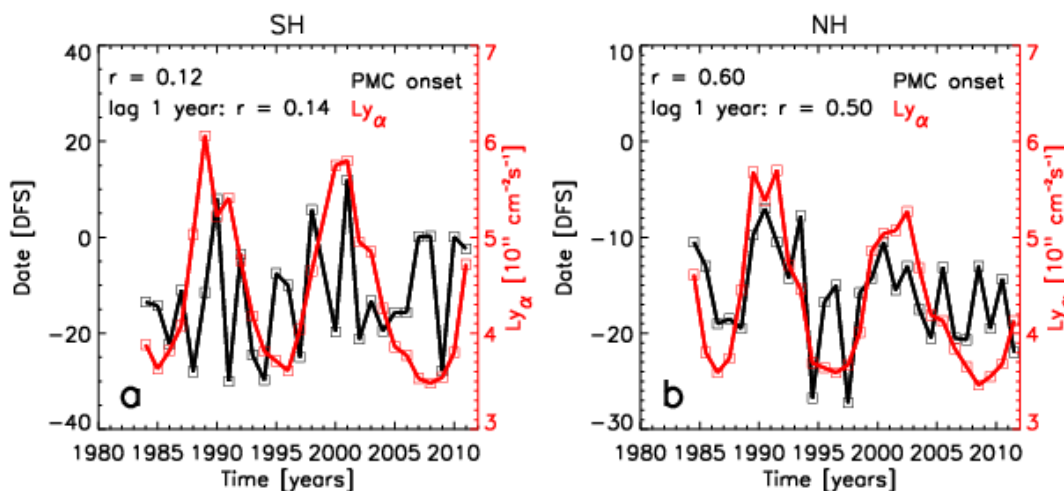


Figure 3.5: Time series of SBUV PMC onset date (black) and median of Lyman- α between DFS -30 and -10 (red) in the SH (a) and NH (b). Note the different y-axis scales for the PMC season start.

Although the SH correlation coefficient just described was small, visual inspection of Figure 3.5 gives the impression that even in the SH there is a low-frequency variation of the PMC season onset date that is correlated with the solar cycle, upon which is superimposed a higher frequency variation. Figure 3.6 compares the difference between SH PMC season onset date and the timing of the SH stratospheric wind reversal (i.e., the residual when the wind variation is subtracted from the observations) to the Lyman- α variations. This comparison reveals that the residual is correlated with the solar cycle, with a correlation coefficient of 0.61, similar to the solar cycle correlation in the NH. This indicates that variations in the SH PMC season onset date are dominated by the timing of the stratospheric wind reversal, with additional modulation from the solar cycle.

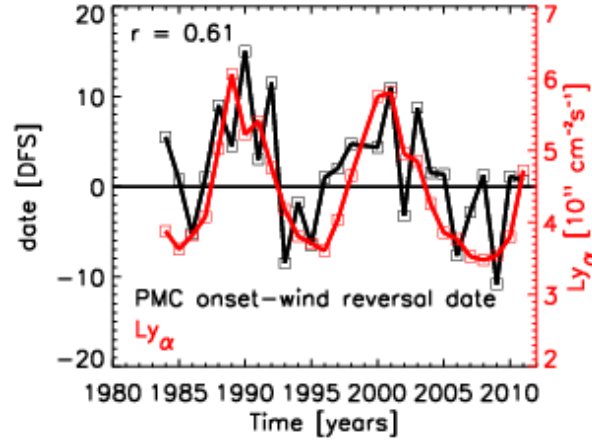


Figure 3.6: Difference between SH PMC onset date and SH wind reversal date (black) vs. Lyman- α (red).

In order to quantify the relative importance of these components, a multiple linear regression analysis was carried out. Since the stratospheric wind reversal and the Lyman- α signal are not correlated (not shown) and thus assumed to be independent, it can further be assumed that the PMC season onset date, D_{on} , can be expressed as a linear combination of the timing of the stratospheric wind reversal, W , and the solar cycle as represented by the Lyman- α flux, $Ly\alpha$:

$$D_{on} = a \cdot W + b \cdot Ly\alpha \quad (1)$$

The coefficients are $a=1.03 \pm 0.10$ days per day delay in the wind reversal, and $b=5.00 \pm 1.34$ days per unit of Lyman- α equal to $10^{11} \text{ cm}^{-2} \text{ s}^{-1}$. That is, for every day delay in the wind reversal, the season onset date is delayed by 1.03 days. For every increase in Lyman- α by $10^{11} \text{ cm}^{-2} \text{ s}^{-1}$, the season onset date is delayed by 5.0 days. As shown in Figure 3.6, Lyman- α changes by roughly twice this much over the solar cycle. Figure 3.7 compares the PMC onset date D_{on} calculated from Equation 1 to the PMC onset date inferred from SBUV observations. The correlation coefficient of 0.91 shows a small improvement over the correlation coefficient of 0.85 obtained by correlating the observed PMC onset date to the wind reversal date alone. Inter-

hemispheric coupling of the SH PMC onset with the NH stratospheric wind is not significant (not shown).

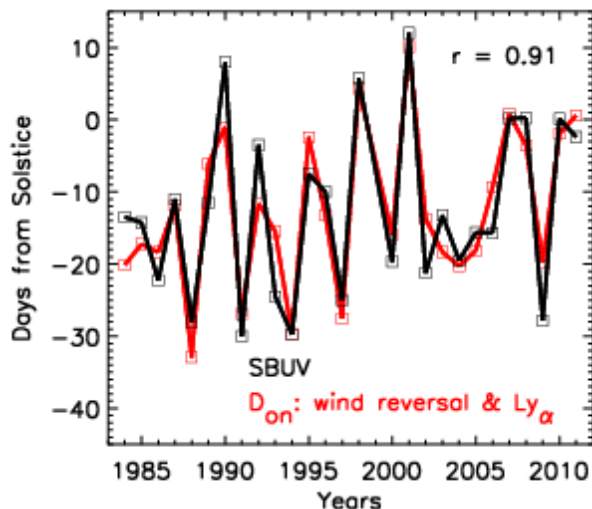


Figure 3.7: SBUV (black) and regressed (red) time series of SH PMC onset date using the SH stratospheric wind reversal date and solar Lyman- α as linear components.

In the NH, as in the SH, a multiple linear regression was also carried out. Recall (Figure 3.5) that we found a clear correlation between the observed NH PMC onset date and Lyman- α , but not between the NH PMC onset date and the same hemisphere stratospheric wind. We therefore investigated a possible connection between NH PMC onsets and stratospheric winds from the opposite hemisphere. This was accomplished by first performing a linear regression with Lyman- α as the only linear component in order to find the component of the total PMC onset variability that can be accounted for by Lyman- α . The residual of the NH PMC onset and the regression result was then correlated with the SH zonal mean zonal wind at various latitudes, altitudes, and times. The maximum correlation with the wind occurred 10 days before the NH PMC onset, at 60.0°S and 20 hPa (~26 km). Figure 3.8a shows the residual of the NH PMC onset and Lyman- α plotted vs. this zonal wind. The correlation coefficient of 0.77 supports the idea that interhemispheric coupling with the SH stratospheric winds plays a role in controlling NH

PMC onset dates. For the regression analysis the NH PMC season onset date, D_{on} , is therefore expressed as a linear combination of the SH stratospheric wind at the above mentioned space and time, W , and the solar cycle as represented by the Lyman- α flux, $Ly\alpha$:

$$D_{on} = c \cdot W + d \cdot Ly\alpha \quad (2)$$

The resulting coefficients are $c = 0.72 \pm 0.13$ days per m/s and $d = 3.51 \pm 0.79$ days per unit of Lyman- α equal to $10^{11} \text{ cm}^{-2}\text{s}^{-1}$. That is, for every increase in opposite hemisphere winter wind strength by 1 m/s, the NH season onset date is delayed by 0.72 days. For every increase in Lyman- α by $10^{11} \text{ cm}^{-2}\text{s}^{-1}$, the season onset date is delayed by 3.51 days. Figure 3.8b compares the PMC onset date D_{on} calculated from Equation 2 to the PMC onset date inferred from SBUV observations. The correlation coefficient of 0.85 shows a moderate improvement over the correlation coefficient of 0.60 obtained by correlating the observed PMC onset date to Lyman- α alone. Similar to the SH, in the NH Lyman- α explains much of the low-frequency variation of the PMC onset, whereas the opposite hemisphere winter wind strength explains much of the high-frequency variation. No correlation was found between the residual of observed and regressed NH PMC onset and quasi-biennial oscillation (QBO), North Atlantic Oscillation (NAO), Arctic Oscillation (AO), and El Niño Southern Oscillation (ENSO). Similarly, in the SH there were no statistically significant correlations between residual differences calculated by differencing the two curves in Figure 3.7 and the QBO, NAO, AO, or ENSO.

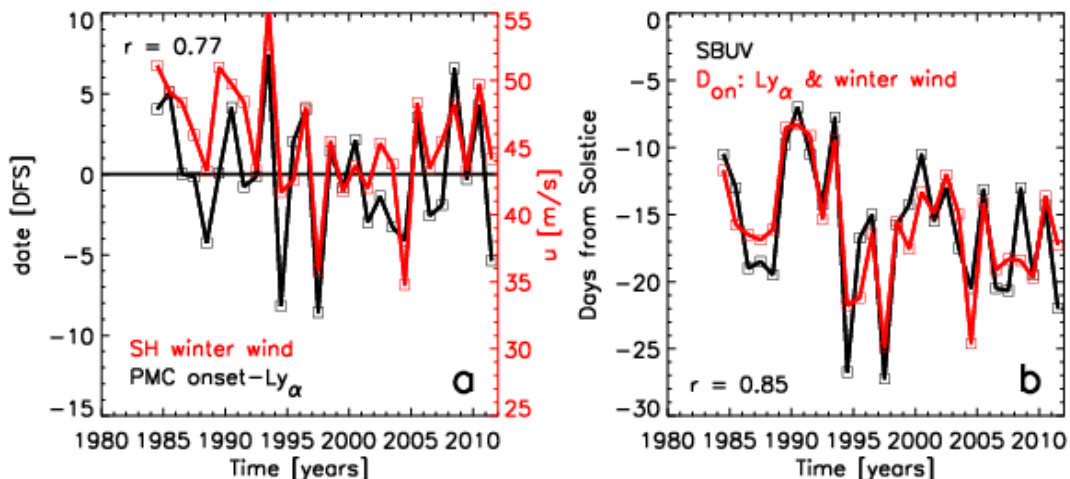


Figure 3.8: a: Difference between the NH PMC onset date and solar Lyman-alpha (black) vs. zonal mean zonal wind at 60.0°S, 20 hPa, 10 days before the onset date (red, right axis). b: SBUV (black) and regressed (red) time series of NH PMC onset date using solar Lyman- α and the wind plotted in the left panel as linear components.

Variability in the PMC season onset date may be increased beyond natural causes by several factors: space shuttle launches and time-varying instrumental effects like sampling of different scattering angles and local times. Observations at varying scattering angles lead to changing cloud detection sensitivity. This study focuses on polar latitudes, where SBUV observes the season onset at scattering angles between 100 and 120°. In this region the Mie scattering phase function is rather flat compared to forward scattering, and we find no clear dependence of PMC season onset date on scattering angle. Thus scattering angle variations may be able to influence the timing of the PMC season onset as determined from some instruments, but this is not a factor in the work presented here. Cloud frequencies are observed to vary in local time due to temperature oscillations caused by tides [von Zahn *et al.*, 1998; Chu *et al.*, 2003, 2006; Fiedler *et al.*, 2005; Stevens *et al.*, 2010]. For this study, the PMC onset for each year is calculated from at least two SBUV observations (ascending and descending node) of the PMC onset, and up to eight observations (both nodes from four instruments). Therefore, in most years the spread in local time during the PMC onset observed by SBUV is huge, usually covering five

to ten hours ranging from 1 AM to 10 PM in the SH, and from 3 AM to 7 PM in the NH. We found no clear connection between the timing of the cloud onset and local time, thus we do not believe that local time is a major driver of the season onset variability observed by SBUV.

Space shuttle launches inject huge amounts of water vapor into the lower mesosphere that have the potential to be transported into the polar regions and increase PMC frequency [Stevens *et al.*, 2002; 2003; 2005b]. We found that no space shuttles were launched up to five (six) days prior to any NH (SH) season observed by SBUV. Transport time of more than five or six days will cause the water vapor plume to diffuse considerably before it reaches the polar region. Another unknown is whether any SBUV instruments were observing at the right location and time to observe a potential increase in PMC frequency at all. Due to its low sensitivity and low horizontal resolution SBUV may not pick up the signal or may report it as a very faint one that does not trigger the season onset. Since the season onset detection algorithm explained in Section 3.2.2.3 rejects sporadic frequency increases, only water vapor plumes injected just before the natural season onset would have the potential to skew the onset determination to an earlier onset. There were only four years in both the NH and SH when shuttle launches occurred within eight days of the SBUV observed season onset; this would not significantly affect the correlations derived here. Thus it is unlikely that space shuttle launches have affected the PMC onsets observed by SBUV in any significant way.

3.2.4 Discussion and Conclusions

Using more than a quarter century of SBUV PMC observations and re-analysis wind data, this work builds on the study carried out by Karlsson *et al.* [2011] and Gumbel and Karlsson

[2011] who found that the timing of the SH stratospheric wind reversal from winter to summer conditions plays an important role in controlling the SH PMC onset date. This work extends these previous findings by showing a high correlation between the timing of the SH PMC season onset date and the timing of the SH stratospheric wind reversal from winter to summer conditions for observations from 1984 to 2011. The mechanism for this phenomenon was summarized by Karlsson *et al.* [2011]: an early reversal from winter eastward to summer westward winds causes an early onset of a net eastward GW drag that leads to an early deceleration of the mesospheric mean zonal flow and thus to equatorward meridional drift, mesospheric upwelling and adiabatic cooling. This early onset of cold temperatures then allows early formation of PMCs.

Beyond showing that the mechanisms described by Karlsson *et al.* [2011] and Gumbel and Karlsson [2011] hold for PMC seasons back to 1984, this work also determines the role of the solar cycle in the SH and NH PMC season onset, and investigates other possible controlling factors like inter-hemispheric coupling. The solar signal is expected to have an influence on PMCs because photolysis of upper mesospheric water vapor is modulated by the changing solar Lyman- α (121.6 nm) flux, and mesospheric temperatures are modulated by the changing solar UV heating rate between solar minimum and maximum conditions. Correlation of the SH season onset date and the solar cycle did not immediately reveal any connection. However, multiple linear regression of the PMC season onset date to stratospheric wind reversal and Lyman- α showed that the SH PMC onset is controlled primarily by the SH stratospheric wind reversal and secondarily by the solar cycle. The multiple linear regression coefficients obtained from equation 1 indicate that a one-day change in the timing of the stratospheric wind reversal from a winter to summer state results in a one-day change in the SH PMC onset date. The wind reversal date from

1984- to 2011 ranges from around -37 to $+3$ days from solstice (see Figure 3.3), for a total range of 40 days. Thus, in the absence of other effects, variations in the same hemisphere stratospheric wind reversal would cause the latest PMC season onset to be delayed by about 40 days from the earliest PMC season onset for the years analyzed here. Likewise, a change in Lyman- α of 10^{11} $\text{cm}^{-2}\text{s}^{-1}$ results in a change in the PMC onset date by 5.00 ± 1.34 days. Such a change in Lyman- α corresponds to roughly half the solar cycle, which suggests that if this were the only relevant mechanism, the SH PMC onset date would be about ten days later at solar maximum than at solar minimum. Since the solar cycle and wind reversal do not vary synchronously, the actual range of observed PMC onset dates is ~ 42 days, or slightly smaller than the sum of the two effects.

The NH stratospheric mean zonal wind reversal from winter to summer conditions takes place about two months earlier than the onset of the PMC season, and thus has no influence. This is due to higher PW activity in the NH that leads to an earlier breakup of the polar vortex and therefore earlier wind reversal than in the SH. The wind reversal causes the mesospheric temperature to drop (not shown), but these temperatures are not low enough yet for PMCs to form until one to two months later when the temperature drops below 140 to 150K. In addition, the mean zonal stratospheric wind speed at the time of the PMC onset does not correlate with the PMC season onset either (not shown). The solar signal shows a moderate correlation with the NH PMC season onset date, with a maximum correlation coefficient of 0.60, which was obtained without a lag. Multiple linear regression coefficients obtained from equation 2 indicate that a change in Lyman- α of 10^{11} $\text{cm}^{-2}\text{s}^{-1}$ results in a change in the PMC onset date by 3.51 ± 0.79 days. It suggests that the NH PMC onset date should be delayed by about seven days at solar maximum compared to solar minimum. In the NH, inter-hemispheric coupling of the opposite

hemisphere stratospheric winds plays a slightly bigger role in controlling the PMC onset dates than the solar cycle: A one m/s change in the zonal mean zonal wind at 60.0°S, 20 hPa (~26 km) and ten days before the NH PMC onset results in a change in the NH PMC onset date of 0.72 ± 0.13 days. Relative to the observed variations in the wind this means that the NH PMC onset should be delayed by about fifteen days at maximum wind speed compared to minimum wind speed. In neither hemisphere is there a correlation between the QBO, NAO, AO, or ENSO with either the PMC onset date or with the difference between PMC onset dates that were observed and calculated through linear regression.

Other possible causes of PMC onset variability such as instrument sampling and space shuttle effects were discussed. We found that neither varying scattering angles nor local times were major drivers of the PMC onset as observed by SBUV. While space shuttle launches may have an effect on PMC occurrence frequency as observed by SBUV, it is unlikely that they have affected the PMC onsets observed by SBUV in any significant way.

In summary we conclude that PW effects on stratospheric winds and consequent GW filtering trigger changes in mesospheric circulation that significantly affect the PMC season onsets in both hemispheres. The SH PMC season onset is controlled primarily by timing of the SH stratospheric wind reversal from its winter to summer state, with a smaller but still important contribution from the solar cycle; inter-hemispheric coupling appears to have a minimal effect. The strong dependence of the SH PMC onset date on the timing of the stratospheric wind reversal could have implications for long-term trends, since any trend in the stratospheric wind reversal will also affect the PMC onset [see, e.g., Smith *et al.*, 2010; Lossow *et al.*, 2012]. The NH PMC season onset is controlled primarily by changes in the opposite hemisphere stratospheric wind, but with a large contribution from the solar cycle. It is possible that the 2-day

and 5-day waves have a minor effect on the PMC onset dates and could explain some of the so far unexplained variability, especially in the NH. Neither the timing of the NH stratospheric wind reversal nor the NH stratospheric wind speed at the time of the NH PMC onset have any influence on the NH season onset.

Acknowledgements

The SBUV/2 data were obtained from NOAA/NESDIS with support from the NOAA Climate and Global Change Atmospheric Chemistry Element. Funding for SB, CER, GET, and VLH was provided by the NASA Small Explorer program under Contract NAS5-03132. SB was also supported by the NSF CEDAR program under grant AGS 0737705. MTD was partially supported by the NASA Geospace Science program through Grant NNH09CF72C. EPS was partially supported by the NASA Earth Science program through Grant NNH08CD48C. We thank ECMWF for producing the ERA-40 reanalysis and the National Center for Atmospheric Research for distributing the reanalysis data. We thank colleagues at the United Kingdom Meteorological Office for producing the MetO analyses and the Distributed Active Archive Center at the Goddard Space Flight Center and the British Atmospheric Data Centre for distributing the MetO data. Lyman- α data were obtained from <http://lasp.colorado.edu/lisird/>.

4 Preliminary results: The PMC onset as observed by SD-WACCM

This chapter describes a science investigation in its early stages, which builds on the work described above. The goal is to evaluate a state-of-the-art, global chemistry climate model for addressing the effects of teleconnection processes on PMCs. Although preliminary, the work is described here as an introduction to future studies that could be performed to further enhance our understanding of long-term changes in PMCs. An introduction to the investigation is described in Section 4.1. Section 4.2 contains a brief description of the model as well as a comparison of simulated mesospheric zonal mean temperature to SOFIE data and simulated stratospheric zonal mean zonal wind to Met Office (MetO) data. In Section 4.3 preliminary results are presented, and Section 4.4 describes plans for future work.

4.1 Introduction

This preliminary study uses the National Center for Atmospheric Research (NCAR) Community Earth System Model (CESM) version 1.0.3 with the Whole Atmosphere Community Climate Model version 4 (WACCM4) component set in order to gauge its potential for simulating the effects of intra-hemispheric teleconnections on PMCs, as described in Section 1.3.1 and by Benze *et al.* [2012] or in Chapter 3. Smith *et al.* [2010] describe WACCM simulations of the response of the mesospheric circulation and temperature to variations in the Antarctic ozone hole, and Benze *et al.* [2012] describe a strong correlation of SH PMC onset dates as observed by SBUV and the timing of the shift from winter to summer zonal wind flow in the SH stratosphere. The mesosphere responds to variations in the ozone hole via the

mechanism described above, wherein changes in the stratospheric wind affect GW filtering. Thus, as Smith *et al.* [2010] state, their results should have implications for PMCs. The goal of this study is to assess this expectation by comparing model simulations directly to satellite observations of PMCs.

WACCM is a global chemistry climate model that extends the CESM simulations into the lower thermosphere near 145 km. The WACCM4 component uses a finite-volume dynamical core [Lin, 2004], and a hybrid vertical scale with 66 levels that are isobaric above ~100 hPa. The vertical resolution increases from about 1.1 km in the troposphere to 1.75 km around 50 km to 3.5 km above ~65 km [Garcia *et al.*, 2007]. The horizontal resolution for the run used here is 1.9 degrees latitude by 2.5 degrees longitude. The chemistry module of WACCM4 is based on the Model for Ozone and Related Chemical Tracers version 3 (MOZART3), which is described in Kinnison *et al.* [2007]. The gravity wave parameterization employed in WACCM4 is described by Richter *et al.* [2010]. Briefly, orographic gravity waves are parameterized based on McFarlane [1987]; the parameterization includes the efficiency with which they are launched. Non-orographic gravity waves are parameterized according to the formulation of Lindzen [1981]; they are launched through either a convective or frontal source parameterization [Richter *et al.*, 2010].

For the comparison to be meaningful, it is important that the model correctly simulates day-to-day variability in the stratospheric wind. Therefore, the specified dynamics version of WACCM, SD-WACCM, is used. In this version the model meteorology is constrained by observations, rather than computed interactively as in the free-running (interactive) version. SD-WACCM does not yet simulate PMCs, neither parameterized nor resolved. Therefore PMC onset dates are inferred from simulated temperatures in the polar summer upper mesosphere. These

inferred PMC onset dates are then compared to the wind reversal dates, which are defined the same way as described by Benze *et al.* [2012]. Using only temperature for defining the PMC onset date is a reasonable approach for this preliminary study since PMC formation depends on the saturation ratio, which depends exponentially on temperature and only linearly on water vapor abundance [Eckermann *et al.*, 2009 and references therein]. Future work will consider the saturation ratio or ice water content derived from SD-WACCM, rather than temperature only for inferring PMC onset dates from the model.

4.2 SD-WACCM

SD-WACCM is a modified version of WACCM in which the meteorology is constrained by observations up to the stratopause. The model used here is nudged every 30 minutes with horizontal winds, temperatures, and surface pressure from the Goddard Earth Observing System 5 (GEOS5) analysis [Reinecker *et al.*, 2008]. This reanalysis product has a 6-hour time resolution, which is interpolated to the required 30-minute time resolution. The nudging coefficient is 0.01, which means that horizontal winds, temperatures, and surface pressure are calculated from a linear combination of 1% from the re-analysis product and 99% from the model. The model is nudged in this way below 50 km, with a linear transition of 1% to zero from 50 to 60 km, while above 60 km the model is fully interactive. In addition to the described nudging, the model is forced with GEOS-5 surface wind stress and sensible as well as latent surface heat flux.

Figure 4.1 shows the stratospheric (100 – 1 hPa) zonal mean zonal wind at $75^{\circ}\text{S} \pm 2.5^{\circ}$ at the end of November and December 2008 from SD-WACCM and the Met Office (MetO). Since

in the stratosphere the model is nudged by GEOS-5 as described above, this figure basically shows a comparison of GEOS-5 and MetO winds. The modeled zonal mean wind resembles observations very well in the stratosphere; below ~ 1 hPa the wind continually decreases from the winter eastward to the summer westward wind velocities. Since the zonal wind filters vertically propagating GWs and thereby changes the residual circulation, this results in increased upwelling and equatorward flow (not shown). As a result, upper mesospheric temperatures decrease due to adiabatic cooling. The mechanism for this intra-hemispheric coupling is described in more detail in Section 1.3.1 and Chapter 3.

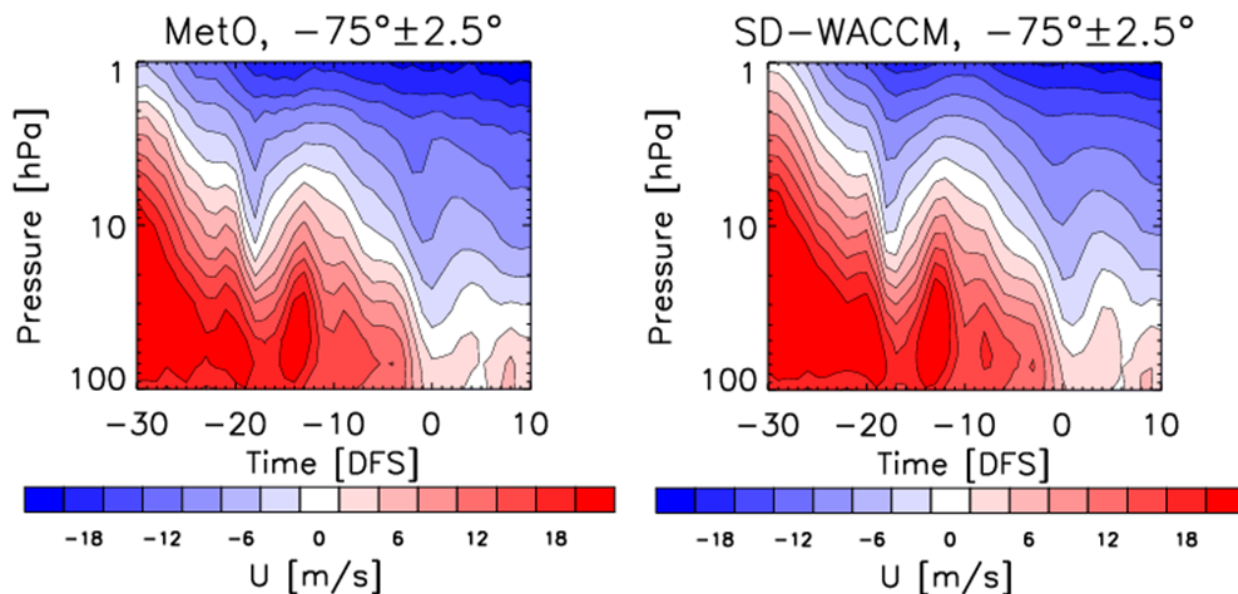


Figure 4.1: MetO (left) and SD-WACCM (right) stratospheric zonal mean zonal wind at $75^{\circ}\text{S} \pm 2.5^{\circ}$ in the SH in 2008.

As shown in Figure 4.2, the modeled zonal mean mesospheric ($1 - 10^{-4}$ hPa) temperatures at $65^{\circ}\text{-}70^{\circ}\text{S}$ during the same time are significantly different from SOFIE version 1.2 temperatures, especially in the upper mesosphere. SOFIE v1.2 temperatures are in agreement to within reported systematic uncertainties with several other datasets (e.g., SABER v2.00) for all altitudes up to 88 km, but have a warm bias between 88 and 95 km [Stevens *et al.*, 2012,

submitted to JGR]. This warm bias is about twice as large in the Antarctic summer (20-30 K) as in the Arctic summer (10-15 K). Even taking into account this SOFIE warm bias above 88 km, Figure 4.2 shows that the simulated mesopause is too cold; in addition, the mesopause altitude is too low, especially in early summer.

A possible reason for the cold, low mesopause is that GWs in SD-WACCM break too low, as already suggested by Bardeen *et al.* [2010] using WACCM with sectional microphysics from the Community Aerosol and Radiation Model for Atmospheres (CARMA) model. They find that the WACCM default GW parameterization is a compromise between generating a good climatology in both the stratosphere and the mesosphere. This results, however, in a mesopause that is too low and too cold. The same is likely true for the version of SD-WACCM used in this study, even though there are two major differences from the model that Bardeen *et al.* [2010] used in addition to the sectional microphysics: 1) the GW parameterization scheme has been updated to a frontal system and convective GW source parameterization [Richter *et al.*, 2010] instead of the previously used arbitrarily specified GW source function, and 2) a parameterization to estimate mountain stress due to unresolved orography was added. Richter *et al.* [2010] find that the two new parameterizations improve the simulated variability of the NH stratosphere, which now exhibits a more realistic frequency of stratospheric sudden warmings. Richter *et al.* [2010] compare the simulated summer mesopause temperatures to SABER (v1.06) and find that SH January mesopause temperatures are ~ 8 K too warm with the new GW scheme, whereas in the NH, July mesopause temperatures are close to SABER observations. Figure 4.2, comparing SD-WACCM with SOFIE v1.2 temperatures, shows an underestimate of simulated mesopause temperature and altitude that seems to contradict the findings by Richter *et al.* [2010]. SOFIE v1.2 temperature is found to be in good agreement with SABER v2.00 temperatures up to

88 km as shown by Stevens *et al.* [2012, submitted to JGR]. Thus, one possible reason for the apparent discrepancy between the conclusions drawn by Richter *et al.* [2010] and this study may be the different SABER data version used by Richter *et al.* [2010]. Both SABER v1.07 and SABER v2.00 include improvements to the performance in the summer polar mesopause region compared to v1.06. Thus, model-SABER comparisons by Richter *et al.* [2010] using SABER v1.06 need to be updated for SABER v2.00.

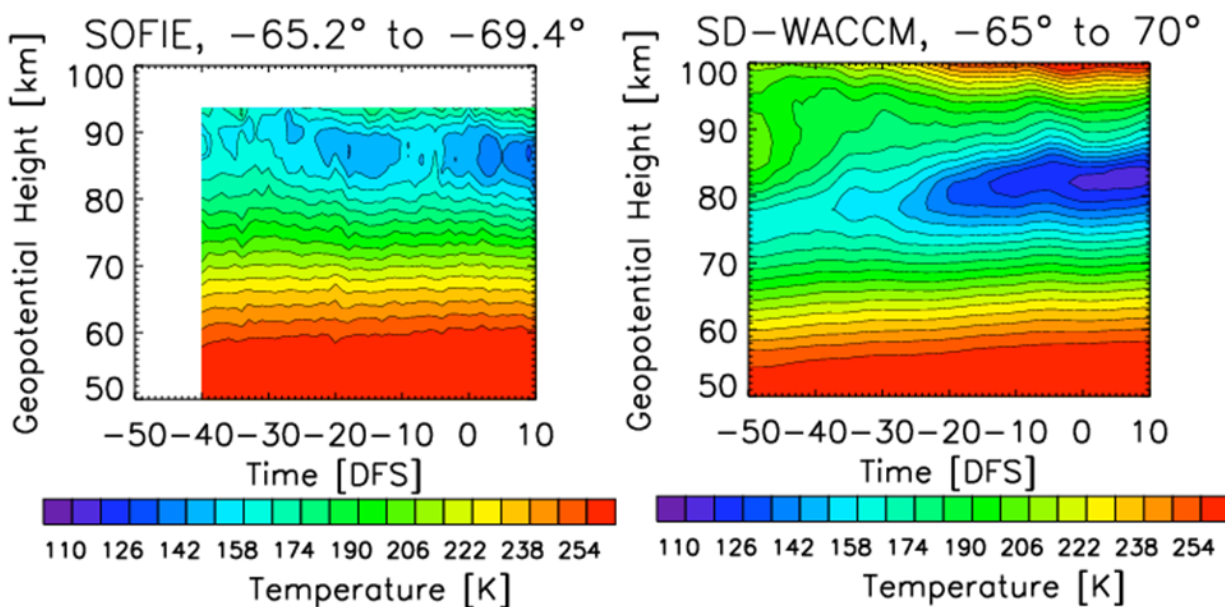


Figure 4.2: SOFIE (left) and SD-WACCM (right) mesospheric zonal mean temperature at 65° - 70° S in the SH during 2008.

4.3 Preliminary results

As described above, the PMC season onset dates are preliminarily inferred from the simulated polar summer temperature in the upper mesosphere. This inferred PMC season onset date is defined as the date on which the zonal mean 5-day averaged simulated temperature at 85 km between 75° and 85° S decreases below 125 K. This criterion is chosen so that simulated

PMC onset dates are on average the same as SBUV onset dates which were investigated by Benze *et al.* [2012], also described in Chapter 3. The day of the wind reversal is defined as the final decrease of the 5-day running average zonal mean zonal wind at 50 hPa (~ 20 km) and 65°S below 10 m/s, in agreement with the criterion first proposed by Waugh *et al.* [1999] and used by Langematz and Kunze [2006; 2008] and Benze *et al.* [2012] (see Chapter 3).

To illustrate these criteria, Figure 4.3 shows the modeled 5-day running average zonal mean zonal wind at 50 hPa and 65°S and the 5-day running average zonal mean temperature at 85 km and $75^\circ\text{--}85^\circ\text{S}$ for the SH 2008 season. In this season, the inferred PMC onset took place 12 days before the wind reversal, an issue that is discussed more below.

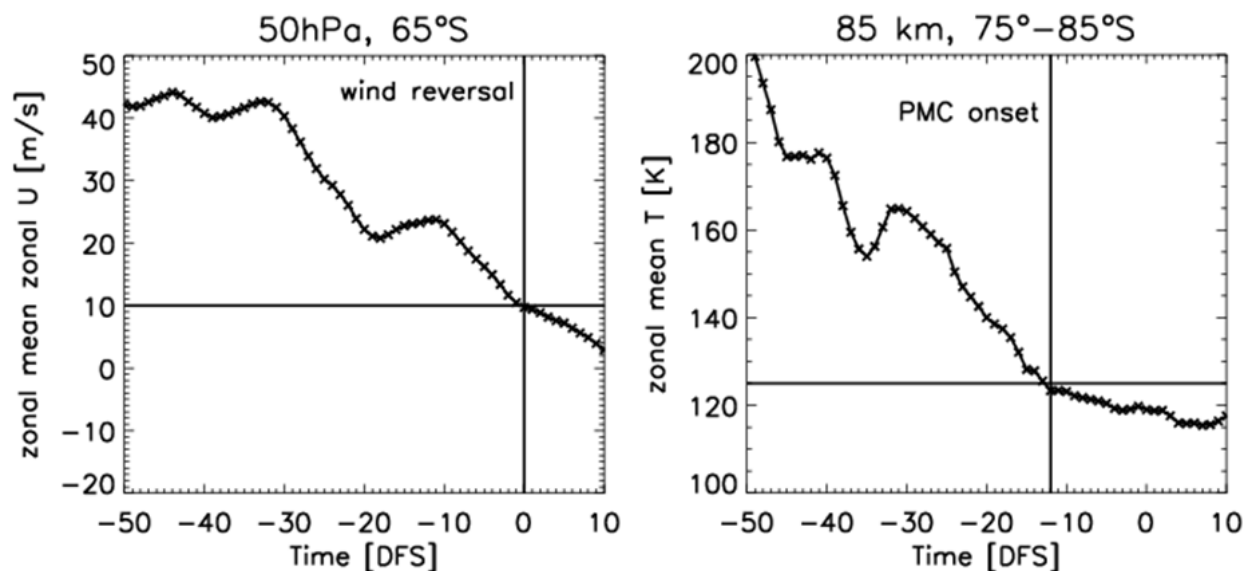


Figure 4.3: Evolution of SD-WACCM wind and temperature in SH 2008 summer. Left: Five-day running average zonal mean zonal wind at 50 hPa and 65°S , right: Five-day running average zonal mean temperature at 85 km and $75^\circ\text{--}85^\circ\text{S}$. Horizontal lines depict the cut-off values of wind and temperature that define the wind reversal and PMC onset dates (vertical lines).

The simulated PMC onset dates and stratospheric wind reversal dates as defined above are shown in Figure 4.4 for all SH seasons between 2001 and 2010. Additionally, the PMC onset dates as observed by SBUV are shown. Error bars on the SBUV PMC onset data indicate the

range of onset dates inferred from measurements from multiple SBUV instruments on different satellites and from observations in the ascending and descending node. As expected from Benze *et al.* [2012], the PMC onset dates as observed by SBUV correlate well with the simulated wind reversal dates. The pure temperature criterion results in simulated PMC onset dates that, on average, agree with the observed onset dates. The year-to-year variability, however, does not show much similarity. The very weak correlation of simulated PMC onset dates and simulated wind reversal dates ($r = 0.28$) is inconclusive regarding the intra-hemispheric coupling mechanism of stratospheric winds controlling the PMC onset.

On average, the simulated PMC onset takes place 3.2 ± 9.5 days earlier than the wind reversal, with the inferred PMC onset sometimes leading, sometimes following the wind reversal. This is not in agreement with the mechanism presented by Karlsson *et al.* [2011], Gumbel and Karlsson [2011] and Benze *et al.* [2012]. The most reasonable approach to addressing this issue is to choose a different criterion for defining the season onset. One option, for instance, is to define a saturation ratio threshold, as described in Section 4.1. Yet another approach is to calculate the ice water content (IWC), which is derived from both CIPS and SOFIE observations. One way to infer IWC in SD-WACCM is to vertically integrate ice mass density calculated by the “0D model” of Hervig *et al.* [2009d]. This model assumes that ice exists in bulk thermodynamic equilibrium in order to calculate ice mass density. Hervig *et al.* [2009d] showed that the 0D model can reproduce the average ice layer altitudes, ice frequency versus time and altitude, ice mass density versus time and altitude, and IWC as observed by SOFIE. Deriving IWC from SD-WACCM simulations will enable more direct comparisons between the model and observations, and will also allow consideration of different instrument sensitivities.

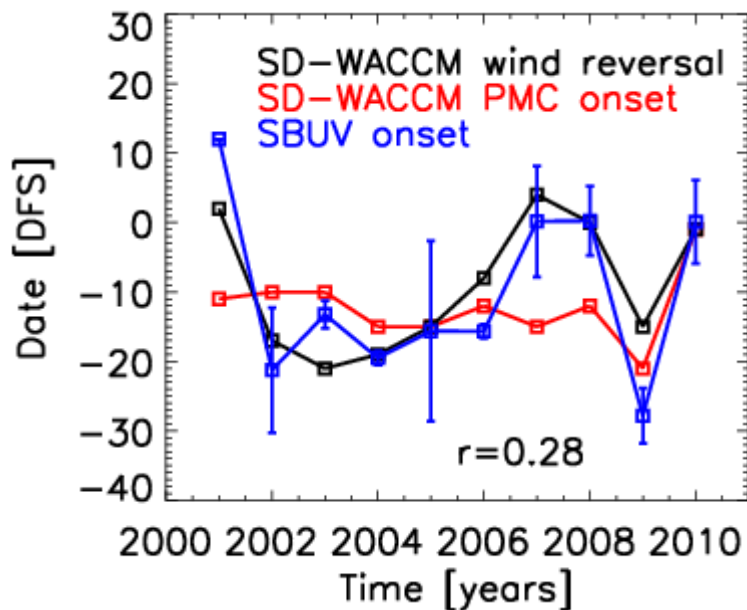


Figure 4.4: SD-WACCM PMC onset dates calculated from the model temperature at 85 km and 75°-85°S (red), wind reversal dates calculated from zonal mean zonal wind at 50 hPa and 65°S (black), and the PMC onset as observed by SBUV (blue). Error bars on the SBUV PMC onset data indicate the range of onset dates inferred from measurements from multiple SBUV instruments on different satellites and from observations in the ascending and descending node.

4.4 Summary and outlook

Although preliminary, the analysis presented above is promising, showing that simulated PMC onset dates are on average similar to the PMC onset dates as observed by SBUV. The results shown are not conclusive, however, because the simulated PMC onset takes place on average 3.2 ± 9.5 days before the wind reversal, sometimes leading, sometimes following it. This is not in agreement with the intra-hemispheric coupling mechanism of stratospheric winds controlling the PMC onset. Therefore, future work needs to address this discrepancy, which may be accomplished by a change in the criterion used for defining the PMC onset dates. Furthermore, the simulations should be extended to the entire SBUV record.

The 0D model presented by Hervig *et al.* [2009d] and briefly described in Section 4.3 enables calculation of ice mass density, which can be converted to IWC. Comparison to CIPS/SOFIE IWC allows for the adjustment of the model's PMC onset parameterization to CIPS/SOFIE PMC sensitivity. This comparison of simulated and observed IWC can of course be extended from the PMC onset date to relative variations during the PMC season.

Finally, in order to confirm that the reason for this coupling is the mechanism described above, the residual circulation and GW parameters need to be analyzed and correlated with the wind reversal dates. It is expected from the intra-hemispheric coupling mechanism that both the vertical and meridional residual circulation velocities should be correlated with the PMC onset dates and wind reversal dates: a later than usual wind reversal should cause a late increase in the eastward GW drag and hence a late increase in the vertical and meridional residual circulation velocities. This would lead to late adiabatic cooling, which would cause a delay in the onset of the PMC season, consistent with the expectations outlined in Smith *et al.* [2010].

5 Conclusions and future work

Benze *et al.* [2009; 2011] validate the AIM/CIPS instrument by comparing PMC occurrence frequency, cloud albedo and background albedo to SBUV observations. They find that frequency and cloud albedo are in excellent agreement. The background Rayleigh albedo, however, shows a still unresolved bias that depends on hemisphere. In addition, the CIPS v3.20 operational frequencies at more equatorward PMC latitudes on the descending node might have a small (~10%) low bias. Subsequent to the publication of Benze *et al.* [2011] the v4.20 operational CIPS retrieval version was introduced. It has a significantly improved background removal algorithm, and thus improved cloud detection statistics. Therefore, it would be useful to extend these validation efforts to v4.20 CIPS data. Additionally, Benze *et al.* [2009; 2011] use only a tiny fraction of the available CIPS data for validation, hence future validation efforts should include the CIPS data at all available SCAs and view angles, and possibly compare this data to lidars and other satellites, e.g., OMI, which uses smaller pixels than the SBUV instruments and has a wide cross-track viewing swath that provides full polar coverage up to 90° latitude every day in both hemispheres. The validation of CIPS data presented by Benze *et al.* [2009; 2011] is an important and necessary investigation that shows that CIPS data is valid for scientific use by the PMC community.

Benze *et al.* [2012] investigates causes of variability in the PMC onset dates in both hemispheres. Previous studies [Karlsson *et al.*, 2011; Gumbel and Karlsson, 2011] found that intra-hemispheric coupling is a controlling factor in the SH PMC onset, using three SH seasons of CIPS and SOFIE observations and nine SH seasons of OSIRIS observations, respectively. Benze *et al.* [2012] extend these studies and confirm the previous explanation by showing its

effect on historical data from 28 years of SBUV data: year-to-year variability in SH zonal mean stratospheric wind is highly correlated to the onset of SH PMC seasons. The NH PMC onset dates, however, are decoupled from the NH zonal mean stratospheric wind since the wind changes from winter-like to summer-like conditions two months prior to the onset of the PMC season, and therefore have no influence on it. Previous studies [Karlsson *et al.*, 2007; 2009a; 2009b] have also described that inter-hemispheric coupling influences intra-seasonal variability in PMC occurrence frequency and particle radius. Benze *et al.* [2012] extend these studies by investigating how PMC onset dates are controlled by inter-hemispheric coupling. The solar cycle effect on PMC albedo and frequency has long been known [e.g., Garcia 1989, Thomas *et al.*, 1991], but its effect on the PMC season onset has never been documented. Therefore, coupling of the solar cycle and the PMC onset dates is also quantified.

For the first time, all three effects, intra-, inter-hemispheric coupling, and the solar cycle, are combined in a multiple linear regression analysis and their relative importance in controlling NH and SH PMC onset dates is quantified. Benze *et al.* [2012] find that the SH PMC season onset is controlled primarily by the timing of the SH stratospheric wind reversal from its winter to summer state, with a smaller but still important contribution from the solar cycle. Since SH stratospheric winds have been shown to change due to changes in the Antarctic ozone hole, this coupling has implications for long-term trends in the PMC onset. Benze *et al.* [2012] further show that inter-hemispheric coupling triggered by winter stratospheric wind variations plays a big role in controlling the NH PMC season onset dates, with additional control by the solar cycle. The correlation of observed NH PMC onset dates and linearly regressed onset dates is slightly smaller than in the SH, suggesting unidentified processes that are more important in the NH than SH, for example 2-day or 5-day planetary waves. A future study could build on this result by

including these waves in the multiple linear regression analysis, and quantifying their impact on the NH PMC onset dates. More suggestions for future studies investigating PMC variability are summarized below. Benze *et al.* [2012] advance scientific knowledge by explaining most of the variability in the PMC season onset over the last 3 decades, both in the NH and SH. Even though the culminating Benze *et al.* [2012] study does not use AIM CIPS data, the results gained are nevertheless pivotal to accomplishing the overall AIM mission goal to “determine why NLCs form and *why they vary*”. In addition, the final objective of the AIM mission is to "provide the basis for study of long-term variability in the mesospheric climate and its relationship to global change". The investigation by Benze *et al.* [2012] goes a long way toward accomplishing this objective. That is, by extending previous studies based on AIM data to the longer term measurements of SBUV, Benze *et al.* [2012] have identified mechanisms that affect long-term variability in mesospheric climate. These mechanisms should therefore be investigated to determine their relationship to global change.

Preliminary results presented in Chapter 4 are promising, but inconclusive regarding intra-hemispheric coupling of SH stratospheric wind and SH PMC onset dates. More work is necessary to improve the PMC onset criterion in SD-WACCM and to confirm the intra-hemispheric coupling mechanism described in Section 1.3.1 and Chapter 3.

Some potential topics for future studies have been introduced above. This list summarizes future studies that would extend Benze *et al.* [2009; 2011; 2012] in more detail:

- The systematic difference in Rayleigh background albedo between CIPS and SBUV found by Benze *et al.* [2011], with CIPS albedo being lower in the NH and higher in the SH, is still not resolved.

- CIPS validation needs to be updated for the current CIPS version v4.20. Furthermore, since Benze *et al.* [2009; 2011] used only a small portion of the available CIPS data for validation, the comparison should be extended to all CIPS viewing angles. More CIPS validation should be carried out by comparison to ground based instruments such as lidar and other satellite instruments, e.g., OMI.
- A study that would directly add to Benze *et al.* [2012] is an investigation of the influence of 2-day and 5-day planetary waves that are generated in-situ in the mesosphere [e.g., Lossow *et al.*, 2012]. Inclusion of these waves is expected to improve the multiple linear regression results of PMC onset dates, especially in the NH.
- One could also extend Benze *et al.* [2012] by investigating the season end and latitudinal extent. Preliminary results by Cora Randall (personal communication) show that the timing of the PMC season end resembles the PMC season onset, which suggests similar mechanisms controlling the PMC season end. Furthermore, Nielsen *et al.* [2010] find that in the NH the 5-day wave plays an important role controlling occurrence frequencies the end of the PMC season, complementing the previous future work possibility.
- Bodil Karlsson finds that the SH PMC onset as observed by OSIRIS is de-coupled from the SH stratospheric wind reversal when the wind reverses very early (personal communication). This is in direct contradiction to Benze *et al.* [2012] who find a very strong coupling between SBUV SH PMC onset dates and SH stratospheric winds, independent of the timing of the wind reversal. One difference between OSIRIS and SBUV is the PMC detection sensitivity, which is much greater for OSIRIS than for SBUV. Doing a sensitivity study of the OSIRIS detection threshold on the intra-

hemispheric coupling would clarify whether the presence of coupling depends on the cloud brightness or not.

- Karlsson *et al.* [2007; 2009b] show how interannual PMC variability, in both the NH and SH, can be forced by planetary wave activity in the winter stratosphere. On the other hand, Benze *et al.* [2012] show that the SH PMC onset is controlled by same-hemispheric winds and that the NH PMC onset by opposite-hemispheric winds. This leads toward the question whether interannual PMC variability is controlled by *both* same- and opposite-hemispheric winds. Hence this analysis would quantify the effects of both intra- and inter-hemispheric coupling on PMC variability from season to season as well as from day to day. The analysis would probably be complicated by a lag between PMC variations and the winter hemisphere that Karlsson *et al.* [2009b] suggested to be dependent on the PMC altitude, such that the lag increases with decreasing PMC altitude.
- An analysis gauging the potential of SD-WACCM for simulating intra-hemispheric teleconnections between SH stratospheric winds and the SH PMC season onset show promising preliminary results, which are however not yet conclusive. Therefore future work addressing PMC onset parameterization insufficiencies are suggested in Section 4.4.

6 Bibliography

- Achatz, U., N. Grieger, and H. Schmidt (2008), Mechanisms controlling the diurnal solar tide: Analysis using a GCM and a linear model, *J. Geophys. Res.*, 113, A08303, doi:10.1029/2007JA012967.
- Alpers, M., M. Gerding, J. Höffner, and U. von Zahn (2000), NLC particle properties from a five-color lidar observation at 54°N, *J. Geophys. Res.*, 105, 12235-12240, doi:10.1029/2000JD900132.
- Andrews, D. G., J. R. Holton, and C. B. Leovy (1987), Middle Atmosphere Dynamics, *Academic Press*, San Diego.
- Backhouse, T. W. (1885), The luminous cirrus clouds of June and July, *Meteorol. Mag.*, 20, 133.
- Bailey, S. M., A. W. Merkel, G. E. Thomas, and J. N. Carstens (2005), Observations of polar mesospheric clouds by the student nitric oxide explorer, *J. Geophys. Res.*, 110, D13203, doi:10.1029/2004JD005422.
- Bailey, S. M., A. W. Merkel, G. E. Thomas, and D. W. Rusch (2007), Hemispheric differences in polar mesospheric cloud morphology observed by the student nitric oxide explorer, *J. Atmos. Sol.-Terr. Phys.*, 69, 1407-1418, doi:10.1016/j.jastp.2007.02.008.
- Bailey, S. M., G. E. Thomas, D. W. Rusch, A. W. Merkel, C. D. Jeppesen, J. N. Carstens, C. E. Randall, W. E. McClintock, and J. M. Russell III (2009), Phase functions of polar mesospheric cloud ice as observed by the CIPS instrument on the AIM satellite, *J. Atmos. Sol.-Terr. Phys.*, 71, 373-380, doi:10.1016/j.jastp.2008.09.039.
- Balsley, B. B., R. F. Woodman, M. Sarango, J. Urbina, R. Rodriguez, E. Ragaini, and J. Carey (1993), Southern-Hemisphere PMSE - Where are they, *Geophys. Res. Lett.*, 20(18), 1983-1985, doi:10.1029/93GL02244.
- Balsley, B. B., R. F. Woodman, M. Sarango, R. Rodriguez, J. Urbina, E. Ragaini, J. Carey, M. Huaman, and A. Giraldez (1995), On the Lack of Southern-Hemisphere Polar Mesosphere Summer Echoes, *J. Geophys. Res.*, 100(D6), 11685-11693, doi:10.1029/95JD00510.
- Bardeen, C. G., O. B. Toon, E. J. Jensen, D. R. Marsh, and V. L. Harvey (2008), Numerical Simulations of the Three-Dimensional Distribution of Meteoric Dust in the Mesosphere and Upper Stratosphere, *J. Geophys. Res.*, 113, D17202, 10.1029/2007JD009515.
- Bardeen, C. G., O. B. Toon, E. J. Jensen, M. E. Hervig, C. E. Randall, S. Benze, D. R. Marsh, and A. W. Merkel (2010), Numerical simulations of the three-dimensional distribution of polar mesospheric clouds and comparisons with Cloud Imaging and Particle Size (CIPS) experiment and the Solar Occultation For Ice Experiment (SOFIE) observations, *J. Geophys. Res.*, 115, doi:10.1029/2009JD012451.

- Baumgarten, G., K. H. Fricke, and G. T. von Cossart (2002), Investigation of the shape of noctilucent cloud particles by polarization lidar technique, *Geophys. Res. Lett.*, 29, doi:10.1029/2001GL013877.
- Baumgarten, G., J. Fiedler, and G. von Cossart (2007), The size of noctilucent cloud particles above ALOMAR (69N, 16E): Optical modeling and method description, *Adv. Space Res.*, 40, 772-784, doi:10.1016/j.asr.2007.01.018.
- Baumgarten, G., J. Fiedler, F.-J. Lübken, and G. von Cossart (2008), Particle properties and water content of noctilucent clouds and their interannual variation, *J. Geophys. Res.*, 113, doi:10.1029/2007JD008884.
- Baumgarten, G., J. Fiedler, and M. Rapp (2010), On microphysical processes of noctilucent clouds (NLC): observations and modeling of mean and width of the particle size-distribution, *Atmos. Chem. Phys.*, 10, doi:10.5194/acp-10-6661-2010.
- Becker, E. and G. Schmitz (2003), Climatological effects of orography and land-sea heating contrasts on the gravity wave-driven circulation of the mesosphere, *J. Atmos. Sci.*, 60, 103–118, doi:10.1175/1520-0469(2003)0600103:CEOOAL>2.0.CO;2.
- Becker, E., A. Müllemann, F. J. Lübken, H. Körnich, P. Hoffmann, and M. Rapp (2004), High Rossby-wave activity in austral winter 2002: Modulation of the general circulation of the MLT during the MaCWAVE/MIDAS northern summer program, *Geophys. Res. Lett.*, 31, L24S03, doi:10.1029/2004GL019615.
- Beig, G., et al. (2003), Review of mesospheric temperature trends, *Rev. Geophys.*, 41, 10.1029/2002RG000121.
- Benze, S., C. E. Randall, M. T. DeLand, G. E. Thomas, D. W. Rusch, S. M. Bailey, J. M. Russell III, W. E. McClintock, A. W. Merkel, and C. D. Jeppesen (2009), Comparison of polar mesospheric cloud measurements from the cloud imaging and particle size experiment and the solar backscatter ultraviolet instrument in 2007, *J. Atmos. Sol.-Terr. Phys.*, 71, 365–372, doi:10.1016/j.jastp.2008.07.014.
- Benze, S., C. E. Randall, M. T. DeLand, G. E. Thomas, S. M. Bailey, J. M. Russell III, and A. W. Merkel (2011), Evaluation of AIM CIPS measurements of Polar Mesospheric Clouds by comparison with SBUV data, *J. Atmos. Sol.-Terr. Phys.*, 73, doi:10.1016/j.jastp.2011.02.003.
- Benze, S., C. E. Randall, B. Karlsson, V. L. Harvey, M. T. DeLand, G. E. Thomas, and E. P. Shettle (2012), On the onset of polar mesospheric cloud seasons as observed by SBUV, *J. Geophys. Res.*, 117, D07104, doi:10.1029/2011JD017350.
- Brasseur, G., and S. Solomon (2005), *Aeronomy of the Middle Atmosphere - Chemistry and Physics of the Stratosphere and Mesosphere*, Springer, Dordrecht, Netherlands.

- Brewer, A. W. (1949), Evidence for a World Circulation Provided by the Measurements of Helium and Water Vapour Distribution in the Stratosphere, *Quart. J. Roy.*, 75, doi:10.1002/qj.49707532603.
- Carbary, J. F., G. J. Romick, D. Morrison, L. J. Paxton, and C. I. Meng (1999), Altitudes of polar mesospheric clouds observed by a middle ultraviolet imager, *J. Geophys. Res.*, 104, doi:10.1029/1999JA900088.
- Carbary, J. F., D. Morrison, and G. J. Romick (2003), Maps of polar mesospheric clouds, *J. Geophys. Res.*, 108, 8446, doi:10.1029/2002JD002255.
- Chamberlain, J. W., D. M. Hunten, and J. E. Mack (1958), Resonance Scattering by Atmospheric Sodium .4. Abundance of Sodium in Twilight, *J. Atmos. Terr. Phys.*, 12, doi:10.1016/0021-9169(58)90086-2.
- Chandran, A., D. W. Rusch, S. E. Palo, G. E. Thomas, and M. J. Taylor (2009), Gravity wave observations in the summertime polar mesosphere from the Cloud Imaging and Particle Size (CIPS) experiment on the AIM spacecraft, *J. Atmos. Sol.-Terr. Phy.*, 71, doi:10.1016/j.jastp.2008.09.041.
- Charney, J.G., and P.G. Drazin (1961), Propagation of planetary-scale disturbances from the lower into the upper atmosphere, *J. Geophys. Res.*, 66, 83, doi:10.1029/JZ066i001p00083.
- Chu, X. Z., C. S. Gardner, and G. Papen (2001a), Lidar observations of polar mesospheric clouds at south pole: diurnal variations, *Geophys. Res. Lett.*, 28, 1937–1940.
- Chu, X. Z., C. S. Gardner, and G. Papen (2001b), Lidar observations of polar mesospheric clouds at South Pole: Seasonal variations, *Geophys. Res. Lett.*, 28, 1203-1206, doi:10.1029/2000GL012524.
- Chu, X. Z., C. S. Gardner, and R. G. Roble (2003), Lidar studies of interannual, seasonal, and diurnal variations of polar mesospheric clouds at the South Pole, *J. Geophys. Res.*, 108(D8), 8447, doi:10.1029/2002JD002524.
- Chu, X. Z., G. J. Nott, P. J. Espy, C. S. Gardner, J. C. Diettrich, M. A. Clilverd and M. J. Jarvis (2004), Lidar observations of polar mesospheric clouds at Rothera, Antarctica (67.5 degrees S, 68.0 degrees W), *Geophys. Res. Lett.*, 31, doi:10.1029/2003GL018638.
- Chu, X. Z., P. J. Espy, G. J. Nott, J. C. Diettrich, and C. S. Gardner (2006), Polar mesospheric clouds observed by an iron Boltzmann lidar at Rothera (67.5 degrees S, 68.0 degrees W), Antarctica from 2002 to 2005: Properties and implications, *J. Geophys. Res.*, 111, D20213, doi:10.1029/2006JD007086.
- Chu, X., C. Yamashita, P. J. Espy, G. J. Nott, E. J. Jensen, H.-L. Liu, W. Huang, and J. P. Thayer (2009), Responses of polar mesospheric cloud brightness to stratospheric gravity waves at the South Pole and Rothera, Antarctica, *J. Atmos. Sol-Terr. Phy.*, 71, 434-445, doi:10.1016/j.jastp.2008.10.002.

- Dalin, P., S. Kirkwood, H. Andersen, O. Hansen, N. Pertsev and V. Romejko (2006), Comparison of long-term Moscow and Danish NLC observations: statistical results, *Ann. Geophys.*, 24, 2841-2849, doi:10.5194/angeo-24-2841-2006.
- Davies, T., M. J. P. Cullen, A. J. Malcolm, M. H. Mawson, A. Staniforth, A. A. White, and N. Wood (2005), A new dynamical core for the Met Office's global and regional modeling of the atmosphere, *Quart. J. Roy.*, 131, 1759–1782, doi:10.1256/qj.04.101.
- Debrestian, D. J., J. D. Lumpe, E. P. Shettle, R. M. Bevilacqua, J. J. Olivero, J. S. Hornstein, W. Glaccum, D. W. Rusch, C. E. Randall, and M. D. Fromm (1997), An analysis of POAM II solar occultation observations of polar mesospheric clouds in the southern hemisphere, *J. Geophys. Res.*, 102, doi:10.1029/96JD01916.
- DeLand, M.T., E. P. Shettle, G. E. Thomas, and J. J. Olivero (2003), Solar backscattered ultraviolet (SBUV) observations of polar mesospheric clouds (PMCs) over two solar cycles, *J. Geophys. Res.*, 108(D8), 8445, doi:10.1029/2002JD002398.
- DeLand, M.T., E. P. Shettle, G. E. Thomas, and J. J. Olivero (2006a), A quarter-century of satellite polar mesospheric cloud observations, *J. Atmos. Sol. -Terr. Phys.*, 68, 9–29, doi: 10.1016/j.jastp.2005.08.003.
- DeLand, M. T., E. P. Shettle, G. E. Thomas, and J. J. Olivero (2006b), Spectral measurements of PMCs from SBUV/2 instruments, *J. Atmos. Sol.-Terr. Phys.*, 68, 65-77, doi:10.1016/j.jastp.2005.08.006.
- DeLand, M.T., E. P. Shettle, G. E. Thomas, and J. J. Olivero (2007), Latitude-dependent long-term variations in polar mesospheric clouds from SBUV version 3 PMC data, *J. Geophys. Res.*, 112, D10315, doi:10.1029/2006JD007857.
- DeLand, M. T., E. P. Shettle, P. F. Levelt, and M. G. Kowalewski (2010), Polar mesospheric clouds (PMCs) observed by the Ozone Monitoring Instrument (OMI) on Aura, *J. Geophys. Res.*, 115, doi:10.1029/2009JD013685.
- Donahue, T. M., J. E. Blamont, and B. Guenther (1972), Noctilucent Clouds in Daytime - Circumpolar Particulate Layers near Summer Mesopause, *J. Atmos. Sci.*, 29, doi:10.1175/1520-0469(1972)029<1205:NCIDCP>2.0.CO;2.
- Dowdy, A., R. A. Vincent, K. Igarashi, Y. Murayama, and D. J. Murphy (2001), A comparison of mean winds and gravity wave activity in the northern and southern polar MLT, *Geophys. Res. Lett.*, 28, doi:10.1029/2000GL012576.
- Dunkerton, T. J., D. P. Delisi, and M. P. Baldwin (1998), Middle atmosphere cooling trend in historical rocketsonde data, *Geophys. Res. Lett.*, 25, doi:10.1029/98GL02385.
- Eckermann, S. D., K. W. Hoppel, L. Coy, J. P. McCormack, D. E. Siskind, K. Nielsen, A. Kochenash, M. H. Stevens, C. R. Englert, W. Singer, and M. E. Hervig (2009), High-altitude data assimilation system experiments for the northern summer mesosphere season of 2007, *J. Atmos. Sol.-Terr. Phys.*, 71, doi:10.1016/j.jastp.2008.09.036.

- Eremenko, M. N., S. V. Petelina, A. Y. Zasesky, B. Karlsson, C. P. Rinsland, E. J. Llewellyn, and J. J. Sloan (2005), Shape and composition of PMC particles derived from satellite remote sensing measurements, *Geophys. Res. Lett.*, 32, doi:10.1029/2005GL023013.
- Evans, W. F. J., L. R. Laframboise, K. R. Sine, R. H. Wiens, and G. G. Shepherd (1995), Observation of Polar Mesospheric Clouds in Summer 1993 by the Windii Instrument on UARS, *Geophys. Res. Lett.*, 22, doi:10.1029/95GL03018.
- Fiedler, J., G. Baumgarten, and G. von Cossart (2005), Mean diurnal variations of noctilucent clouds during 7 years of lidar observations at ALOMAR, *Ann. Geophys.*, 23, 1175-1181.
- Fiedler, J., G. Baumgarten, and F.-J. Lübken (2009), NLC observations during one solar cycle above ALOMAR, *J. Atmos. Sol.-Terr. Phys.*, 71, 424-433, doi:10.1016/j.jastp.2008.11.010.
- Fiedler, J., G. Baumgarten, U. Berger, P. Hoffmann, N. Kaifler and F. J. Luebken (2011), NLC and the background atmosphere above ALOMAR, *Atmos. Chem. Phys.*, 11, 5701-5717, doi:10.5194/acp-11-5701-2011.
- Fleig, A., R. McPeters, P. Bhartia, B. Schlesinger, R. Cebula, K. Klenk, S. Taylor, and D. Heath (1990), Nimbus 7 Solar Backscatter Ultraviolet (SBUV) Ozone Products User's Guide, *NASA*.
- Förster, W. (1906), Von der Erdatmosphäre zum Himmelsraum, 115 pp, *Hermann Hillger Verlag*, Berlin.
- Fogle, B. and B. Haurwitz (1966), Noctilucent clouds, *Space Sci. Rev.*, 6, 279-340, doi:10.1007/BF00173768.
- Frederick, J. E., R. P. Cebula, and D. F. Heath (1986), Instrument characterization for the detection of long-term changes in stratospheric ozone: an analysis of the SBUV/2 radiometer, *Journal of Atmospheric and Oceanic Technology*, 3, 472-480.
- Fricke, K. H. and U. von Zahn (1985), Mesopause Temperatures Derived from Probing the Hyperfine-Structure of the D2 Resonance Line of Sodium by Lidar, *J. Atmos. Terr. Phys.*, 47, doi:10.1016/0021-9169(85)90116-3.
- Fritts, D. C. and M. J. Alexander (2003), Gravity wave dynamics and effects in the middle atmosphere, *Rev. Geophys.*, 41, doi:10.1029/2001RG000106.
- Gadsden, M. (1985), Observations of Noctilucent Clouds from Northwest Europe, *Ann. Geophys.*, 3, 119-126.
- Gadsden, M. and W. Schröder (1989), Noctilucent Clouds, Physics and Chemistry in Space, Vol. 18, Planetology, Lanzerotti, L., J., Hill, M., Muenster, D. S., *Springer-Verlag*, Berlin.
- Gadsden, M. (1998), The North-West Europe data on noctilucent clouds: a survey, *J. Atmos. Sol.-Terr. Phys.*, 60, doi:10.1016/S1364-6826(98)00072-8.

- Garcia, R. R. (1989), Dynamics, Radiation, and Photochemistry in the Mesosphere - Implications for the Formation of Noctilucent Clouds, *J. Geophys. Res.*, 94(D12), 14605–14615, doi:10.1029/JD094iD12p14605.
- Garcia, R. R. and B. A. Boville (1994), Downward Control of the Mean Meridional Circulation and Temperature Distribution of the Polar Winter Stratosphere, *J. Atmos. Sci.*, 51, doi:10.1175/1520-0469(1994)0512238:COTMMC>2.0.CO;2.
- Garcia, R. R., D. R. Marsh, D. E. Kinnison, B. A. Boville, and F. Sassi (2007), Simulation of secular trends in the middle atmosphere, 1950-2003, *J. Geophys. Res.*, 112, D09301, doi:10.1029/2006JD007485.
- Gardner, C. S., G. C. Papen, X. Z. Chu, and W. L. Pan (2001), First lidar observations of middle atmosphere temperatures, Fe densities, and polar mesospheric clouds over the North and South poles, *Geophys. Res. Lett.*, 28, doi:10.1029/2000GL012622.
- Gelinas, L. J., K. A. Lynch, M. C. Kelley, R. L. Collins, M. Widholm, E. MacDonald, J. Ulwick, and P. Mace (2005), Mesospheric charged dust layer: Implications for neutral chemistry, *J. Geophys. Res.*, 110, A01310, doi:10.1029/2004JA010503.
- Gerrard, A. J., T. J. Kane, and J. P. Thayer (1998), Noctilucent clouds and wave dynamics: Observations at Sondrestrom, Greenland, *Geophys. Res. Lett.*, 25, 2817-2820, doi:10.1029/98GL02107.
- Gerrard, A. J., T. J. Kane, J. P. Thayer, and S. D. Eckermann (2004), Concerning the upper stratospheric gravity wave and mesospheric cloud relationship over Sondrestrom, Greenland, *J. Atmos. Sol.-Terr. Phys.*, 66, 229-240, doi:10.1016/j.jastp.2003.12.005.
- Golitsyn, G. S., A. I. Semenov, N. N. Shefov, L. M. Fishkova, E. V. Lysenko, and S. P. Perov (1996), Long-term temperature trends in the middle and upper atmosphere, *Geophys. Res. Lett.*, 23, doi:10.1029/96GL01592.
- Gordley, L. L., M. E. Hervig, C. Fish, J. M. Russell, III, S. Bailey, J. Cook, S. Hansen, A. Shumway, G. Paxton, L. Deaver, T. Marshall, J. Burton, B. Magill, C. Brown, E. Thompson, and J. Kemp (2009), The solar occultation for ice experiment, *J. Atmos. Sol.-Terr. Phys.*, 71, doi:10.1016/j.jastp.2008.07.012.
- Gumbel, J. and B. Karlsson (2011), Intra- and inter-hemispheric coupling effects on the polar summer mesosphere, *Geophys. Res. Lett.*, 38, L14804, doi:10.1029/2011GL047968.
- Hansen, G. and M. Serwazi, and U. von Zahn (1989), 1st Detection of a Noctilucent Cloud by Lidar, *Geophys. Res. Lett.*, 16, doi:10.1029/GL016i012p01445.
- Hartogh, P., G. R. Sonnemann, M. Grygalashvyly, L. Song, U. Berger, F.-J. Lübken (2010), Water vapor measurements at ALOMAR over a solar cycle compared with model calculations by LIMA, *J. Geophys. Res.*, 115, D00I17, doi:10.1029/2009JD012364.

- Heath, D.F., A. J. Krueger, H. A. Roeder, and B. D. Henderson (1975), The solar backscatter ultraviolet and total ozone mapping spectrometer (SBUV/TOMS) for Nimbus G, *Optical Engineering*, 14, 323–331.
- Hemenway, C. L., R. K. Soberman, and G. Witt (1964), Sampling of noctilucent cloud particles, *Tellus*, 16, 84–88, doi:10.1111/j.2153-3490.1964.tb00146.x.
- Hervig, M. E., R. E. Thompson, M. McHugh, L. L. Gordley, J. M. Russell, and M. E. Summers (2001), First confirmation that water ice is the primary component of polar mesospheric clouds, *Geophys. Res. Lett.*, 28, doi:10.1029/2000GL012104.
- Hervig, M. and D. Siskind (2006), Decadal and inter-hemispheric variability in polar mesospheric clouds, water vapor, and temperature, *J. Atmos. Sol.-Terr. Phys.*, 68, 30-41, doi:10.1016/j.jastp.2005.08.010.
- Hervig, M.E., M. H. Stevens, L. L. Gordley, L. E. Deaver, J. M. Russell III, and S. M. Bailey, (2009d), Relationships between polar mesospheric clouds, temperature, and water vapor from solar occultation for ice experiment (SOFIE) observations, *J. Geophys. Res.*, 114, D20203, doi:10.1029/2009JD012302.
- Hervig, M.E., L. L. Gordley, M. H. Stevens, J. M. Russell III, S. M. Bailey, and G. Baumgarten, (2009a), Interpretation of SOFIE PMC measurements: Cloud identification and derivation of mass density, particle shape, and particle size, *J. Atmos. Sol.-Terr. Phys.*, 71, 316–330, doi:10.1016/j.jastp.2008.07.009.
- Hervig, M. E., L. L. Gordley, J. M. Russell, III, and S. M. Bailey (2009b), SOFIE PMC observations during the northern summer of 2007, *J. Atmos. Sol.-Terr. Phys.*, 71, doi:10.1016/j.jastp.2008.08.010.
- Hervig, M. E., L. L. Gordley, L. E. Deaver, D. E. Siskind, M. H. Stevens, J. M. Russell, III, S. M. Bailey, L. Megner, and C. G. Bardeen (2009c), First Satellite Observations of Meteoric Smoke in the Middle Atmosphere, *Geophys. Res. Lett.*, 36, L18805, doi:10.1029/2009GL039737.
- Hervig, M. E. and L. L. Gordley (2010), Temperature, shape, and phase of mesospheric ice from Solar Occultation for Ice Experiment observations, *J. Geophys. Res.*, 115, D15208, doi:10.1029/2010JD013918.
- Höffner, J., F. J. Lübken (2007), Potassium lidar temperatures and densities in the mesopause region at Spitsbergen (78 degrees N), *J. Geophys. Res.*, 112, doi:10.1029/2007JD008612.
- Holton, J. R. and M. J. Alexander (2000), The Role of Waves in the Transport Circulation of the Middle Atmosphere, *Geophysical Monograph: Atmospheric Science Across the Stratopause*, 123, 21-35.
- Holton, J. R. (2004), An Introduction to Dynamic Meteorology, International Geophysics Series, Vol. 88, fourth edition, 535 pp., ed: Frank Cynar, *Academic Press*, San Diego.

- Horvath, J. J., L. H. Brace, R. W. Simmons (1962), Theory and implementation of the Pitot-static technique for upper atmospheric measurements, University of Michigan College of Engineering, pp. 36, *Office of Research Administration*.
- Humphreys, W. J. (1933), Nacreous and Noctilucent Clouds, *Mon. Wea. Rev.*, 61, 228–229, doi:10.1175/1520-0493(1933)61<228:NANC>2.0.CO;2.
- Hunten, D. M., R. P. Turco, and O. B. Toon (1980), Smoke and Dust Particles of Meteoric Origin in the Mesosphere and Stratosphere, *J. Atmos. Sci.*, 37, 1342–1357, doi:10.1175/1520-0469(1980)037<1342:SADPOM>2.0.CO;2.
- Innis, J. L., A. R. Klekociuk, R. J. Morris, A. P. Cunningham, A. D. Graham, and D. J. Murphy (2008), A study of the relationship between stratospheric gravity waves and polar mesospheric clouds at Davis Antarctica, *J. Geophys. Res.*, 113, doi:10.1029/2007JD009031.
- IPCC, 2007: Climate Change 2007: The Physical Science Basis. Contribution of Working Group I to the Fourth Assessment Report of the Intergovernmental Panel on Climate Change [Solomon, S., D. Qin, M. Manning, Z. Chen, M. Marquis, K.B. Averyt, M. Tignor and H.L. Miller (eds.)]. *Cambridge University Press*, Cambridge, United Kingdom and New York, NY, USA.
- Jardetzky, W. (1926), Über die leuchtenden Wolken, *Meteorolo. Z.*, 43, 310-312.
- Jensen, E. J. (1989), A numerical model of polar mesospheric cloud formation and evolution, Thesis for Doctor of Philosophy, Department of Astrophysical, Planetary and Atmospheric Science, *University of Colorado at Boulder*.
- Jensen, E. J., G. E. Thomas, and O. B. Toon (1989), On the Diurnal-Variation of Noctilucent Clouds, *J. Geophys. Res.*, 94, doi:10.1029/JD094iD12p14693.
- Jesse, O. (1885), Auffallende Abenderscheinungen am Himmel, *Meteor. Z.*, 2, 311-312.
- Jesse, O. (1886), Die auffallenden Abenderscheinungen am Himmel im Juni und Juli 1885, *Meteorol. Z.*, 2, 6.
- Jesse, O. (1890), Luminous clouds, *Nature*, 43, 59–61, doi:10.1038/043059a0.
- Karlsson, B., H. Körnich, and J. Gumbel (2007), Evidence for interhemispheric stratosphere-mesosphere coupling derived from noctilucent cloud properties, *Geophys. Res. Lett.*, 34, L16806, doi:10.1029/2007GL030282.
- Karlsson, B., C. McLandress, and T. G. Shepherd (2009a), Inter-hemispheric mesospheric coupling in a comprehensive middle atmosphere model, *J. Atmos. Sol.-Terr. Phys.*, 71, doi:10.1016/j.jastp.2008.08.006.

- Karlsson, B., C. E. Randall, S. Benze, M. Mills, V. L. Harvey, S. M. Bailey, and J. M. Russell III (2009b), Intra-seasonal variability of polar mesospheric clouds due to inter-hemispheric coupling, *Geophys. Res. Lett.*, 36, L20802, doi:10.1029/2009GL040348.
- Karlsson, B., C. E. Randall, T. G. Shepherd, V. L. Harvey, J. Lumpe, K. Nielsen, S. M. Bailey, M. Hervig, and J. M. Russell (2011), On the seasonal onset of polar mesospheric clouds and the breakdown of the stratospheric polar vortex in the Southern Hemisphere, *J. Geophys. Res.*, 116, D18107, doi:10.1029/2011JD015989.
- Khosravi, R., G. Brasseur, A. Smith, D. Rusch, S. Walters, S. Chabrillat, and G. Kockarts (2002), Response of the mesosphere to human-induced perturbations and solar variability calculated by a 2-D model, *J. Geophys. Res.*, 107, 4358, doi:10.1029/2001JD001235.
- Kinnison, D. E., et al. (2007), Sensitivity of chemical tracers to meteorological parameters in the MOZART-3 chemical transport model, *J. Geophys. Res.*, 112, D20302, doi:10.1029/2006JD007879.
- Kirkwood, S. and K. Stebel, (2003), Influence of planetary waves on noctilucent cloud occurrence over NW Europe, *J. Geophys. Res.*, 108, doi:10.1029/2002JD002356.
- Kirkwood, S., P. Dalin, and A. Rechou (2008), Noctilucent clouds observed from the UK and Denmark - trends and variations over 43 years, *Ann. Geophys.*, 26, doi:10.5194/angeo-26-1243-2008.
- Klostermeyer, J. (2002), Noctilucent Clouds Getting Brighter, *J. Geophys. Res.*, 107, 4195, doi:10.1029/2001JD001345.
- Langematz, U. and M. Kunze (2006), An update on dynamical changes in the Arctic and Antarctic stratospheric polar vortices, *Clim. Dyn.*, 27, 647-660, doi:10.1007/s00382-006-0156-2.
- Langematz, U. and M. Kunze (2008), Climate Variability and Extremes during the Past 100 years (Advances in Global Change Research): Dynamical Changes in the Arctic and Antarctic Stratosphere During Spring, *Springer*, Netherlands, Brönnimann, S., J. Luterbacher, T. Ewen, H. F. Diaz, R. S. Stolarski, and U. Neu (Eds.), 33, 293-301, doi:10.1007/978-1-4020-6766-2_20.
- Leslie, R. C. (1885), Sky Glows, *Nature*, 32, doi:10.1038/032245a0.
- Lin, S. J. (2004), A "vertically Lagrangian" finite-volume dynamical core for global models, *Monthly Weather Review*, 132, 10.1175/1520-0493(2004)132<2293:AVLFDC>2.0.CO;2.
- Lindzen, R. S. (1967), Thermally Driven Diurnal Tide in Atmosphere, *Quart. J. Roy.*, 93, doi:10.1002/qj.49709339503.
- Lindzen, R. S., and D. Blake (1970), Mean Heating of the Thermosphere by Tides, *J. Geophys. Res.*, 75(33), 6868–6871, doi:10.1029/JC075i033p06868.

- Lindzen, R. S. (1981), Turbulence and Stress Owing to Gravity-Wave and Tidal Breakdown, *J. Geophys. Res.*, 86, 9707-9714.
- Lopez-Puertas, M., M. Garcia-Comas, B. Funke, D. Bermejo-Pantaleon, M. Hoepfner, U. Grabowski, G. P. Stiller, T. von Clarmann, and C. von Savigny (2009), Measurements of polar mesospheric clouds in infrared emission by MIPAS/ENVISAT, *J. Geophys. Res.*, 114, doi:10.1029/2009JD012548.
- Lorenc, A. C., S. P. Ballard, R. S. Bell, N. B. Ingleby, P. L. F. Andrews, D. M. Barker, J. R. Bray, A. M. Clayton, T. Dalby, D. Li, T. J. Payne, and F. W. Saunders (2000), The Met. Office global three-dimensional variational data assimilation scheme, *Quart. J. Roy.*, 126, 2991-3012, doi:10.1256/smsqj.57001.
- Lossow, S., C. McLandress, A. I. Jonsson, and T. G. Shepherd (2012), Influence of the Antarctic ozone hole on the polar mesopause region as simulated by the Canadian Middle Atmosphere Model, *J. Atmos. Sol.-Terr. Phys.*, 74, 111 – 123, doi:10.1016/j.jastp.2011.10.010.
- Ludlam, F. H. (1957), Noctilucent Clouds, *Tellus*, 9, 341–364, doi: 10.1111/j.2153-3490.1957.tb01890.x.
- Lübken, F.-J., W. Hillert, G. Lehmacher, U. von Zahn, M. Bittner, D. Offermann, F. J. Schmidlin, A. Hauchecorne, M. Mourier, and P. Czechowsky (1994), Intercomparison of Density and Temperature Profiles Obtained by Lidar, Ionization Gauges, Falling Spheres, Datasondes and Radiosondes During the Dyana Campaign, *J. Atmos. Terr. Phys.*, 56, doi:10.1016/0021-9169(94)90023-X.
- Lübken, F.-J. (1999), Thermal structure of the Arctic summer mesosphere, *J. Geophys. Res.*, 104, 9135-9149.
- Lübken, F.-J., M. J. Jarvis, and G. O. L. Jones (1999), First in situ temperature measurements at the Antarctic summer mesopause, *Geophys. Res. Lett.*, 26, doi:10.1029/1999GL010719.
- Lübken, F.-J. (2000), Nearly zero temperature trend in the polar summer mesosphere, *Geophys. Res. Lett.*, 27, 3603-3606, doi:10.1029/2000GL011893.
- Lübken, F.-J. and A. Müllemann (2003), First in situ temperature measurements in the summer mesosphere at very high latitudes (78 degrees N), *J. Geophys. Res.*, 108, 8448, doi:10.1029/2002JD002414.
- Lübken, F.-J., A. Müllemann, and M. J. Jarvis (2004), Temperatures and horizontal winds in the Antarctic summer mesosphere, *J. Geophys. Res.*, 109, D24112, doi:10.1029/2004JD005133.
- Lübken, F.-J., G. Baumgarten, J. Fiedler, M. Gerding, J. Höffner, and U. Berger (2008), Seasonal and latitudinal variation of noctilucent cloud altitudes, *Geophys. Res. Lett.*, 35, doi:10.1029/2007GL032281.

- Lübken, F.-J., J. Lautenbach, J. Höffner, M. Rapp and M. Zecha (2009), First continuous temperature measurements within polar mesosphere summer echoes, *J. Atmos. Sol.-Terr. Phys.*, 71, 453-463, doi:10.1016/j.jastp.2008.06.001.
- Lübken, F.-J., J. Höffner, T. P. Viehl, B. Kaifler, and R. J. Morris (2011), First measurements of thermal tides in the summer mesopause region at Antarctic latitudes, *Geophys. Res. Lett.*, 38, L24806, 10.1029/2011GL050045.
- Marsh, D. R., R. R. Garcia, D. E. Kinnison, B. A. Boville, F. Sassi, S. C. Solomon, and K. Matthes (2007), Modeling the whole atmosphere response to solar cycle changes in radiative and geomagnetic forcing, *J. Geophys. Res.*, 112, D23306, doi:10.1029/2006JD008306.
- Martyn, D. F. and O. O. Pulley (1936), The temperature and constituents of the upper atmosphere, Bulletin (Council for Scientific and Industrial Research (Australia)), H.J. Green, *Government Printer*.
- McClintock, W. E., D. W. Rusch, G. E. Thomas, A. W. Merkel, M. R. Lankton, V. A. Drake, S. M. Bailey, J. M., Russell III (2009), The cloud imaging and particle size experiment on the aeronomy of ice in the mesosphere mission: instrument concept, design, calibration, and on-orbit performance, *J. Atmos. Sol.-Terr. Phys.* 71, 340–355.
- McPeters, R. D. (1980), The Behavior of Ozone near the Stratopause from 2 Years of BUUV Observations, *J. Geophys. Res.*, 85, 4545-4550.
- McPeters, R. D., T. Miles, L. E. Flynn, C. G. Wellemeyer, J. M. Zawodny (1994), Comparison of SBUV and SAGE II ozone profiles: implications for ozone trends, *J. Geophys. Res.*, 99, 20513.
- Megner, L. (2011), Minimal impact of condensation nuclei characteristics on observable Mesospheric ice properties, *J. Atmos. Sol.-Terr. Phys.*, 73, 2184-2191, doi:10.1016/j.jastp.2010.08.006.
- Merkel, A. W., D. W. Rusch, S. E. Palo, J. M. Russell III, S. M. Bailey (2009), Planetary wave activity in polar mesospheric clouds as observed from the cloud imaging and particle size instrument, *J. Atmos. Sol.-Terr. Phys.*, 71, 381-391, doi:10.1016/j.jastp.2008.12.001.
- Mills, M. J., O. B. Toon, and G. E. Thomas (2005), Mesospheric sulfate aerosol layer, *J. Geophys. Res.*, 110, D24208, doi:10.1029/2005JD006242.
- Mishchenko, M. I., L. D. Travis, D. W. Mackowski (1996), T-matrix computations of light scattering by nonspherical particles: A review, *Journal of Quantitative Spectroscopy and Radiative Transfer*, 55, 5, 535-575, doi:10.1016/0022-4073(96)00002-7.
- Mishchenko, M. I. and L. D. Travis, (1998), Capabilities and limitations of a current FORTRAN implementation of the T-matrix method for randomly oriented, rotationally symmetric scatterers, *Journal of Quantitative Spectroscopy and Radiative Transfer*, 60, 309-324, doi:10.1016/S0022-4073(98)00008-9.

- Morris, R. J., A. R. Klekociuk, R. Latteck, W. Singer, D. A. Holdsworth, and D. J. Murphy (2009), Inter-hemispheric asymmetry in polar mesosphere summer echoes and temperature at 69 degrees latitude, *J. Atmos. Sol.-Terr. Phys.*, 71, 464-469, doi:10.1016/j.jastp.2008.09.042.
- Murray, B. J. and E. J. Jensen (2010), Homogeneous nucleation of amorphous solid water particles in the upper mesosphere, *J. Atmos. Sol.-Terr. Phys.*, 72, 51-61, doi:10.1016/j.jastp.2009.10.007
- Nedoluha, G. E. and R. M. Bevilacqua, R. M. Gomez, B. C. Hicks, J. M. Russell and Connor, B. J. (2003), An Evaluation of Trends in Middle Atmospheric Water Vapor as Measured by HALOE, WVMS, and POAM, *J. Geophys. Res.*, 108, 4391, doi:10.1029/2002JD003332.
- Nielsen, K. and D. E. Siskind, S. D. Eckermann, K. W. Hoppel, L. Coy, J. P. McCormack, S. Benze, C. E. Randall and Hervig, M. E. (2010), Seasonal variation of the quasi 5 day planetary wave: Causes and consequences for polar mesospheric cloud variability in 2007, *J. Geophys. Res.*, 115, doi:10.1029/2009JD012676
- Nordberg, W. L. Katchen, J. Theon and W. S. Smith (1965), Rocket Observations of the Structure of the Mesosphere, *J. Atmos. Sci.*, 22, 611-622, doi:10.1175/1520-0469(1965)022%3C0611:ROOTSO%3E2.0.CO;2.
- Olivero, J. J. and G. E. Thomas (1986), Climatology of Polar Mesospheric Clouds, *J. Atmos. Sci.*, 43, 1263-1274, doi:10.1175/1520-0469(1986)043<1263:COPMC>2.0.CO;2.
- Olivero, J. J. and G. E. Thomas (2001), Evidence for changes in greenhouse gases in the mesosphere, *Adv. Space Res.*, 28, 931-936, doi:10.1016/S0273-1177(01)80020-X.
- Petelina, S. V., D. A. Degenstein, E. J. Llewellyn, N. D. Lloyd, C. J. Mertens, M. G. Mlynczak, and J. M. Russell (2005), Thermal conditions for PMC existence derived from Odin/OSIRIS and TIMED/SABER data, *Geophys. Res. Lett.*, 32, L17813, doi:10.1029/2005GL023099.
- Petelina, S. V. E. J. Llewellyn, D. A. Degenstein and Lloyd, N. D. (2006), Odin/OSIRIS limb observations of polar mesospheric clouds in 2001-2003, *J. Atmos. Sol.-Terr. Phys.*, 68, 42-55, doi:10.1016/j.jastp.2005.08.004.
- Petrie, S. (2004), Basic Atmospheric Chemistry: A Quantum Chemical Study on Hydration of Mesospheric NaOH, *Environ. Chem.*, 1, 35-43, doi: 10.1071/EN04001.
- Plane, J. M. C. (2000), The role of sodium bicarbonate in the nucleation of noctilucent clouds, *Ann. Geophys.*, 18, 807-814, doi:10.1007/s00585-000-0807-2.
- Poppe, A. D. James and Horanyi, M. (2011), Measurements of the terrestrial dust influx variability by the Cosmic Dust Experiment, *Planet. Space Sci.*, 59, 319-326, doi:10.1016/j.pss.2010.12.002.

- Pueschel, R. F., S. Verma, H. Rohatschek, G. V. Ferry, N. Boiadjieva, S. D. Howard, and A. W. Strawa (2000), Vertical transport of anthropogenic soot aerosol into the middle atmosphere, *J. Geophys. Res.*, 105(D3), 3727–3736, doi:10.1029/1999JD900505.
- Randel, W. J., K. P. Shine, J. Austin, J. Barnett, C. Claud., N. P. Gillett, P. Keckhut, U. Langematz, R. Lin, C. Long, C. Mears, A. Miller, J. Nash, D. J. Seidel, D. W. J. Thompson, F. Wu, and S. Yoden (2009), An update of observed stratospheric temperature trends, *J. Geophys. Res.*, 114, doi:10.1029/2008JD010421.
- Rapp, M. and F. J. Lübken (2004), Polar mesosphere summer echoes (PMSE): review of observations and current understanding, *Atmos. Chem. Phys.*, 4, 2601-2633, doi:10.5194/acp-4-2601-2004.
- Rapp, M. and G. E. Thomas (2006), Modeling the microphysics of mesospheric ice particles: Assessment of current capabilities and basic sensitivities, *J. Atmos. Sol.-Terr. Phys.*, 68, 715–744, doi:10.1016/j.jastp.2005.10.015.
- Rapp, M. and I. Strelnikova (2009), Measurements of meteor smoke particles during the ECOMA-2006 campaign: 1. Particle detection by active photoionization, *J. Atmos. Sol.-Terr. Phys.*, 71, 477-485, doi:10.1016/j.jastp.2008.06.002.
- Rapp, M. I. Strelnikova, B. Strelnikov, R. Latteck, G. Baumgarten, Q. Li, L. Megner, J. Gumbel, M. Friedrich, U. P. Hoppe, and S. Robertson (2009), First in situ measurement of the vertical distribution of ice volume in a mesospheric ice cloud during the ECOMA/MASS rocket-campaign, *Ann. Geophys.*, 27, 755-766, doi:10.5194/angeo-27-755-2009.
- Reinecker, M. M., et al. (2008), The GEOS-5 data assimilation system — documentation of Versions 5.0.1 and 5.1.0, Tech. Rep. NASA/TM-2007-104606, Vol. 27, *NASA GSFC*.
- Richter, J. H. F. Sassi and R. R. Garcia (2010), Toward a Physically Based Gravity Wave Source Parameterization in a General Circulation Model, *J. Atmos. Sci.*, 67, 136-156, doi:10.1175/2009JAS3112.1.
- Robert, C.E., C. von Savigny, J. P. Burrows, G. Baumgarten (2009), Climatology of noctilucent cloud radii and occurrence frequency using SCIAMACHY, *J. Atmos. Sol.-Terr. Phys.*, 71, 408–423.
- Rosinski, J., R. H. Snow (1961), Secondary Particulate Matter from Meteor Vapors, *J. Meteor.*, 18, 736–745, doi:10.1175/1520-0469(1961)018<0736:SPMFMV>2.0.CO;2.
- Rusch, D.W., S. M. Bailey, G. E. Thomas, and A. W. Merkel (2008), Seasonal-latitudinal variations of PMC particle size from SME measurements for the northern 1983 Season and SNOE measurements for the northern 2000 and southern 2000/2001 seasons. *J. Atmos. Sol.-Terr. Phys.*, 70, 71–88, doi:10.1016/j.jastp.2007.10.006.
- Rusch, D.W., G. E. Thomas, W. E. McClintock, A. W. Merkel, S. M. Bailey, J. M. Russell III, C. E. Randall, C. D. Jepsen and M. Callan (2009), The cloud imaging and particle size experiment on the Aeronomy of Ice in the Mesosphere mission: cloud morphology for the

- northern 2007 season, *J. Atmos. Sol.-Terr. Phys.*, 71, 356-364, doi:10.1016/j.jastp.2008.11.005.
- Russell III, J.M., M. G. Mlynczak, L. L. Gordley, J. J. Tansock, R. Esplin (1999), An overview of the SABER experiment and preliminary calibration results, *Proceedings of SPIE 3756*, 277–288.
- Russell III, J.M., S. M. Bailey, L. L. Gordley, D. W. Rusch, M. Horanyi, M. E. Hervig, G. E. Thomas, C. E. Randall, D. E. Siskind, M. H. Stevens, M. E. Summers, M. I. Taylor, C. R. Englert, P. J. Espy, W. E. McClintock, and A. W. Merkel (2009), The aeronomy of ice in the mesosphere (AIM) mission: overview and early science results, *J. Atmos. Sol.-Terr. Phys.*, 71, 289–299, doi:10.1016/j.jastp.2008.08.011.
- J. M. Russell, III, P. Rong, S. M. Bailey, M. E. Hervig and S. V. Petelina (2010), Relationship between the summer mesopause and polar mesospheric cloud heights, *J. Geophys. Res.*, 115, doi:10.1029/2010JD013852.
- Schmidlin, F. J. H. S. Lee and W. Michel (1991), The Inflatable Sphere - A Technique For The Accurate Measurement of Middle Atmosphere Temperatures, *J. Geophys. Res.*, 96, 22673-22682, doi:10.1029/91JD02395.
- Schmidt, H. and G. P. Brasseur, M. Charron, E. Manzini, M. A. Giorgetta, T. Diehl, V. I. Fomichev, D. Kinnison, D. Marsh and S. Walters (2006), The Hammonia Chemistry Climate Model: Sensitivity of the Mesopause Region to the 11-Year Solar Cycle and CO₂ Doubling, *J. Climate*, 19, 3903-3931.
- Schröder, W., 2001. Otto Jesse and the investigation of noctilucent clouds 115 years ago. *Bulletin of the American Meteorological Society*, 82, 2457-2468, doi:10.1175/1520-0477(2001)082<2457:OJATIO>2.3.CO;2.
- Semenov, A.I., N. N. Shefov, E. V. Lysenko, G. V. Givishvili, and A. V. Tikhonov (2002), The season peculiarities of behavior of the long-term temperature trends in the middle atmosphere on the mid-latitudes, *Phys. Chem. Earth*, 27, 529–534.
- Shepherd, T. G. (2000), The middle atmosphere, *J. Atmos. Sol.-Terr. Phys.*, 62, 1587-1601, doi:10.1016/S1364-6826(00)00114-0.
- Shepherd, T. G. (2007), Transport in the middle atmosphere, *Journal of the Meteorological Society of Japan*, 85B, 165-191, doi:10.2151/jmsj.85B.165.
- Shettle, E.P., G. E. Thomas, J. J. Olivero, W. F. J. Evans, D. J. Debrestian, L. Chardon (2002) Three-satellite comparison of polar mesospheric clouds: evidence for long-term change, *J. Geophys. Res.*, 107, D12, doi:10.1029/2001JD000668.
- Shettle, E. P., M. T. DeLand, G. E. Thomas, and J. J. Olivero (2009), Long term variations in the frequency of polar mesospheric clouds in the northern hemisphere from SBUV, *Geophys. Res. Lett.*, 36, L02803, doi:10.1029/2008GL036048.

- Shettle, E. P., G. E. Nedoluha, M. T. DeLand, G. E. Thomas, and J. J. Olivero (2010), SBUV observations of polar mesospheric clouds compared with MLS temperature and water vapor measurements, *Geophys. Res. Lett.*, 37, L18810, doi:10.1029/2010GL044132.
- Siskind, D. E., S. D. Eckermann, J. P. McCormack, M. J. Alexander, and J. T. Bacmeister (2003), Hemispheric differences in the temperature of the summertime stratosphere and mesosphere, *J. Geophys. Res.*, 108, doi:10.1029/2002JD002095.
- Smith, A. K., R. R. Garcia, D. R. Marsh, D. E. Kinnison, and J. H. Richter (2010), Simulations of the response of mesospheric circulation and temperature to the Antarctic ozone hole, *Geophys. Res. Lett.*, 37, L22803, doi:10.1029/2010GL045255.
- Stevens, M. H. R. R. Conway, C. R. Englert, M. E. Summers, K. U. Grossmann and O. A. Gusev (2001), PMCs and the water frost point in the Arctic summer mesosphere, *Geophys. Res. Lett.*, 28, 4449-4452, doi:10.1029/2001GL013598.
- Stevens, M. H., C. R. Englert, and J. Gumbel (2002), OH observations of space shuttle exhaust, *Geophys. Res. Lett.*, 29, doi:10.1029/2002GL015079.
- Stevens, M. H., J. Gumbel, C. R. Englert, K. U. Grossmann, M. Rapp, and P. Hartogh (2003), Polar mesospheric clouds formed from space shuttle exhaust, *Geophys. Res. Lett.*, 30, 10, 1546, doi:10.1029/2003GL017249.
- Stevens, M. H., C. R. Englert, M. T. DeLand, and M. Hervig (2005a), The polar mesospheric cloud mass in the Arctic summer, *J. Geophys. Res.*, 110, doi:10.1029/2004JA010566.
- Stevens, M. H., R. R. Meier, X. Chu, M. T. DeLand, and J. M. C. Plane (2005b), Antarctic mesospheric clouds formed from space shuttle exhaust, *Geophys. Res. Lett.*, 32, L13810, doi:10.1029/2005GL023054.
- Stevens, M. H., C. R. Englert, M. Hervig, S. V. Petelina, W. Singer and K. Nielsen (2009), The Diurnal Variation of Polar Mesospheric Cloud Frequency near 55 Degrees N Observed by Shimmer, *J. Atmos. Sol.-Terr. Phys.*, 71, 401-407, doi:10.1016/j.jastp.2008.10.009.
- Stevens, M. H., D. E. Siskind, S. D. Eckermann, L. Coy, J. P. McCormack, C. R. Englert, K. W. Hoppel, K. Nielsen, A. J. Kochenash, M. E. Hervig, C. E. Randall, J. Lumpe, S. M. Bailey, M. Rapp, and P. Hoffmann (2010), Tidally induced variations of polar mesospheric cloud altitudes and ice water content using a data assimilation system, *J. Geophys. Res.*, 115, D18209, doi:10.1029/2009JD013225.
- Stevens, M. H., L. E. Deaver, M. E. Hervig, J. M. Russell, III, D. E. Siskind, P. E. Sheese, E. J. Llewellyn, R. L. Gattinger, J. Höffner, and B.T. Marshall (2012), Validation of Upper Mesospheric and Lower Thermospheric Temperatures Measured by the Solar Occultation For Ice Experiment, *submitted to J. Geophys. Res.*.
- Strelnikova, I. M. Rapp, B. Strelnikov, G. Baumgarten, A. Brattli, K. Svenes, U. Hoppe, M. Friedrich, J. Gumbel and B. P. Williams (2009), Measurements of meteor smoke particles

- during the ECOMA-2006 campaign: 2. Results, *J. Atmos. Sol.-Terr. Phys.*, 71, 486-496, doi:10.1016/j.jastp.2008.07.011.
- Swinbank, R. and A. O'Neill (1994), A Stratosphere-Troposphere Data Assimilation System, *Monthly Weather Review*, 122, 686-702, doi:10.1175/1520-0493(1994)1220686:ASTDAS>2.0.CO;2.
- Taylor, M.J., M. Gadsden, R. P. Lowe, M. S. Zalcik, J. Brausch (2002), Mesospheric cloud observations at unusually low latitudes, *J. Atmos. Sol.-Terr. Phys.*, 64, 991–999.
- Thayer, J. P., M. Rapp, A. J. Gerrard, E. Gudmundsson, and T. J. Kane (2003), Gravity-wave influences on Arctic mesospheric clouds as determined by a Rayleigh lidar at Sondrestrom, Greenland, *J. Geophys. Res.*, 108, doi:10.1029/2002JD002363.
- Theon, J. S. W. Nordberg, L. B. Katchen and J. J. Horvath (1967), Some Observations on Thermal Behavior of Mesosphere, *J. Atm. Sci.*, 24, 428-438, doi:10.1175/1520-0469(1967)0240428:SOOTTB>2.0.CO;2.
- Thomas, R. J. and T. M. Donahue (1972), Analysis of OGO-6 Observations of OI5577-A Tropical Nightglow, *J. Geophys. Res.*, 77, 3557-3565, doi:10.1029/JA077i019p03557.
- Thomas, G. E. et al. (1980), Scientific Objectives of the Solar Mesosphere Explorer Mission, *Pure and Applied Geophysics*, 118, 591-615, doi:10.1007/BF01586468.
- Thomas, G. E. (1984), Solar Mesosphere Explorer Measurements of Polar Mesospheric Clouds (Noctilucent Clouds), *J. Atmos. Terr. Phy.*, 46, 819-824, doi:10.1016/0021-9169(84)90062-X.
- Thomas, G.E., J. J. Olivero (1989), Climatology of Polar mesospheric clouds .2. Further analysis of solar mesosphere explorer data, *J. Geophys. Res.*, 94, 14673–14681.
- Thomas, G.E., J. J. Olivero, E. J. Jensen, W. Schroeder, O. W. Toon (1989), Relation between increasing methane and the presence of ice clouds at the mesopause, *Nature*, 338, 490–492, doi:10.1038/338490a0.
- Thomas, G. E. (1991), Mesospheric Clouds and the Physics of the Mesopause Region, *Rev. Geophys.*, 29, 553-575, doi:10.1029/91RG01604.
- Thomas, G. E., R. D. McPeters, and E. J. Jensen (1991), Satellite-Observations of Polar Mesospheric Clouds by the Solar Backscattered Ultraviolet Spectral Radiometer - Evidence of a Solar-Cycle Dependence, *J. Geophys. Res.*, 96, D1, 927–939, doi:10.1029/90JD02312.
- Thomas, G.E. (1996a), Is the polar mesosphere the miner's canary of global change? *Adv. Space Res.*, 18, 149–158.
- Thomas, G.E. (1996b), Global change in the mesosphere lower thermosphere region: has it already arrived? *J. Atmos. Terr. Phys.*, 58, 1629–1656, doi:10.1016/0021-9169(96)00008-6.

- Thomas, G. E. and J. Olivero (2001), Noctilucent clouds as possible indicators of global change in the mesosphere, *Adv. Space Res.*, 28, 937-946, doi:10.1016/S0273-1177(01)80021-1.
- Thomas, G. E., J. J. Olivero, M. T. Deland and E. P. Shettle (2003), Comment on “Are noctilucent clouds truly a “Miner's Canary” for Global Change?”, *Eos Trans. AGU*, 84, 36.
- Thomas, G.E. (2003), Are noctilucent clouds harbingers of global change in the middle atmosphere? *Adv. Space Res.*, 32, 1737–1746, doi:10.1016/S0273-1177(03)90470-4.
- Thompson, D. W. J. and S. Solomon (2002), Interpretation of recent Southern Hemisphere climate change, *Science*, 296, 895-899, doi:10.1126/science.1069270.
- Tseraskii, V. K. (1890), On Luminous Clouds, *Ann. Observ. Moscow*, 2, 177, in Russian.
- Uppala, S. M., et al. (2005), The ERA-40 re-analysis, *Quart. J. Roy.*, 131, 2961-3012, doi:10.1256/qj.04.176.
- Vestine, E. H. (1934), Noctilucent Clouds (with Plate VI), *Journal of the Royal Astronomical Society of Canada*, 28, 249.
- Vincent, R. A. (1994), Gravity-Wave Motions in the Mesosphere and Lower Thermosphere Observed at Mawson, Antarctica, *J. Atmos. Terr. Phys.*, 56, doi:10.1016/0021-9169(94)90100-7.
- von Cossart, G., J. Fiedler, U. von Zahn, G. Hansen, and U. P. Hoppe (1997), Noctilucent clouds: One- and two-color lidar observations, *Geophys. Res. Lett.*, 24, 1635-1638, doi:10.1029/97GL01575.
- von Cossart, G., J. Fiedler, and U. von Zahn (1999), Size distributions of NLC particles as determined from 3-color observations of NLC by ground-based lidar, *Geophys. Res. Lett.*, 26, 11, 1513–1516, doi:10.1029/1999GL900226.
- von Zahn, U., G. von Cossart, J. Fiedler, and D. Rees (1998), Tidal variations of noctilucent clouds measured at 69 degrees N latitude by groundbased lidar, *Geophys. Res. Lett.*, 25, 1289–1292, doi:10.1029/98GL00546.
- von Zahn, U., G. von Cossart, J. Fiedler, K. H. Fricke, G. Nelke, G. Baumgarten, D. Rees, A. Hauchecorne and K. Adolfsen (2000), The ALOMAR Rayleigh/Mie/Raman lidar: objectives, configuration, and performance, *Ann. Geophys.*, 18, 815-833, doi:10.1007/s00585-000-0815-2.
- von Zahn, U. (2003), Are noctilucent clouds a “Miner's Canary” for global change?, *Eos Trans. AGU*, 84, doi:10.1029/2003EO280001.
- von Zahn, U., U. Berger, J. Fiedler and P. Hartogh (2004), Noctilucent clouds and mesospheric water vapor: the past decade, *Atmos. Chem. Phys.*, 4, 2449–2464.

- Warren, S. G., G. E. Thomas, G. Hernandez, and R. W. Smith (1997), Noctilucent cloud observed in late April at South Pole Station: Temperature anomaly or meteoritic debris?, *J. Geophys. Res.*, 102, D2, 1991–2000, doi:10.1029/96JD02513.
- Waugh, D. W., W. J. Randel, S. Pawson, P. A. Newman, and E. R. Nash (1999), Persistence of the lower stratospheric polar vortices, *J. Geophys. Res.*, 104, D22, 27191-27201.
- Wegener, A. (1912), Die Erforschung der obersten Atmosphärenschichten, *Zeitschrift für anorganische Chemie*, 75, 107-131, doi:10.1002/zaac.19120750112.
- Wickwar, V. B., M. J. Taylor, J. P. Herron and B. A. Martineau (2002), Visual and Lidar Observations of Noctilucent Clouds Above Logan, Utah, at 41.7 Degrees N, *J. Geophys. Res.*, 107, 4054, doi:10.1029/2001JD001180.
- Witt, G., J. Martin-Löf, N. Wilhelm, W. S. Smith (1964) High latitude summer mesospheric temperatures and winds with particular regard to noctilucent clouds, *Space Research V*, 820-821.
- Witt, G. (1969), The nature of noctilucent clouds, *Space Research IX*, 157–169.
- WMO (World Meteorological Organization) Scientific Assessment of Ozone Depletion: 2006, *Global Ozone Research and Monitoring Project - Report No. 50*, 572pp., Geneva, 2007.
- Woodman, R. F., B. B. Balsley, F. Aquino, L. Flores, E. Vazquez, M. Sarango, M. M. Huaman, and H. Soldi (1999), First Observations of Polar Mesosphere Summer Echoes in Antarctica, *J. Geophys. Res.*, 104, A10, 22577–22590, doi:10.1029/1999JA900226.
- Woods, T. N., W. K. Tobiska, G. J. Rottman, and J. R. Worden (2000), Improved solar Lyman alpha irradiance modeling from 1947 through 1999 based on UARS observations, *J. Geophys. Res.*, 105, 27195-27215, doi:10.1029/2000JA000051.
- Wrotny, J. E. and J. M. Russell, III (2006), Interhemispheric differences in polar mesospheric clouds observed by the HALOE instrument, *J. Atmos. Sol.-Terr. Phys.*, 68, 1352-1369, doi:10.1016/j.jastp.2006.05.014.
- Zasetsky, A. Y., S. V. Petelina and I. M. Svishchev (2009), Thermodynamics of homogeneous nucleation of ice particles in the polar summer mesosphere, *Atmos. Chem. Phys.*, 9, doi:10.5194/acp-9-965-2009.